

Theory of Computing Point Spread Functions

by

Ratsimandresy Holinirina Dina Miora
born on 01 November 1992

*Dissertation presented for the degree of doctor rerum
naturalium, Dr. rer. nat. in the Faculty of Physics and
Astronomy at Friedrich Schiller University Jena, and Doctor of
Philosophy, Ph.D in Physics in the Faculty of Science at
Stellenbosch University*



Supervisors:

Dr. Gurthwin Bosman

Prof. Dr. Erich Rohwer

Prof. Dr. Rainer Heintzmann

2023

Examination

Reviewers:

- Examiner 1: Prof. Dr. Rainer Heintzmann, Professor at Friedrich Schiller University Jena, Germany
- Examiner 2: Dr. Gurthwin Bosman, Senior Researcher and Lecturer at Stellenbosch University, South Africa
- Examiner 3: Prof. Dr. Andrew Forbes, Professor at Witwatersrand University, South Africa
- Examiner 4: Prof. Dr. Jerome Mertz, Professor at Boston University, United States

Oral examination date:

22 November 2023

Declaration

By submitting this dissertation electronically, I, Ratsimandresy Holinirina Dina Miora, declare that the entirety of the work contained therein is my own, original work, that I am the sole author thereof. I have not copied any text passages from third parties or my own dissertations without referencing them accordingly and acknowledging any aids, personal correspondences and sources used in my work. The persons who assisted me to the completion of this thesis are listed in the acknowledgements with their respective contribution. This doctoral thesis has not yet been submitted as part of a state examination or other scientific examination except under the joint-degree examination between Friedrich Schiller University Jena (FSU) and Stellenbosch University (SU). A similar or in significant parts similar doctoral thesis or other paper has not been submitted to any other institution of higher education other than FSU and SU in accordance with the cotutelle agreement between FSU and SU. I have not received any assistance from commercial agents offering dissertation services and that no third party has - either directly or indirectly - received any financial benefits for producing work in connection with this doctoral thesis. Reproduction and publication thereof by FSU and SU will not infringe any third party rights. I hereby confirm that I am familiar with the current Examination Regulations related to my joint-degree between FSU and SU.

Signature:

Ratsimandresy Holinirina Dina Miora

Date:

Copyright © 2023.

Friedrich Schiller University Jena and Stellenbosch University.

All rights reserved.

Abstract

Theory of Computing Point Spread Functions

Ratsimandresy Holinirina Dina Miora

Dissertation: PhD

2023

Incoherent imaging in fluorescence microscopy is mathematically formulated as a convolution of the object with the optical response of the system, which is called point spread function (PSF). This response occurs under certain imaging condition invariances such as the shift-invariance and the Abbe sine condition. The image quality and resolution are limited by the numerical aperture of the system and the wavelength of the emitted light, which in turn define the diffraction limit of the optical system. The optical resolution and/or image quality can be improved either by developing an advanced imaging system with an inherently smaller PSF or by trying to undo the convolution of the object with the PSF using a mathematical approach called “deconvolution” under plausible assumptions about the object. A realistic and accurate PSF model is required for an accurate and efficient deconvolution process. In this thesis, we present a theoretical approach of computing PSFs in the field of fluorescence microscopy under realistic acquisition conditions with a given set of known and unknown imaging parameters. Four techniques for computing the PSFs of a wide-field microscope have been developed. These PSF models, two of which are completely new, are Fourier-based, easy to implement, suitable for tilted stratified medium, and account for the vector features of light. The fast Fourier-transformation is a practical tool to speed up PSF calculations, and its pitfalls are carefully avoided in our computation. Our PSF models are compared to state-of-the-art PSFs in current theoretical works, validated experimentally and tested for their deconvolution efficiency. The models are demonstrated to be superior to existing state-of-the-art PSFs. The deconvolution using our PSF models has been found to enable a contrast improvement of up to $162\times$.

Zusammenfassung

Theorie der Berechnung von Punktspreizfunktionen

Ratsimandresy Holinirina Dina Miora

Dissertation: Dr. rer. nat.

Dezember 2023

Das Bildgebungsverfahren mit inkohärentem Licht in der Fluoreszenzmikroskopie ist mathematisch formuliert als Faltung eines Objekts mit der optischen Antwort des Systems, der Punktspreizfunktion (PSF). Diese Antwort findet unter bestimmten Bildgebungsbedingungen, wie z.B. der Verschiebungsinvarianz und der Abbe-Sinus-Bedingung, statt. Die Bildqualität und Auflösung eines optischen Systems werden durch die numerische Apertur des Systems und der Wellenlänge des emittierten Lichts begrenzt, welche wiederum durch die Beugungsgrenze des optischen Systems definiert wird. Die optische Auflösung und die Bildqualität kann entweder durch eine Weiterentwicklung des Bildgebungsverfahrens in ein Verfahren mit inhärent kleinerer PSF oder durch die Umkehrung der Faltung des Objektes mit der PSF durch einen mathematischen Ansatz namens "Dekonvolution" unter plausiblen Annahmen verbessert werden. Für einen effizienten Dekonvolutionsprozess wird ein realistisches und akkurates Modell der PSF benötigt. In dieser Doktorarbeit präsentieren wir eine Theorie der Berechnung der PSF in der Fluoreszenzmikroskopie unter realistischen Aufnahmebedingungen mit einer gegebenen Anzahl bekannter und unbekannter Bildgebungsparametern. Vier Ansätze zur Berechnung der PSF eines Weitfeldsystems, von denen zwei gänzlich neu sind, werden entwickelt. Diese neuen PSF-Modelle sind Fourier basiert, einfach zu implementieren, für gekippte stratifizierte Medien geeignet und beziehen die vektoriellen Eigenschaften des Lichtes mit ein. Die schnelle Fourier-Transformation ist ein praktisches Verfahren zur Beschleunigung von PSF-Berechnungen und ihre Stolperfallen werden bei unseren Berechnungen sorgfältig vermieden. Unsere PSF-Modelle werden mit Modellen nach dem aktuellen Stand der theoretischen Wissenschaft verglichen, experimentell validiert und auf ihre Dekonvolutionseffizienz getestet. Wir zeigen dass unsere PSF Modelle besser als existierende Modelle sind. Die Dekonvolution mit unseren Modellen erlauben eine Kontrastverbesserungsfaktor bis zu 162.

Acknowledgements

I would not have been able to complete this thesis without the great help and support of many people, colleagues and friends. I am grateful for the patience, guidance, and financial and moral support of my supervisors: Gurthwin Bosman, Erich Rohwer, and Rainer Heintzmann. I am especially grateful for their sacrifice of time, even outside the working hours.

I wish to thank the Laser Research Institute, Stellenbosch University, and the Nanoimaging Research Group, Jena, for accepting me to be a part of their group. The discussions and oral presentations I have had in both groups have greatly helped me to improve my work. I would like to thank Fengjiao Ma, in particular, for the fruitful discussion on deconvolution, Monalisa Goswami, Patrick Then, and Elia Alejandra Zegarra Valverde for assisting me with the experimental work during my stay in Jena in 2018 and 2019. I would also like to acknowledge the assistance of Andre du Toit at the Department of Physiology, Stellenbosch University during the PSF measurement. A special thanks to Maximilian Senftleben from the SaraLab for providing a large part of the experimental PSFs data that are used in this thesis.

I would also like to thank Colin Sheppards for fruitful discussion on aplanatic factor, Martin Kielhorn for providing the first idea of the SincR PSF model, Herbert Gross and Norman Girma Worku for the first draft of the MATLAB code of the chirp-Z transform function, and Peter Verveer for the first version of the DIPimage Library of the Richards and Wolf code in our MATLAB toolbox.

I thank Ando Zehrer and Ulrike Schulze for helping me write the German version of the abstract, and Jason Francis and Nick Barry for proofreading the thesis and giving constructive advice during the writing process.

This work would not have been achieved without the financial and material support of the Stellenbosch University, the African Laser Center in South Africa, the scholarship from DAAD, and the African Institute for Mathematical Sciences, and Friedrich Schiller Jena University for my stay in Jena in 2018. In addition, I wish to thank Herbert Stafast for his help and hospitality at his home during my stay in Jena.

My special thanks are extended to my family and friends in Madagascar, Stellenbosch, and Jena for their encouragement and continuous support.

Last but not least, I wish to thank God for giving me the strength, grace, and knowledge to complete this thesis.

Dedications

... so that in all things God may be praised

Nomenclature

Constants

$$\epsilon_0 = 8.854 \times 10^{-12} \text{ m}^{-3} \cdot \text{kg}^{-1} \cdot \text{s}^4 \cdot \text{A}^2$$

$$\mu_0 = 4\pi \times 10^{-7} \text{ kg} \cdot \text{m} \cdot \text{s}^{-2} \cdot \text{A}^{-2}$$

Variables

(x, y, z)	Cartesian coordinates in real space	[pixels]
(p_x, p_y, p_z)	Pixel pitch in (x, y, z) –direction respectively	[nm]
(k_x, k_y, k_z)	Spatial frequency coordinates in Fourier space	[rad · nm ⁻¹]
(v, u)	Radial and axial optical coordinate	[o.u.]
θ	Elevation angle	[°]
ϕ	Azimuthal angle	[°]
r	Radial position	[pixels]
α	Rotation angle	[°]
λ_{em}	Emission wavelength	[nm]
λ_0	Emission wavelength in vacuum	[nm]
λ_{ex}	Excitation wavelength	[nm]
$k = 2\pi/\lambda_{\text{em}}$	Wave-number	
NA	Numerical aperture	[]
M	Radial magnification	[]
Φ	Wavefront aberration	[nm]
(n, m)	Radial and azimuthal orders of wavefront aberration	[]
Z_n^m	Zernike polynomials of order (n, m)	[nm]
C_n^m	Amplitudes or coefficients of Z_n^m	[nm]
n_j	Refractive index of the medium j	
t_j	Thickness of the medium j	[nm]
$t_m^{(j)}$	Transmission coefficient of m –polarized light at interface $j, m = p$ for polarization parallel to the plane of incidence, and s for polarization normal to the plane of incidence	

Abbreviations in alphabetical order

AF	Aplanatic Factor
AFP	Actual Focus Position
ASF	Amplitude Point Spread Function, also denoted by \vec{h}
ATF	Amplitude Point Transfer Function
BFP	Back Focal Plane
CZT	Chirp-Z Transform
DC	Design Condition of the optical imaging system
Exp-PSF	Experimental Point Spread Function
FFT	Fast Fourier Transform
FS	Focal Shift
FT	Fourier Transform
F-Shell	Fourier Shell method
GS	Gold Standard
LSI	Linear Shift Invariant
LSV	Linear Shift Variant
MRE	Mean Relative Error
NCC	Normalized Cross Correlation
NDC	Non-Design Condition of the optical imaging system
NFP	Nominal Focus Position
OL	Objective Lens
OPD	Optical Path Difference
OTF	Optical Transfer Function, also denoted by \tilde{h}
o.u.	Optical Unit
PSF	Point Spread Function, also denoted by h
RI	Refractive Index
SAF	Supercritical Angle Fluorescence
Std	Standard deviation
RW	Richards and Wolf method
S	Strehl ratio
Sinc-R	Sinc-R method
SP-CZT	Slice propagation method using the CZT
SP-FFT	Slice propagation method using the FFT
WD	Working distance

Vectors and Tensors

$\vec{E}(r, t)$ Electric field evaluated at spatial position r and time t

$\vec{B}(r, t)$ Magnetic field evaluated at spatial position r and time t

Subscripts

eff Effective

l Lens

i Immersion medium

g Coverslip

s Sample

Superscripts

* Variables in DC when paired with $n_s, n_g,$ and n_i

* Identifying the models described and developed in this thesis when paired with SP-FFT, SP-CZT, F-Shell, and Sinc-R

Contents

Abstract	iii
Zusammenfassung	iv
Acknowledgements	v
Dedications	vi
Nomenclature	vii
Contents	x
List of Figures	xii
1 Introduction	1
1.1 Context and research question	1
1.2 Current state of the art	4
1.3 Outline of the thesis	9
2 Theoretical Background	10
2.1 Image formation	10
2.2 Diffraction theory of light	16
2.3 Diffraction theory of aberration	24
2.4 Fourier imaging	25
2.5 Image reconstruction: deconvolution	26
3 Point Spread Function Calculations	28
3.1 Introduction	28
3.2 The k -sphere	29
3.3 The electric field on the k -sphere	30
3.4 Digital Fourier transformation and its pitfalls	33
3.5 Methods for computing PSFs	38
3.6 Aberrant PSF	43
3.7 Dipole emission Point Spread Functions	50

<i>CONTENTS</i>	xi
3.8 Space-variant imaging	51
3.9 Limitation of wide-field microscopy	52
4 Theoretical Analysis of the Point Spread Functions	54
4.1 Introduction	54
4.2 PSFs sensitivities to parameter mismatch	55
4.3 Comparison of different computation methods	64
5 Phase Retrieval of High NA Point Spread Function Data	73
5.1 Introduction	73
5.2 Phase retrieval algorithm	74
5.3 Phase retrieval algorithm for a high NA PSF data	77
6 Experimental Validation	79
6.1 Experimental validation workflow pipeline	79
6.2 Materials and method for PSF measurement	80
6.3 Factor for energy conservation	82
6.4 PSFs under different imaging conditions	85
6.5 PSFs for image reconstruction	92
7 Conclusion	100
Appendices	102
A Detailed computation of the optical path difference	103
A.1 Optical path difference	103
A.2 Decomposition of the phase aberration into Zernike polynomials	111
B Visualisation of the effects of aberrations on PSFs	116
C Averaging over the dipole orientations	121
D Sample preparation protocol	122
E Image quality metrics	124
List of References	126

List of Figures

1.1	Display of the lateral and axial cross section of the PSF and OTF of a 1.4 NA oil immersion objective lens and emission wavelength of 532 nm	2
1.2	Convolution of an object with a PSF	3
2.1	Diagram of an inverted wide-field fluorescence microscope	11
2.2	Geometrical representation of a 4 <i>f</i> -imaging system using the thin lens approximation	12
2.3	Introduction of the notion of the Gaussian reference sphere to warrant the Abbe's sine condition.	13
2.4	Schematic illustration of the aplanatic factor	15
2.5	Diffraction of plane waves through an aperture.	18
2.6	Field propagation from a circular aperture of diameter <i>a</i>	19
2.7	Vector field propagation from a circular aperture of diameter <i>a</i> through a high NA system.	21
2.8	Geometry of wave aberrations.	24
3.1	Fourier space representation of a plane wave from a wavelet <i>W</i> at a point source P_W in the pupil plane called McCutchen pupil	30
3.2	Illustration of the Huygens Wavelet becoming a plane wave.	31
3.3	Representation of the waves on the <i>k</i> -sphere	31
3.4	Directional change of the electric field	32
3.5	Illustration of the Fourier sampling pitfall	35
3.6	Wrap-around of using FFTs in PSF calculations	37
3.7	Diagram of the wave propagation in real space for calculating the zoom factor <i>c</i>	39
3.8	Example of a generated interpolation coefficients of k_z	41
3.9	4 <i>f</i> -imaging with a tilted object plane in real and Fourier space representation	44
3.10	Illustration of the optical path at a given design condition and under an arbitrary non-design condition at a given azimuthal angle ϕ and refracted angle in the lens system θ	47
3.11	Components of the electric field in the pupil plane from a system with a non-tilted coverslip and a system with a coverslip tilted by $\alpha = 1^\circ$	49

3.12	Display at $\gamma = 0.2$ of the lateral profiles of tilted PSFs at $\alpha = 1^\circ$ about the x -axis at the focus (left) and at a defocus position $u = 60$ o.u. (right). . . .	50
3.13	Display at $\gamma = 0.2$ of the yz -profiles of non-tilted PSF (left) and tilted PSF (right)	50
3.14	Optical transfer function in a conventional incoherent imaging system	53
4.1	yz -cross section of aberrant PSFs	57
4.2	Visualization of the focal shift and peak intensity along the optical axis at $\alpha = 0$ for different t_s and n_s/n_i values, $NA = 1.2, n_i^* = n_i = 1.33$ and $\lambda_{em} = 500$ nm	58
4.3	Representation of the focal shift in a simple imaging diagram	59
4.4	The influence of refractive index mismatch and coverslip tilt onto the OTF.	60
4.5	Projection of the real part of the OTF along k_y -axis	61
4.6	Effects of the lack of knowledge of the tilt parameters on the OTF	62
4.7	Radial mean profiles of the PSFs at the focus position in logarithmic scale	65
4.8	Observation of the violation of the missing cone by calculating and presenting the integrated intensity along z	66
4.9	Mean relative error between the gold standard RW-GS PSF and PSFs models	67
4.10	Normalized cross correlation between the gold standard PSF and PSFs models	68
4.11	Quantification of the wrap-around effect	69
4.12	Computational time of each technique per voxel in μs	70
5.1	Test of the accuracy of the phase retrieval algorithm using simulated data	78
6.1	Back focal plane re-imaging system	83
6.2	Measurement of the BFP for validating the energy conservation factor.	84
6.3	Phases of Exp-PSFs recorded with high NA objectives, and NCC and MRE between measured and simulated PSF data.	87
6.4	Display at $\gamma = 0.5$ of the xy -profiles sections at three different z -planes and yz -profiles at $x = 0$ of high NA Exp-PSF, $NA = 1.3$	88
6.5	Display at $\gamma = 0.5$ of the xy -profiles sections at three different z -planes and yz -profiles at $x = 0$ of high NA Exp-PSF, $NA = 1.4$	89
6.6	Display at $\gamma = 0.5$ of the xy -profiles sections at three different z -planes and yz -profiles at $x = 0$ of high NA Exp-PSF, $NA = 1.57$	90
6.7	Display of the yz -profiles of the Exp-PSF, and the corresponding simulated aberrant PSFs calculated from different methods: RW, SP-FFT*, SP-CZT*, F-Shell*, and Sinc-R* from $NA = 0.95$ at different values of t_g^*	92
6.8	Relative intensity profiles of the theoretical PSFs and Exp-PSF at different t_g^* along the axial axis and NCC between Exp-PSF and simulated data	93

6.9	Results from the deconvolution of a spherical bead of $2.5\ \mu\text{m}$ in diameter with non-aberrant PSFs	96
6.10	Radial and axial profiles of recovered bead	97
6.11	Results of the deconvolution of a spherical bead of $2.5\ \mu\text{m}$ in diameter with aberrant PSFs	97
6.12	Results from the deconvolution of the images of <i>C. Elegans</i> embryo using non-aberrant vPSF	98
6.13	Results from the deconvolution of the images of <i>C. Elegans</i> embryo using aberrant RW PSFs, SP-FFT*, SP-CZT*, F-Shell*, and Sinc-R*	99
A.1	Orthonormal coordinate system	104
A.2	Diagram illustrating the new coordinate system $\{\vec{u}', \vec{v}', \vec{n}\}$ for calculating the immersion medium thickness in non-design condition and the positions of B_1 and C_1	106
A.3	Determination of the segment CH	108
B.1	Wavefront error σ_W in wave unit λ_0 , MRE, NCC and Strehl ratio S of an aberrant PSF at varying sample thickness t_s ranging from $1\lambda_0$ to $9\lambda_0$ in comparison with the reference non-aberrant reference PSF	117
B.2	Wavefront error σ_W in wave unit λ_0 , MRE, NCC and Strehl ratio S of an aberrant PSF at varying sample thickness t_s ranging from $50\lambda_0$ to $250\lambda_0$ in comparison with the reference non-aberrant reference PSF	118
B.3	Zernike coefficients C_n^m at different $n_s/n_i, \alpha$ and t_s	119
B.4	Binary images which corresponds to Fig. fig:ZCoeff all higher depth representing the Zernike coefficients $C_n^m \geq 0.075\lambda_0$	120

Chapter 1

Introduction

This chapter introduces the readers to the context and research question of the study in this thesis. This study consists of investigating and modelling the impulse response, known as the point spread function (PSF), of wide-field fluorescence microscopy. An overview of the state-of-the-art and of studies that have been conducted in the direction of PSF calculation and their respective limitation is given. This is followed by a summary of the contribution made in this thesis to the field of super-resolution microscopy and the structure of the rest of the thesis.

1.1 Context and research question

Fluorescence microscopy is a well-used technical tool for research in the field of biology. It utilizes the multiplexing and specificity of fluorescence labels to image biological samples. The technique has been widely used as it enables high-resolution imaging with high contrast, and offers the possibility of recording images of different cell components with different colours [1].

Fluorescence emission can be explained in terms of energy absorption. The energy that is associated with the photon is $\hbar\mu$, \hbar is the Planck constant and $\mu = c/\lambda$, c being the speed of light and λ the photon's wavelength [1]. In the presence of external illumination at a given wavelength λ_{ex} , the fluorescent molecule is excited. A photon is absorbed resulting in a transition from the ground state to a higher energy state. The molecule in the excitation state can decay back to the ground state by fluorescing. The emitted energy during the relaxation of the molecule is lower than the excitation photons as some of the energy is lost to the molecular environment. Due to this loss, the emission wavelength is larger than the excitation wavelength. This results in a shift in the spectrum called the Stokes shift [1]. The Stokes shift is important in fluorescence microscopy to separate the fluorescence emission from the excitation light source. A filter cube containing excitation and emission filters, and a dichroic beam splitter is used to filter out the excitation light from the fluorescence of the

molecules which is detected by a camera or eye to form the desired image of the sample [2].

Fluorescence microscopy is an incoherent imaging technique. Fluorescence emission fluctuates over time and is emitted at a random phase [2]. The coherence time of the field, defined as the time under which two waves of different beams of light have a constant phase between them, is short. The temporal resolution of the detector is bandwidth limited so it is not able to detect the fluctuations of the intensity with coherent phase. Hence the probability to detect coherence in intensity measurements with a finite bandwidth detector is low. Given this, fluorescent emitters are assumed to be incoherent light sources. The intensity which corresponds to the coherence phase is negligible and can be discarded and the resulted intensity is the incoherent sum of the intensities of each individual emitter.

An optical fluorescence microscope is characterised by the point spread function (PSF). The PSF represents the response of a diffraction-limited system in the imaging of a single point-source fluorescent emitter (see Fig. 1.1a and 1.1b).

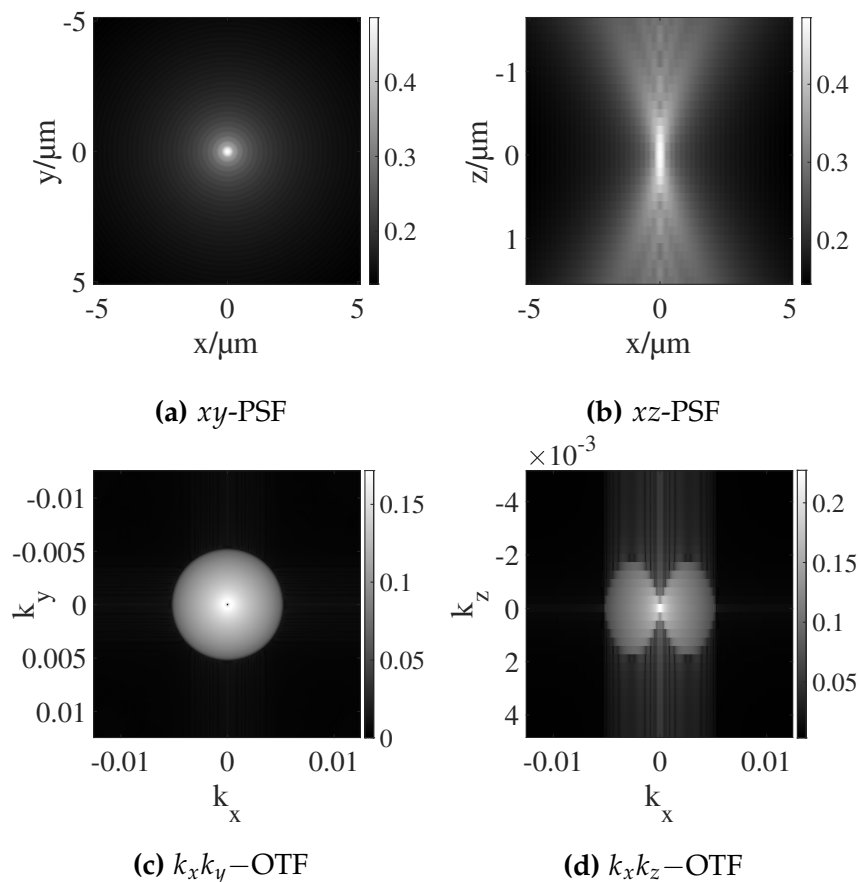


Figure 1.1: Display at $\gamma = 0.2$ of the cross section of the point spread function (PSF) along the xy (a) and xz -plane (b) at $z = 0$ and $y = 0$ respectively, and the optical transfer function (OTF) along the $k_x k_y$ (c) and $k_x k_z$ -plane (d) at $k_z = 0$ and $k_y = 0$ from an optical system with an oil immersion objective lens of numerical aperture $NA = 1.4$, emission wavelength $\lambda_{em} = 532$ nm.

The incoherent imaging can be described mathematically as a convolution of the object with the PSF where the shift-invariance properties in the system and law of superposition hold [3].

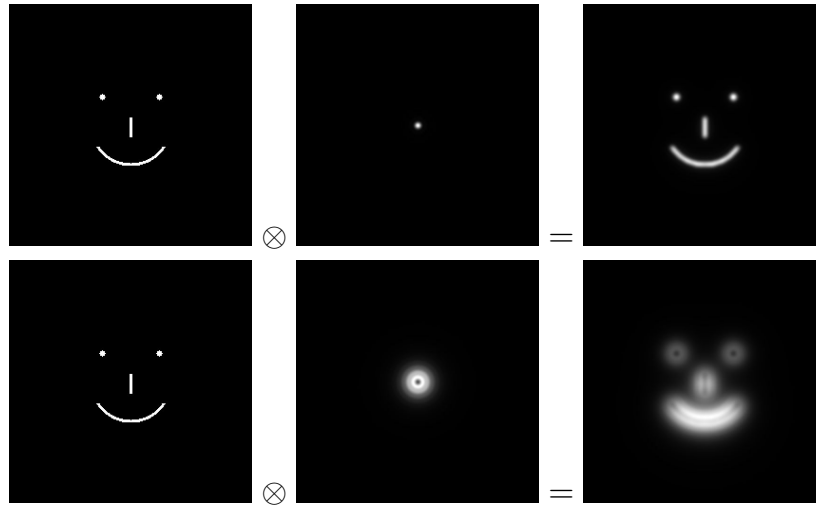


Figure 1.2: Convolution of an object O with a PSF. First column: Object O . First row and second column: in-focus PSF at $z = 0$. First row and third column: image formed by the convolution of O with the in-focus PSF. Second row and second column: out-of-focus PSF at $z = 0.6 \mu\text{m}$. Second row and third column: image formed by the convolution of O with the out-of-focus PSF at $z = 0.6 \mu\text{m}$.

With a conventional fluorescence microscope, also called wide-field, the sample object is illuminated uniformly. In a thick sample, the emitters at different depths contribute to the light intensity of the detected focal plane. In effect, the frequency component along the optical axis of the optical transfer function (OTF), equivalent to the Fourier transform of the PSF, goes missing. This missing region is commonly referred to what is called the “missing cone” (see Fig. 1.1d). The PSF is band-limited in frequency space, yielding to the diffraction limit of the optical resolution called Abbe limit [3]. Finer features in the object that are smaller than this limit will be imaged as if they are with the same size as the Abbe limit. The lateral passband of the PSF, and the missing cone, are two main reasons of the blurring in an observed image when in and out of focus (Fig. 1.2).

Many research studies are in search of ways to overcome the drawbacks of wide-field microscopy by either developing an advanced imaging technique capable of achieving an optical resolution beyond the Abbe limit and filling the missing cone region in the OTF or improving the image quality and contrast of wide-field computationally using the knowledge of the PSF.

An advanced imaging technique can be achieved in different ways such as structuring the illuminating light [4], structured excitation in combination with a spatially sensitive detection [5], switching off some fluorescence emission to reduce the width of the PSF [6], statistically switching on and off the emitters and have its precise location to

form a high resolution image [7]. These approaches can all be beneficial under particular conditions, but still have their respective drawbacks. The imaging can be time consuming if it is point scanning the sample. Some advanced techniques may require high excitation intensities that can damage the sample quickly due to phototoxicity and photobleaching. Lastly, the equipment can also be costly.

The second approach which is done computationally is called “deconvolution”. It consists of undoing the effect the PSF does in the convolution of the object to obtain the best estimate of the object from the measured image. It can, in some cases, achieve the same resolution as an advanced imaging and thus significantly improve the image quality and contrast, since it makes plausible assumptions about the object [5]. A realistic model of the PSF based on the unknown and known parameters of the optical imaging, samples and image acquisition is however required for a successful deconvolution. Calculating the PSFs is of interest not only for optical resolution improvement, but also for predicting the resulting image under a given condition. The PSF can also be experimentally reconstructed by averaging over several images of beads with size smaller than the Abbe limit. Experimental reconstruction of the PSF has the advantage of detecting aberrations that may be present in a system. However, imaging a PSF under the exact acquisition condition as the specimen is not straightforward. A wrong estimation of the noise distribution in the PSF affects the quality of the image reconstruction.

To contribute to the improvement of microscopic image data quality and respond to the research question: *“how to achieve a high resolution imaging with a good contrast while avoiding the drawbacks of advanced imaging technique?”*, we believe one answer consists of developing *effective ways for computing the PSF of a wide-field system under realistic condition*, and demonstrate *the efficiency of the PSFs for image reconstruction*.

1.2 Current state of the art

The first step to computing the PSF of a given optical imaging system consists of studying the image formation, and thus the impulse response. This study has been the focus of many research groups around the world since the days of Ernst Abbe (1840 - 1905) [8, 9]. These studies range from the theoretical study and derivation of the analytical expression of the impulse and frequency response of a system, to the experimental study and validation of the theory. An analytical expression of the PSF is derived theoretically under a given set of assumptions and approximations based on the diffraction theory of light. The accuracy of each PSF model depends on these assumptions and approximations.

Hopkins is among the first scientists to study the frequency response or optical transfer function (OTF) of an optical system [10]. His work focused on a system which is free of aberration other than defocusing effects. His calculation of the OTF is in terms

of Bessel functions. Hopkins's model is valid under the Fresnel-Kirchhoff boundary condition. This assumes that the field outside the pupil is zero and the diffraction by the pupil itself can be neglected [10, 11]. The Rayleigh-Sommerfeld expression of the diffraction represents the exact scalar amplitude field [12]. The Fresnel-Kirchhoff solution to wave propagation is a paraxial approximation of the Rayleigh-Sommerfeld solution [13, 14, 15, 16]. This corresponds to the scalar diffraction of light formed by converging spherical waves.

Several followed the work of Hopkins in the investigation of the OTF such as Stokseth [17], Sheppard and Gu [11], and Hiraoka et al. [18]. These studies theoretically and experimentally investigated properties of a defocused optical system with incoherent illumination [17], and in a more advanced technique using epifluorescence microscopy [18]. The imaging models were compared to results from geometrical optics. It is concluded that geometrical optic is a poor representation of an optical system, and a diffraction theory of the imaging is required especially at high numerical aperture (high NA). The need for a more accurate theoretical model was also concluded as a large deviation of the theoretical model from the experimental was observed [18]. A review of the diffraction pattern of a circular aperture based on previous findings, and the off-axis imaging for systems of low and large Fresnel number, was conducted by Gibson and Lanni [19]. This investigation of the image formation and off-axis imaging was established by describing the OTF of the system and the frequency components of a 3D object that is transferred by a given optical system based on Born-Wolf formulation [20]. It is concluded from this formulation that the image formation is a convolution of the object distribution with the response of the optical system.

Another study by Streibl was conducted in the year of 1985 to investigate the image formation from a scattering object with partially coherent illumination under the first-order Born approximation [21]. He discussed the limiting factor of the imaging and the reasons for missing frequency components in the OTF. He found that the high coherence in the illumination light worsens the image quality [21]. This demonstrates the benefit of incoherent optical imaging such as fluorescence microscopy over coherent imaging.

The phase aberration due to the non-design parameters was first introduced by Gibson and Lanni [22]. This phase aberration is calculated in terms of the optical path difference (OPD) between the design and non-design conditions of the system. A design condition represents the image acquisition condition at which the optical system was designed for while non-design condition is the real acquisition condition. The analytical finding calculated from Kirchhoff's scalar diffraction model was tested experimentally under the assumption of shift-invariance and linearity in the system. The experiment has proven the model of the aberrations to be accurate [22]. Although a scalar model is easy to implement, it does not account for the vector feature of light

such as polarization and the direction of the energy flow [23]. Given the Fresnel-Kirchhoff boundary condition in the model, scalar diffraction theory is also limited to low NA .

Although Fresnel wave propagation is fast as it requires only one Fourier Transform (FT) to compute, wave propagation under the Fresnel approximation is only accurate in the paraxial approximation, i.e. for low NA systems [13, 14]. The angular spectrum of plane waves (ASPW), also called Fourier propagation in different literature, is an accurate technique for computing wave propagation [14]. However this technique can be expensive in time as it requires two FTs to calculate the propagation operation. The ASPW has also been proven to result to the same wave propagation as the Rayleigh-Sommerfeld integral under the same boundary conditions [15]. ASPW is well suited for high NA system. Engelberg explored the physical optics propagation to derive a new efficient technique for wave propagation in high NA system by avoiding the paraxial approximation relative to the propagation distance along the optical axis z in the Rayleigh-Sommerfeld diffraction integral [16]. This new formulation goes beyond the Fresnel approximation.

Although a solution can be found to accommodate high NA in a scalar diffraction formulation, the polarization of light and the direction of energy flow cannot be taken into consideration in a scalar formulation. Richards and Wolf calculated the vector diffraction response of an aplanatic and aberration free optical system [23, 24]. Török et al. reformulated the Richards and Wolf (RW) model to include spherical aberration due to refractive mismatch with a planar interface and the transmission coefficients of the interface [25]. A further study was developed later to derive an analytical solution to the diffraction integrals and decomposition of the spherical aberration by Zernike polynomials [26]. This aberration decomposition is of interest in understanding any defect induced by the non-design parameters and aberrations. The model was generalized to accommodate a stratified medium composed of N -layers of different refractive indices [27]. The polarization state in the image plane and polarization fluorescence microscopy were also investigated [28].

The RW model has been chosen by many as the ground truth for calculating the PSF as it is the most rigorous among existing models so far, and is derived from Maxwell's equations [29, 30, 31, 32, 33]. The integrals in its formulation are however expensive to compute. Several attempts have been made to speed up the computation by approximating the continuous integral in terms of series. Kant solves the diffraction integral by expanding it into a series of Gegenbauer polynomials of the first kind [29]. A review of other computational methods was drafted by Foreman [31]. In this review, series representations of the model in terms of eigenfunctions, multipole expansions and an approximation of the spherical wavefront into a paraboloidal wavefront are presented. A trade-off between the accuracy and computation speed is made. Although the computation using these approximations is fast and the con-

vergence is rapid, its accuracy is correlated to the degree of the polynomials or the number of expansions. There is however a threshold to this correlation. A very high number of expansions can also over-approximate the model and worsen the fit in the focal region. Another disadvantage of the approximation into developed series and component-wise expansion is the fact that the Maxwell's equations may not be satisfied as each component of the electric field is expanded separately, and different errors and approximations might be induced [31]. Lastly, these approximations including the expansion of Kant [29], are valid such that the pupil plane is symmetric. This means that any aberration that is not radially symmetric is not yet included in these formulations.

Developing methods for computing an accurate and efficient PSF is still not a solved problem, especially in the digital age. Li et al. implemented the scalar PSF model based on the theory developed by Gibson and Lanni [22, 34]. The Fresnel-Kirchhoff diffraction integral is approximated in terms of Bessel series and the computation is found to be efficient in time [34]. The algorithm accounts for the spherical aberration due to any refractive mismatch in the system and radial symmetry property of the PSF. Thus, it does not consider any asymmetric aberration that may be present in the system. The PSF models under the PSFGenerator toolbox developed by Kirshner et al. [33], and based on the RW formulation [24] was used as state-of-the-art technique to validate the model of Li et al. [34]. This state-of-the-art PSF model has been widely used for deconvolution [35, 36]. Based on our experience, the software does not support larger grids. In other words, it is not memory efficient. In this thesis, these models will be used for comparison with newly developed methods.

Aguet et al. also developed a MATLAB MEX, a MATLAB function that calls a C code, for calculating vectorial as well as scalar PSF models [37]. These methods exploit a numerical integration based on Simpson's rule to compute the diffraction integral [37]. Samuylov et al. developed a technique for computing a PSF based on a sparse Gaussian mixture [32]. This later model is obtained by combining several weighted single Gaussian kernels shifted to different positions. Its efficiency and accuracy depend on the number of Gaussian functions used. At the time of the submission of this thesis, the PyFocus is the most recent package for computing a fully vectorial numerical calculations of the PSF to the best of our knowledge [38]. The package was written with Python programming language and in an open source format. Since this package was only discovered during the final stage of the revision of the thesis, we were not able to conclude about its pros and cons.

The quality of a model is measured in terms of its accuracy, computation time, its vector features, and the computation method such as for instance inclusion of radial symmetry. Analytical and theoretical PSF models are validated experimentally by imaging beads of size smaller than the diffraction limit and averaging over the images of several beads. By investigating theoretically and experimentally the effects of

refractive index mismatches in confocal microscopy, Hell et al. predicted a drop in intensity in the PSF, focal shift and change of optical resolution due to refractive index mismatches [39]. Sheppard and Török later investigated the same effects on confocal imaging [40]. Haeberlé [41] conducted an experimental validation of the rigorous vector formulation of the diffraction of an optical system by Török et al. model [26] with the OPD formulated by Gibson and Lanni [22]. Ghosh and Preza extended the experimental evaluation of the algorithm similar to the one formulated by Haeberlé in [41] by accounting for stratified medium composed of more than one layer of sample of a given refractive index and thickness in the sample region [42]. This consideration is done over a given small block in space of the sample region, not the whole space. This shift-invariance condition holds within that small block.

Many parameters of the PSF model in an experimental setting are unknown and a realistic model which fits the reality is required. Each of the PSF models still has its own pros and cons. Existing PSF calculations are either based on insufficient models or contain inaccuracies such as a non-uniform integral close to the focus position. *A strategic and unified comparison of various ways to implement PSF generation models is still missing in the field.*

In this thesis, *we analyse, in depth, the state-of-the-art in PSF calculation, their limitations and present new efficient ways for calculating realistic PSFs. We also developed four PSF models, two of which are totally new to the best of our knowledge. The first two models use the angular spectrum method to propagate the field in free space while the two other methods use different techniques to propagate the field in three-dimensional space. Three of the models are Fourier-based. The Fast Fourier-transform is a very handy tool to speed up PSF calculations, but its pitfalls have to be carefully avoided (e.g. caused by the cyclic borders and discrete sampling in Fourier space). One of the four methods uses the chirp-Z method that has been used in the literature to avoid the pitfalls of the FFT without any loss of accuracy [43, 44]. The theoretical models are validated experimentally and their efficiency for image reconstruction is compared.*

A tilt due to any misalignment, imperfection in the optical system or simply a poorly mounted coverslip can change the PSF pattern and so the image quality dramatically. A study of tilted plane, a tilted stratified medium to be more precise, has been included in the optical diffraction calculation conducted by Matsushima et al. [45]. In our work, we expand this study by *including also the OPD induced by the tilted stratified medium and account for the effect of the tilting in the 3D spectrum in Fourier space. The OPD is decomposed into Zernike polynomials to quantify the single aberration present in the system due to the tilt.* This particular study is of a great interest in understanding and predicting image formation. It can also be used for quality control of an optical system.

The software code developed under this project for calculating the PSF of a wide-field microscope under a realistic condition is written with MATLAB programming lan-

guage. *This code will be released with the first manuscript from this thesis in an open source format.* We believe this toolbox will contribute to the advancement of optical modelling and image reconstruction. The source code is reproducible and can be easily adapted to include different modes of the most advanced fluorescence techniques.

1.3 Outline of the thesis

The rest of the thesis is organized as follows:

Chapter 2: We discuss the theoretical background for studying and calculating PSF. This background ranges from the description of optical apparatus and the different imaging conditions that need to be satisfied, diffraction theory and propagation of light to the description of image formation and image reconstruction.

Chapter 3: We present our newly developed techniques for calculating PSFs. We report each necessary ingredient, including possible tilting in the optical system, for drafting the algorithms for computing the PSFs. Additionally, we present the formulation of a dipole emission PSF. Moreover, we extend the formulation of the PSF to account for the space-variance property. A brief discussion of wide-field imaging concludes this chapter.

Chapter 4: We analyse the sensitivities of the PSFs and OTFs to a deviation of its parameters from the design conditions. A unified comparison of the newly developed PSFs and the state-of-the-art is also conducted.

Chapter 5: Experimental validation of the theoretically developed PSF requires the recording of experimental PSF, which is never aberration free. Here we present a newly adapted phase algorithm to estimate the phase from experimental PSF in order to adopt a proper comparison of the theory with experiment.

Chapter 6: The theoretical PSFs models developed under this project are validated experimentally.

Chapter 7: We conclude the thesis with an overview of the methods discussed and future work.

Chapter 2

Theoretical Background

For a better understanding of the underlying principles of light microscopy and point spread function calculation, it is important to discuss the properties of light itself and the mathematical formulation of image formation. This constitutes the focus of this chapter.

2.1 Image formation

2.1.1 Optical apparatus of a wide-field fluorescence microscope

Optical microscopy is an important tool in scientific research. A microscope is a device which can help to visualize an object that cannot be seen with naked eye such as bacteria. It is basically composed of a sample stage holding the specimen, a light source to illuminate or excite the sample, an objective lens (OL) to collect the emitted light from the sample. Most modern fluorescence microscopes have a tube lens to form the primary image of the sample and use a camera to record the image. The camera converts photons into an electrical signal containing spatially-resolved intensity information of the incident light. The digitized output of the camera is then input into a computer to display the image of the sample. The image quality is characterized by the optical system parameters: immersion medium and numerical aperture NA of the OL, the emission wavelength λ_{em} of the emitter, the excitation wavelength λ_{ex} of the light source, the optical and physical properties of the sample, and the sensitivities of the detector or camera. In fluorescence microscopy, a laser is often used as an illuminating light source. Lasers are a source of a coherent and monochromatic light. The sample to image is stained with fluorophores. In widefield microscopy, the sample is illuminated uniformly (see Fig. 2.1). Fluorescence emission upon excitation of the fluorophores may be detected by a digital camera to form the image of the specimen.

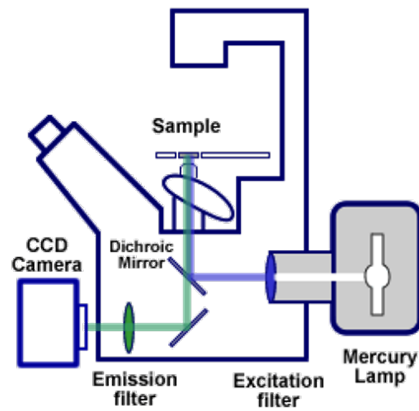


Figure 2.1: Diagram of an inverted wide-field fluorescence microscope [46]. The blue light path represents the excitation light while the green channel represents the fluorescence emission in this figure. A dichroic mirror is used to filter out the excitation light from being detected by the CCD camera.

2.1.1.1 Detection systems

To avoid artefacts due to photobleaching, and for live samples, phototoxicity, the sample is illuminated at a fairly low power. As a consequence, the fluorescence signal is weak and can be difficult to detect [1]. A sensitive detection system is thus required to acquire data with high signal-to-ratio (SNR). The choice of a detection system mainly depends on its application. Some imaging would require high-speed detection but usually at the cost of the spatial resolution, while other detection system might be slow, but is more sensitive to weak signal. The characteristic parameters of detection systems are its quantum efficiency (QE), gain, and spatial and temporal resolution. The quantum efficiency indicates the ability of the detector to convert photons to electronic charge. It is wavelength dependent. The electronic charge is afterwards converted to a voltage value which in turn is digitized to levels of brightness in the output image. Weak fluorescence signal may contain useful and important information that may need to be amplified before digitization. The gain of a camera characterizes this signal amplification. The spatial and temporal resolution of a camera are also worth considering. Its spatial resolution must match the optical resolution of the system to detect the smallest feature that is present in the emitter and is resolved by the system. An appropriate detection speed is important to temporarily resolve the occurrence of specific event from the emitter. A long exposure time may reduce the noise and enhance the present signal but may lead to losing information on events occurring on time-scales smaller than the exposure time. In any type of imaging which requires a scan over the sample or the image plane, this parameter is important.

2.1.1.2 Statistical noise models

From photon emission to image digitization, the three most dominant types of noise that can be detected, accumulated, and also digitized in fluorescence microscopy are photon noise, electronic noise, and readout noise [47]. Photon noise is also called fluorescence noise or shot noise. It is determined by the fluctuation of the photon emission and its arrival at the detector. It follows the Poisson distribution. Electronic noise arises in the detector. It includes noise accumulated over time due to thermal vibration of electrons. This type of noise is also called dark current or dark noise in other literature [48]. As the signal is transferred, noise is also transferred and gets amplified with the signal. An additional noise called readout noise is added during this process of quantization of the electronic signal.

2.1.2 The Abbe sine condition

There are different conditions that a system need to satisfy depending on the purpose of the optical system [49]. In a perfect imaging system, a plane is imaged onto a plane without acquisition of any phase aberration [3]. This is achieved by satisfying the Abbe sine condition [3]. The Abbe sine condition ensures the image intensity invariance along the lateral axis. Given this condition, the pupil in the back focal plane (BFP) is evenly spaced when it is made discrete. If the optical system does not satisfy this condition, the pupil gets distorted. To understand the concept, we simplify the diagram in Fig. 2.1 with a simple $4f$ -imaging system (see Fig. 2.2). We assume a point-like object emitting light isotropically in 4π -direction as emitter. The propagating spherical wave can be approximated by many finite plane waves. The direction of a finite plane wave is given by the wave-vector \vec{k} which forms an angle θ_{em} about the optical axis (see Fig. 2.2). As the light propagates through the optical system, the wave-vector in the detection side forms an angle θ_{det} about the optical axis.

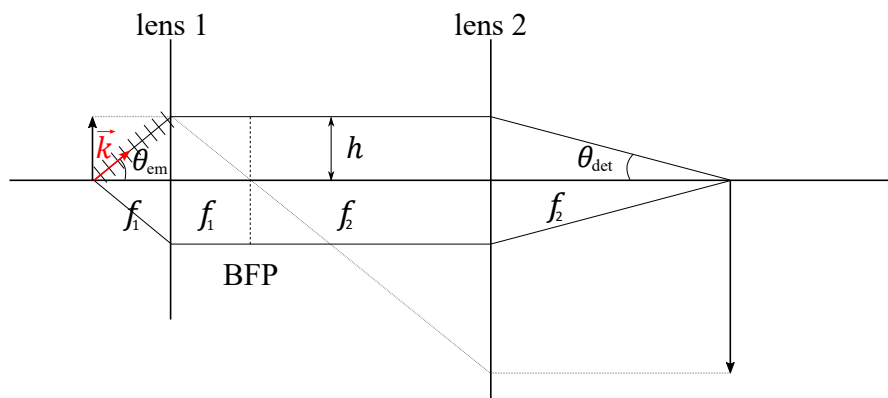


Figure 2.2: Geometrical representation of a $4f$ -imaging system using the thin lens approximation. BFP stands for back focal plane. Here lens 1 with focal length f_1 corresponds to the microscope objective lens while lens 2 is associated with the tube lens with focal length f_2 .

From the drawing in Fig. 2.2, the invariance is of $\tan \theta_{em} / \tan \theta_{det} = f_2 / f_1$, which corresponds to the Helmholtz condition [49]. Under this condition, the equivalent refractive locus is a plane, f_1 and f_2 being the focal lengths of the objective lens (lens 1) and tube lens (lens 2) respectively. This surface is defined as the wavefront at the surface where the waves bend due to the lens from the surface normal to the optical axis to the direction towards the focal point. The plane equivalent refractive locus corresponds to the plane indicated by the position of lens 2 in Fig. 2.2. The Helmholtz condition holds and of importance in paraxial optical systems.

For high NA imaging, the Abbe's sine condition is more accurate [3, 24, 49]. The notion of Gaussian sphere is introduced to fulfill it. A Gaussian reference sphere is a sphere of radius equal to the focal length and centred at the Gaussian points which are either the emitter position in object plane or the nominal focus in image plane [3]. Here, the radius of the Gaussian sphere in the object and image planes are f_1 or f_2 respectively. Under this condition, the finite plane waves propagate to the Gaussian reference sphere and get projected to the reference plane without acquiring any extra phase. The same principle is applied in reverse to the tube lens (lens 2 in Fig. 2.3).

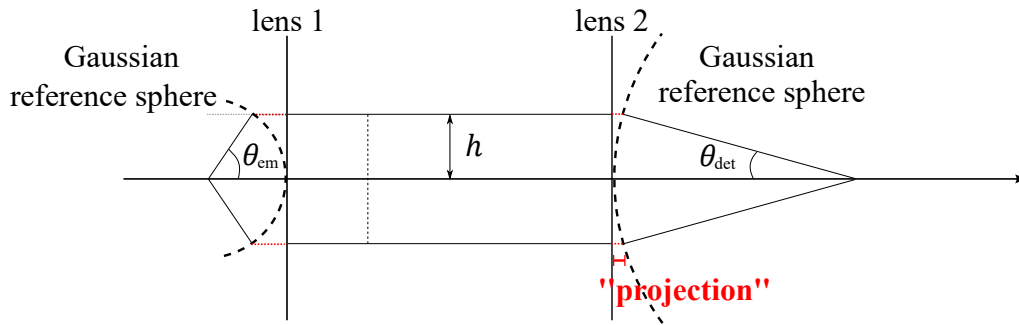


Figure 2.3: Introduction of the notion of the Gaussian reference sphere to warrant Abbe's sine condition. "Projection" refers to direction of the beams at the connected surface without acquiring any phase for the space in between the plane surface and the sphere.

For a small lateral shift Δx in the object plane, the residual optical path difference (OPD) between the change in path in the object plane and in the image plane, is given as follows:

$$\Delta x = n_1 f_1 \sin \theta_{em} - n_2 f_2 \sin \theta_{det}. \quad (2.1.1)$$

We have n_1 and n_2 the refractive indices in the object and image space respectively, and Δx is the lateral displacement. The residual path Δx must be zero to satisfy a lateral shift invariance in a system. This yields to the Abbe sine condition which relates the angles θ_{det} and θ_{em} :

$$\frac{n_1 \sin \theta_{em}}{n_2 \sin \theta_{det}} = \frac{f_2}{f_1} = M, \quad (2.1.2)$$

M being the magnification of the optical system.

This introduction of Gaussian reference sphere requires the consideration of the energy conservation which is discussed further down in the next Section 2.1.3.

2.1.3 Aplanatic correction

In response to the imaging condition invariants, an aplanatic factor needs to be taken into consideration. This factor corresponds to the apodization function (see Eq. (2.2.24)). A system is aplanatic if it is free from spherical and coma aberration. Any lateral displacement of the system inside an aplanatic region centered at the optical axis does not induce any aberration to the system [50]. An aplanatic system forms a perfect image. While satisfying this condition, the energy must be conserved. In reference to Fig. 2.4 for instance, integrating over the radial position r in the BFP must yield to the same quantity of energy as integrating over the angle θ in the equivalent refractive locus [49].

As discussed in Section 2.1.2, the corresponding equivalent refractive locus is a Gaussian reference sphere of radius equal to the focal length of the lens for a system satisfying the Abbe's sine condition. Under this condition, the apodization or aplanatic factor (AF) is $\sqrt{\cos(\theta)}$ [49]. Without loss of generality, we restrict ourselves to the effect of a radial displacement from the optical axis of the beamlet.

2.1.3.1 Emission path

The aplanatic correction can be understood by considering once again transverse finite plane waves propagating parallel to the optical axis and redirected to the nominal focus which is at the centre of the Gaussian reference sphere. Assuming a lossless system, the power P_1 of an incident beamlet distributed on an elementary area A_1 is projected onto a larger area A_0 of the spherical area such that $A_1 = A_0 \cos \theta$ (see Fig. 2.4). This implies that the irradiance I_1 of the beamlet measured at A_1 , which is defined as the power per area, is proportional to $I_0 / \cos \theta$, I_0 being the irradiance measured at A_0 .

The positive direction of z is indicated by the direction of the arrow in Fig. 2.4. Towards this direction, we have an effect of concentrating irradiance to a smaller area (A_0 to A_1). It corresponds to the emission path where the wave propagation occurs from the object plane, defined to be at Ξ_0 , to Ξ_1 , a plane parallel to the pupil plane. In the imaging of an isotropic emitter, the energy on the Gaussian reference sphere is uniformly distributed. The electric field in the pupil plane therefore needs to be scaled by $1/\text{AF} = 1/\sqrt{\cos \theta}$ to conserve the energy. The aplanatic effect in the detection path can often be neglected due to the usually large magnification of the objective lens and large focal length of the tube lens. This leads to small values of θ_{det} compared to θ_{em} , and the corresponding cosine tends to 1 (see right side of Fig. 2.3). In a demagnifying imaging system, the detection angle θ_{det} is significant compared to θ_{em} . The aplanatic

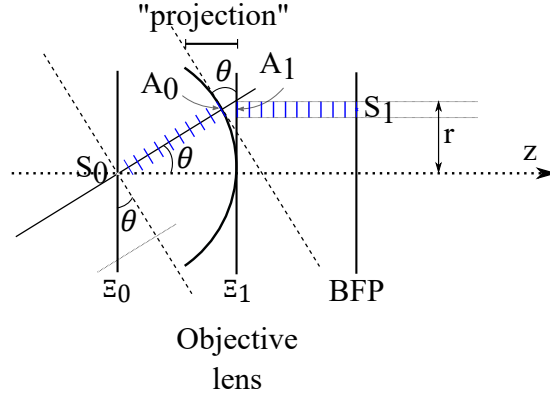


Figure 2.4: Schematic illustrating the “aplanatism effect”. The two planes Ξ_0 and Ξ_1 are parallels and are perpendicular to the optical axis. The area A_0 is a projection of the elementary area A_1 of the plane Ξ_1 onto the Gaussian reference sphere.

factor cancels out and is equal to 1 if the magnification of the system is 1. The general formulation of the aplanatic factor (AF) in amplitude field is given by:

$$AF_{amp} = \sqrt{\frac{\cos \theta_{em}}{\cos \theta_{det}}}. \quad (2.1.3)$$

The subscript *amp* simply indicates that the AF in Eq. (2.1.3) applies to amplitude field not intensity. In Section 6.3, we validate experimentally the theory of the aplanatic factor discussed in this section. In this experimental validation, the tube lens possesses a larger focal length than the objective lens, which is the case of most modern optical systems in the field of fluorescence microscopy [51].

2.1.3.2 Excitation path

However, to base the argument on the reciprocity theorem: a monochromatic optical system in which a field $(E_{x_0}, E_{y_0}, E_{z_0})$ at position S_0 gives rise to a field $(E_{x_2}, E_{y_2}, E_{z_2})$ at position S_2 in the image plane, will guarantee that generating $(E_{x_2}, E_{y_2}, E_{z_2})$ at position S_2 results in a field of $(E_{x_0}, E_{y_0}, E_{z_0})$ at position S_0 [49]. For an excitation point spread function (PSF), the excitation light is collected by the tube lens with a low NA and is focused onto the sample by an objective lens with high NA . The beam in the BFP can therefore be approximated to be parallel and uniform in the 2D pupil plane. Its bijective correspondence to the 3D frequency spectrum of the object plane is uniform. The projection of this 3D frequency spectrum onto the 2D pupil plane leads to a factor $1/\cos \theta$ on that plane. By passing by the objective lens (direction: S_1 to S_0 in Fig. 2.4), the aplanatic factor of the system which is equal to $\sqrt{\cos \theta}$ applies. The total factor that needs to be applied for a correct conservation of the energy is therefore equal to $\sqrt{\cos \theta} \times (1/\cos \theta) = \sqrt{\cos^{-1}(\theta)}$.

These imaging condition invariants are necessary for a correct calculation of the PSF. In the next section, the diffraction theory of light under these conditions are presented.

2.2 Diffraction theory of light

2.2.1 Maxwell's equations

In classical optics, the quantum effects such as particle and wave duality, and entanglement are not considered. Light is an electromagnetic field and its behaviour is governed by Maxwell's equations. Light has the ability to change the property of matter. Matter is optically characterized by its behaviour when an external field is applied to it and how the electric field propagates throughout it. The wave propagation depends on the properties of matter and its interaction with light. The representation of a light-matter interaction consists of a set of interaction with many point charges. The effective macroscopic Maxwell's equations are given as follows:

$$\nabla \cdot \vec{D}(r, t) = \rho_{\text{ext}}(r, t) \quad \text{Gauss's law} \quad (2.2.1)$$

$$\nabla \cdot \vec{B}(r, t) = 0 \quad \text{Gauss's law for magnetism} \quad (2.2.2)$$

$$\nabla \times \vec{E}(r, t) = -\frac{\partial \vec{B}(r, t)}{\partial t} \quad \text{Faraday's law of induction} \quad (2.2.3)$$

$$\nabla \times \vec{H}(r, t) = \vec{J}(r, t) + \frac{\partial \vec{D}(r, t)}{\partial t} \quad \text{Ampere's law} \quad (2.2.4)$$

where r and t are spatial and temporal position at which the fields are evaluated, ρ_{ext} is the source charge density, \vec{J} is the macroscopic current density, \vec{D} and \vec{H} are the electric and magnetic field flux density respectively [3]. The electric flux density is proportional to \vec{E} and the dielectric polarization \vec{P}_d such that $\vec{D} = \epsilon_0 \vec{E} + \vec{P}_d$, ϵ_0 being the dielectric constant of vacuum. The magnetic field and magnetic field flux density are linked by the relation: $\vec{B} = \mu_0 \vec{H}$ in nonmagnetic material, with μ_0 is the magnetic permeability of vacuum. Gauss's law describes that the flux density of the electric field \vec{E} is also proportional to the charge density of the enclosed surface. As opposed to the electric field, Gauss's law in Eq. (2.2.2) states that there is no magnetic monopole. The total magnetic flux is zero and the magnetic field \vec{B} is always attributed to a dipole. Faraday's law of induction and Ampere's law define the interconnection between \vec{E} and \vec{B} . A time-varying in \vec{B} induces \vec{E} and vice-versa. It is also observed from the Ampere's law that a change in the current per unit area can influence the circulation density of \vec{B} and so the electric field \vec{E} . Substituting the expression of \vec{B} in Faraday's law of induction by the expression in the Ampere's law, we have the general wave equation which corresponds to the electric field as:

$$\nabla \times \nabla \times \vec{E} - \mu_0 \epsilon_0 \frac{\partial^2 \vec{E}(r, t)}{\partial t^2} = \mu_0 \frac{\partial \vec{J}(r, t)}{\partial t} + \mu_0 \frac{\partial^2 \vec{P}_d(r, t)}{\partial t^2}, \quad (2.2.5)$$

The right hand side (RHS) of Eq. (2.2.5) relates to the medium. The current density \vec{J} and \vec{E} are linked by Ohm's law $\vec{J} = \sigma \vec{E}$, with σ being a tensor [3].

In the realm of linear optics, this current project primarily considers dielectric media with no free charges which implies that there is no variation of ρ_{ext} in time, $\sigma = 0$.

Hence, $\vec{j} = \vec{0}$ and $\nabla \cdot \vec{D} = 0$. Thus, the wave equation described in Eq. (2.2.5) reduces to the Helmholtz equation for a linear, isotropic, homogeneous and dispersive media:

$$\nabla^2 \vec{E}(r, t) - \frac{n^2}{c^2} \frac{\partial^2 \vec{E}(r, t)}{\partial t^2} = 0, \quad (2.2.6)$$

with $c = \frac{1}{\sqrt{\epsilon_0 \mu_0}}$ is the speed of light in vacuum, and $n = \sqrt{\epsilon/\epsilon_0}$ is the refractive index of the medium in which the wave is propagating, ϵ being the dielectric constant of the medium. Two particular solutions to the Helmholtz equation for the electric field are plane and spherical waves represented as:

$$\vec{E}(r, t) = \mathcal{R}\{e^{i(\vec{k} \cdot \vec{r} - \omega t)}\}, \quad \text{plane wave;} \quad (2.2.7)$$

$$\vec{E}(r, t) = \mathcal{R}\left\{\frac{1}{r} e^{i(\|\vec{k}\| \cdot \|\vec{r}\| - \omega t)}\right\}, \quad \text{spherical wave;} \quad (2.2.8)$$

with $\mathcal{R}\{x\}$ being the real part of x , \vec{k} the complex wavevector such that $k^2 = \|\vec{k}\|^2 = k_x^2 + k_y^2 + k_z^2$, $k = nk_0$ is the wavenumber in the medium of refractive index n , $k_0 = 2\pi/\lambda_0$ is the free-space wavenumber, $\lambda = \lambda_0/n$ is the wavelength and ω the angular frequency. Unless we talk about vector diffraction, we omit the arrow in the expression of \vec{E} for simplicity in the following formulation. To understand the dispersion relation of the wave, the proposed solution to the wave equation is inserted in Eq. (2.2.6) and we obtain the dispersion relation:

$$k_x^2 + k_y^2 + k_z^2 = \frac{\omega^2 n^2}{c^2}. \quad (2.2.9)$$

The refractive index n is function of the angular frequency ω and can be complex. Therefore, it defines the properties of \vec{k} . If the imaginary part of \vec{k} is not zero, a decay in the electric field is induced:

$$E(r, \omega) = e^{i(\mathcal{R}\{\vec{k}\} \cdot \vec{r} - \omega t)} e^{-\mathcal{I}\{\vec{k}\} \cdot \vec{r}}. \quad (2.2.10)$$

This decaying factor $e^{-\mathcal{I}\{\vec{k}\} \cdot \vec{r}}$ corresponds to evanescent waves. $\mathcal{I}\{x\}$ indicates the imaginary part of x . The condition for an homogeneous and evanescent waves are therefore given by:

$$\text{If } k_z^2 \geq 0, \quad k_0^2 \geq k_x^2 + k_y^2 \quad : \text{ homogeneous wave} \quad (2.2.11)$$

$$\text{If } k_z^2 < 0, \quad k_z \in \mathbb{C} \quad : \text{ evanescent wave} \quad (2.2.12)$$

2.2.2 Propagation and diffraction of monochromatic waves

To describe the propagation and diffraction of monochromatic waves, let S_0 be a source of a plane wave placed at infinity, Ξ_a is the plane where an aperture of width a is placed and $P(x, y, z)$ is a point on a plane Ξ_P placed at a distance equal to Δz

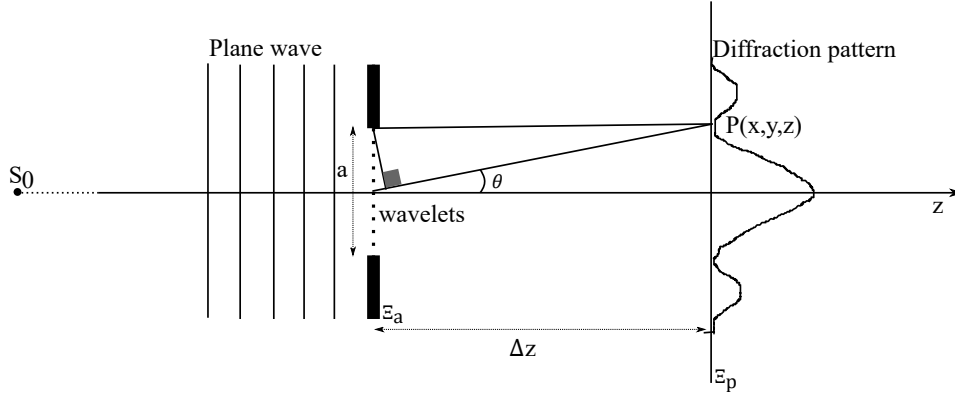


Figure 2.5: Diffraction of planes waves through an aperture.

behind the aperture. The wave propagates the distance Δz and the diffraction pattern is evaluated at P (see Fig. 2.5).

From Huygens-Fresnel principle, each point of the wavefront at the aperture of Ξ_a becomes secondary source of spherical wave. The diffraction pattern formed on Ξ_p is a linear superposition of the Huygens wavelets: constructive and destructive interference depending on the phase difference between the waves. The first minimum of the diffraction pattern is the position where the wave at the edge of the aperture and the wave along the optical axis interfere destructively (position indicated by the point P in Fig. 2.5). This process is mathematically a convolution between the electric field at the boundary of the aperture and the Huygens wavelets [3]:

$$E(x, y, z) = E(x, y, z_a) \otimes K_H, \quad (2.2.13)$$

where z_a and z_p are respectively the axial position at the aperture of plane Ξ_a and the plane of observation, Ξ_p , where the point P is, \otimes is the convolution operator, and K_H is the Kernel of the Huygens wavelets. A convolution in real space corresponds to the multiplication of the Fourier transform of $E(x, y, z_a)$, denoted by $\tilde{E}(k_x, k_y, z_a)$, with the transfer function which corresponds to the Huygens wavelets. The time-independent beam diffraction can therefore be formulated as the angular spectrum of plane waves given by:

$$E(x, y, z) = \iint_{-\infty}^{\infty} \tilde{E}(k_x, k_y, z_a) e^{ik_z z} e^{i(k_x x + k_y y)} dk_x dk_y, \quad (2.2.14)$$

where $e^{ik_z z} = \mathcal{F}\{K_H\}(k_z)$ is the transfer function which corresponds to the Huygens wavelets, $\mathcal{F}\{x\}$ is the Fourier transform of x . This term is known as the propagator in our formulation for calculating the PSF in Chap. 3. The term $\tilde{E}(k_x, k_y, z_a)$ represents the pupil field distribution.

From Eq. (2.2.14), the formulation and accuracy of the diffraction pattern depends on the approximation used. This expression describes a scalar field. It can be generalised to a vector formulation when the field polarization is considered.

2.2.3 Scalar diffraction model

Scalar field approximation does not account for the vector feature of light. To differentiate a scalar diffraction model from a vector model, let us consider the diagram displayed in Fig. 2.6, which is a 3D display of Fig. 2.5. The image plane in Fig. 2.6 corresponds to the plane Ξ_p in Fig. 2.5. The plane Ξ_a of Fig. 2.5 is at the lens position in z for a system satisfying the paraxial approximation and the Helmholtz condition as described in Section 2.1.2. This is the case for a low NA system. If the system satisfies the Abbe sine condition, the sphere on the right side of the lens represents the equivalent refractive locus on which the field from the pupil plane gets projected before it converges to the nominal point. In a scalar field approximation, the field is assigned to point in space without consideration of its orientation (see Fig. 2.6). In a vector field approximation, at each point in space, the polarization state of the electric field can change and must be taken into consideration.

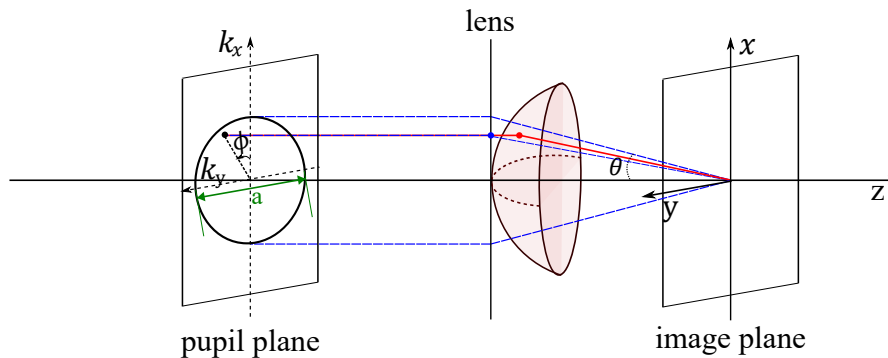


Figure 2.6: Field propagation from a circular aperture of diameter a . In a low NA system satisfying the paraxial approximation, the waves follow the path indicated by the blue dashed lines. With a high NA system where the Abbe sine condition needs to be satisfied, the waves get projected onto the sphere and follow the red path instead.

In the paraxial approximation, the inclination angle, θ , from the object plane as well as towards the image plane with respect to the optical axis, is assumed to be small enough so $\sin \theta = (k_x^2 + k_y^2)/k_0^2 \approx \theta$ (see Fig. 2.5). In this case, the spatial frequency $k_z = \sqrt{k_0^2 - k_x^2 - k_y^2}$ can be approximated using the Taylor expansion of degree 2 to obtain:

$$k_z \approx k_0 - \frac{k_x^2 + k_y^2}{2k_0}. \quad (2.2.15)$$

This approximation enables the derivation of paraxial-Fresnel near-field diffraction. If the field is evaluated at a far distance *i.e.* $z \gg a^2/\lambda$ from the aperture, the far-field Fraunhofer diffraction is obtained [14]. The Kirchoff's boundary condition, which corresponds to the contribution of the field outside the opening of the aperture being neglected, can be applied if the width of the aperture is large compared to the wavelength [14]. In this case, the limit of integrations reduces to the width of the aperture.

The representation of the scalar diffraction model for low numerical aperture systems can therefore be approximated and derived by considering a circular aperture of diameter a [19]. In other words this means that the pupil field distribution in Eq. (2.2.14) is simply a disk of diameter a .

This results to the intensity distribution of the diffraction pattern being:

$$I(x, y, z) \propto \left| \int_0^a J_0 \left(\frac{k_0 \rho' \rho}{2z} \right) e^{i\Phi(\rho')} \rho' d\rho' \right|^2, \quad (2.2.16)$$

where $\rho' = \sqrt{k_x^2 + k_y^2}$ is the radial position in the aperture, $\rho = \sqrt{x^2 + y^2}$ is the radial position in the resulting diffraction pattern, and J_0 is the Bessel function of the first kind of order 0. The function $\Phi(\rho')$ represents the wavefront aberration.

If the wavefront aberration is zero, the intensity I in Eq. (2.2.16) becomes proportional to a Sombbrero function:

$$I(\rho, z) \propto \left| \frac{J_1 \left(k_0 \frac{a}{2} \sin \theta \right)}{k_0 \frac{a}{2} \sin \theta} \right|^2, \quad (2.2.17)$$

where $\rho/z = \sin \theta$, and J_1 is the Bessel function of first order. The smallest width, d_{lim} , in the aperture that can be resolved in the observation plane is determined by the position of the first minimum of the intensity I . This smallest width is the diffraction limit, and is given by:

$$d_{\text{lim}} = \begin{cases} \frac{1.22}{\pi} \frac{\lambda_0}{n \sin \theta} & \text{Rayleigh criterion} \\ \frac{\lambda}{2n \sin \theta_0} & \text{Abbe resolution limit,} \end{cases} \quad (2.2.18)$$

with λ_0 is the vacuum wavelength and n is the refractive index of the medium. The numerical aperture is defined as $NA = n \sin \theta$.

2.2.4 Vector diffraction

A scalar diffraction theory is simple to derive but it does not fit the reality of most practical situations in optics. The polarization and vector diffraction can only be accessed by considering the vector nature of the electric field (see Fig. 2.7).

Richards and Wolf investigated the rigorous vector diffraction of the electric field [23, 24]. The diffraction pattern at a focal distance from the lens is calculated by considering a monochromatic point source of angular frequency ω placed at a distance infinity before the lens.

Starting from Eq. (2.2.7), Richards and Wolf firstly assumed that the system obeys the Kirchoff's boundary condition where any contribution from field outside the boundary conditions of the circular aperture is neglected [23]. This is valid as the diffraction of interest is in far-field as is the case of most microscopy techniques. However, the

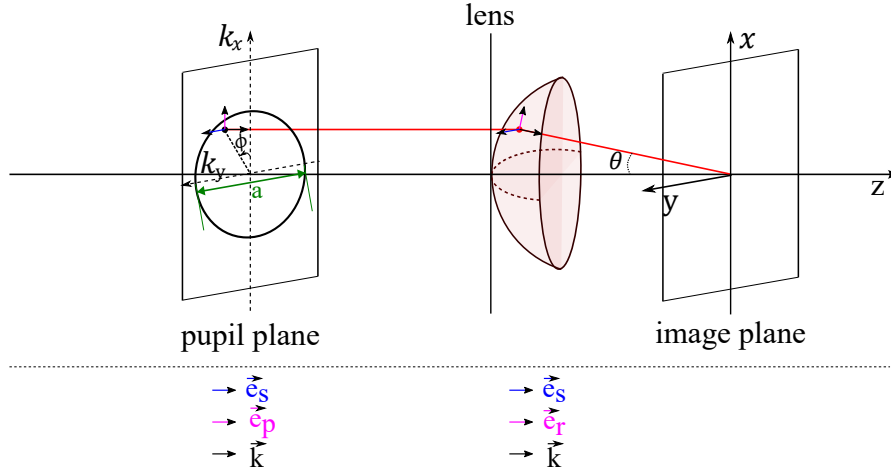


Figure 2.7: Vector field propagation from a circular aperture of diameter a through a high NA system. \vec{e}_s, \vec{e}_p are unit vectors of s and p -polarization state, \vec{e}_r represents the unit vector of the p -polarization after the projection on the Gaussian sphere.

representation of the electric field even in a vector formulation is still an approximation because the exact boundary condition of the imaging still remains unknown [23]. The second assumption adopts the principle of stationary phase. Sinusoids with rapidly varying phase are cancelled out. This implies an asymptotic approximation for large phase $\vec{k} \cdot \vec{r}$. Given those approximations, the expression of the electric field evaluated at a point $P(x, y, z)$, with spherical coordinates (r_P, θ_P, ϕ_P) , given in Eq. (2.2.14), is reformulated as follows:

$$\vec{E}(r) = -\frac{ik_0}{2\pi} \iint_{\Omega} \frac{\vec{a}(k_x, k_y)}{k_z} e^{ik_0[\Phi(k_x, k_y) + \vec{k} \cdot \vec{r}]} dk_x dk_y, \quad (2.2.19)$$

with θ_P being the elevation angle and ϕ_P being the azimuthal angle, \vec{a} is the strength factor and Φ is the aberration function describing the wave deformation in the pupil plane. Eq (2.2.19) is derived from the Helmholtz wave equation for a linear, isotropic, homogeneous and dispersive media and satisfies Maxwell's equations.

The components of \vec{E} are found as:

$$E_x(P) = -iC(I_0 + I_2 \cos(2\phi_P)) \quad (2.2.20)$$

$$E_y(P) = -iCI_2 \sin(2\phi_P) \quad (2.2.21)$$

$$E_z(P) = -2CI_1 \cos \phi_P, \quad (2.2.22)$$

where $C = \frac{\pi f l_0}{\lambda_0}$ is a constant, with f being the focal length of the lens in vacuum, l_0 an amplitude factor and λ_0 the wavelength in vacuum [23]. The three functions I_0, I_1 and I_2 are respectively defined for $q = 0, 1$ and 2 by:

$$I_q = \int_0^{\theta_{\max}} f(\theta) Q_q(\theta) J_q(kr_P \sin \theta \sin \theta_P) e^{ikr_P \cos \theta \cos \theta_P} d\theta, \quad (2.2.23)$$

such that θ_{\max} is the maximum angular aperture of the optical system, J_q is the Bessel function of the first kind and order q , and f is an apodization function. This function

is introduced to ensure the energy conservaton in the system. The general expression of the apodization is given in [49] by:

$$f(\theta) = \left[\frac{g(\theta)g'(\theta)}{\sin \theta} \right] \text{ with } g'(\theta) = \frac{dg(\theta)}{d\theta} \text{ being the first derivative of } g. \quad (2.2.24)$$

As seen in the previous Section 2.1.2, the imaging condition, supposedly a condition which connects rays in the object space with rays in the image space, is $g(\theta) = \sin \theta$ yielding to the apodization function $f(\theta) = \sqrt{\cos \theta}$ for a system obeying the Abbe sine condition. On the other hand, the expression of Q_q in Eq. (2.2.23) is defined as:

$$Q_q(\theta) = \begin{cases} \sin \theta(1 + \cos \theta) & \text{if } q = 0, \\ \sin^2 \theta & \text{if } q = 1 \\ \sin \theta(1 - \cos \theta) & \text{if } q = 2. \end{cases} \quad (2.2.25)$$

The expression of the electric field described until now corresponds to a system which does not account for any interfaces that may be present in the system. In many experimental situations, the system is formed by at least three media with two interfaces: sample, coverslip and immersion medium. The sample can be a stratified medium. Török et al. investigated the diffraction of light as it passes through different media of different indices of refraction. The interfaces are planar and perpendicular to the optical axis [25]. The integral representation of the field at the N^{th} medium is generalised for a stratified medium and is given by:

$$I_q^N = \int_0^{\theta_{\max}} f(\theta_1) Q_q^N(\theta_1) J_q(k_1 r_P \sin \theta_1 \sin \theta_P) e^{ik_N r_P \cos \theta_2 \cos \theta_P} d\theta_1, \quad (2.2.26)$$

with

$$Q_q^N(\theta_1) = \begin{cases} \sin \theta_1 \left(T_s^{(N-1)} + T_p^{(N-1)} \cos \theta_N \right) & \text{if } q = 0, \\ T_p^{(N-1)} \sin \theta_1 \sin \theta_N & \text{if } q = 1 \\ \sin \theta_1 \left(T_s^{(N-1)} - T_p^{(N-1)} \cos \theta_N \right) & \text{if } q = 2. \end{cases} \quad (2.2.27)$$

$T_s^{(N-1)}$ and $T_p^{(N-1)}$ are the transmission coefficients through the $(N - 1)$ interfaces at the very last interface, which correspond to the s and p polarization of the electric field. The refracted angles $\theta_1, \theta_2, \dots, \theta_N$ are linked by the Snell's law of refraction. The light is propagating from medium with subscript 1 to medium N in this formulation. The expression of T_p^{N-1} and T_s^{N-1} are given in Section 2.2.4.1.

2.2.4.1 Transmission coefficients

The complex valued transmission coefficient for a system with N homogeneous dielectric media *i.e.* with $(N - 1)$ -interfaces was derived by Török and Varga [27] based

on the previous work of Born and Wolf [20] and is given by

$$T_m^{(N-1)} = \frac{t_m^{(N-1)} \prod_{j=1}^{N-2} t_m^{(j)} \exp(i\sigma_{j+1})}{1 + R_m^{(N-1)}}, \quad (2.2.28)$$

where $R_m^{(N-1)}$ is a recursive function of the transmission $t_m^{(j)}$ and reflection coefficients $r_m^{(j)}$ at each interface (j) , $(j) \in [1, N-1]$. The function $R_m^{(N-1)}$ has a phase term and is equal to $r_m^{(1)} r_m^{(2)} \exp(2i\sigma_2)$ for $N = 3$ and $\sigma_j = k_0 n_j t_j \cos(\theta_j)$, n_j being the refractive index in medium j , t_j the thickness of the j -th medium and θ_j the refracted angle at $(j-1)$ -th interface and incident at (j) -th interface. The subscript m indicates p or s polarization. The Fresnel amplitude transmission, $t_m^{(j)}$, and reflection coefficients, $r_m^{(j)}$, are expressed as follows:

$$t_m^{(j)} = \frac{2ap_m^j}{p_m^j + p_m^{j+1}} \text{ with } a = \begin{cases} 1 & \text{if } m = s \\ n_j/n_{j+1} & \text{if } m = p \end{cases} \quad \text{and} \quad r_m^{(j)} = \frac{p_m^j - p_m^{j+1}}{p_m^j + p_m^{j+1}}, \quad (2.2.29)$$

with $p_s^j = n_j \cos(\theta_j)$ and $p_p^j = \frac{1}{n_j} \cos(\theta_j)$, $j \in [1, N]$ and $(j) \in [1, N-1]$ [20].

Given the expression of σ_j and the same assumption as by Török and Varga [27] and Haeblerlé [41] in the reflection coefficients being much smaller than unity, the denominator of Eq. (2.2.28) is rounded to unity and Eq. (2.2.28) can be rewritten as:

$$T_m^{(N-1)} \approx \left(\prod_{j=1}^{N-1} t_m^{(j)} \right) \exp(ik_0\psi) \quad \text{with} \quad \psi = \sum_{j=2}^{N-1} n_j t_j \cos(\theta_j). \quad (2.2.30)$$

Eq. (2.2.30) is approximately true for a corrected objective lens where the light transmission is enhanced hence low reflection [52]. The phase term ψ is compensated in the lens system in many of the recent microscope objectives [52]. The phase difference between the phase compensated by the lens system and the phase acquired in real imaging represents the phase aberration of the system contained in Φ in Eq. (2.2.19).

2.2.4.2 Polarization

The three spatial components (E_x, E_y, E_z) of the diffraction field in Eq. (2.2.20), (2.2.21) and, (2.2.22) are derived from a linearly polarized incident light oscillating along the x -axis as it propagates [23, 24]. For an arbitrary polarization of the incident light, the electric field in the observation plane can be expressed as a combination of those three components (E_x, E_y, E_z) . For a linearly polarized light making an angle α about the x -axis, the components of the resulting field in the observation plane \vec{E}_α is:

$$\vec{E}_\alpha = \begin{pmatrix} \cos \alpha & \sin \alpha & 0 \\ -\sin \alpha & \cos \alpha & 0 \\ 0 & 0 & 1 \end{pmatrix} \begin{pmatrix} E_x \\ E_y \\ E_z \end{pmatrix}. \quad (2.2.31)$$

The same principle can be applied for different polarization states. For instance, propagating a circularly polarized incident light is similar to propagating separately the components of the field and combining each propagated component of the fields in a vector summation. This is true given the fact that Maxwell's equations are linear and the superposition principle holds.

2.3 Diffraction theory of aberration

In the presence of an aberration, the wavefront at the exit pupil departs from the ideal Gaussian reference sphere. Some waves are delayed compared to others. Hence the formulation of the diffraction is modified accordingly.

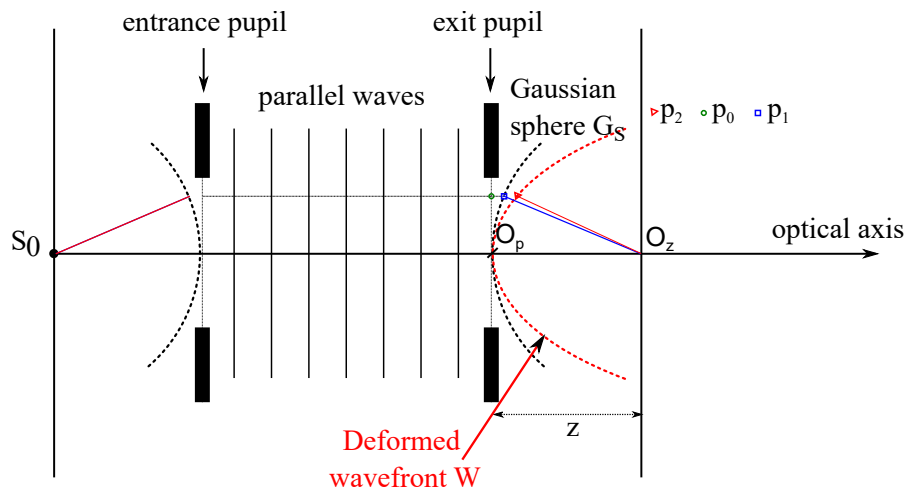


Figure 2.8: Geometry of wave aberrations. The blue line indicates the path travels by the wave in a non-aberrant imaging and the red line indicates the optical path in a non design condition aberrant system.

In Fig. 2.8, we illustrate an imaging of a plane to a plane of a single emitter S_0 in a $4f$ -system. A parallel wave arrives at a position p_0 at the exit plan. In a perfect imaging, this incoming wave is projected from p_0 to p_1 without acquiring any extra phase before it focuses at the focal point O_z on the observation plane at a distance z from the exit pupil (blue line). In an aberrant system, the ray acquire extra phase to reach to the point p_2 on the deformed wavefront before it focuses at O_z (red line). This phase, denoted by Φ , is defined as the OPD between the deformed wavefront denoted by W and the Gaussian reference sphere G_S in Fig. 2.8 and is given by:

$$\Phi(r, \rho, \phi) = [S_0 p_2] - [S_0 p_1], \quad (2.3.1)$$

with r being the object field coordinate, ρ the radial position at the pupil plane limited by the maximum angular aperture, and ϕ the azimuthal angle [53]. Under the Abbe sine condition, Φ depends on three rotationally invariant parameters $r^2, \rho^2, r\rho \cos \phi$.

A single aberration can be obtained by combining a power series of those three parameters. The primary transverse aberrations are obtained by differentiating the wave aberration Φ about the pupil radial coordinates. These derivations have been discussed in several textbooks and are not discussed any further in this thesis [20, 53, 54, 55].

In geometrical optics, only a single aberration, defined by the following general expression, might be detected:

$$b_{lnm} r^{2l+m} \rho^n \cos(m\phi), \quad (2.3.2)$$

with b_{lnm} being the aberration coefficient, $l, n, m \in \mathbb{N}^3$ such that $n > m$ and $n - m$ is even [53]. The parameters n and m define the radial and azimuthal orders of the wavefronts respectively. The parameter l defines the order of the aberration.

In diffraction theory, several single aberrations with given amplitudes, which can be negative or positive, add up to form a small phase change in the wavefront [55]. The linear representation of a set of single aberrations can be expressed in terms of the Zernike polynomials [56]. The distortion caused in the pupil plane mathematically corresponds to an additional phase in the complex amplitude electric field. This phase change influences how the light will interfere in the observation plane and so the diffraction pattern and the PSF.

2.4 Fourier imaging

As seen earlier in Fig. 1.2 of Section 1, the formation of an image by a given optical system can mathematically be described as a convolution of spatial fluorescence intensity distribution, for instance created by a spatially varying fluorophore concentration, with the PSF of the system. The PSF is derived from the rigorous vector diffraction of light transmitted by a circular aperture. The PSF is mathematically the intensity distribution which results from the square of the electric diffraction field.

The spatial intensity distribution of the object, denoted by O , can be interpreted as the probability density of the light emitted from the object (the fluorophore) after photo-excitation. We denote \vec{h}_{amp} the complex amplitude spread function (ASF) and $h = |\vec{h}_{amp}|^2$ without the subscript the corresponding intensity PSF.

2.4.1 Coherent imaging

In a coherent or partially coherent system, the electric fields from different point source emitters can be in phase or out of phase. The phase coherent term is not zero. The resulting image amplitude \vec{A}_I is obtained as a convolution of the object field amplitude, \vec{A}_O , with the ASF:

$$\vec{A}_I(r) = \vec{A}_O(r) \otimes \vec{h}_{amp}(r). \quad (2.4.1)$$

The image intensity is given by $I(r) = \vec{A}_I(r) \cdot \vec{A}_I^*(r)$, being the scalar product of \vec{A}_I with its complex conjugate \vec{A}_I^* and r being the image spatial coordinate.

2.4.2 Incoherent imaging

In an incoherent imaging system, the phase between the electric fields of point emitters fluctuate randomly and the pairing of the phase cannot be detected by the camera due to the limited bandwidth of the detector [1]. The sources are independent and uncorrelated. The time-average intensity of the superposition of the fields is phase independent. Thus, the convolution operation in the imaging applies for the intensity. This is usually the case of fluorescence microscopy. Since fluorescence light emission is a spectrum instead of being monochromatic, the PSF at each frequency adds to the total intensity. The ideal detected image intensity is thus given by:

$$I(r) = O(r) \otimes h(r), \quad (2.4.2)$$

The object intensity and the PSF coexist without affecting each other. In integration formulation, this convolution process is represented as follows:

$$I(r) = \iint_{-\infty}^{+\infty} O(r')h(r - r')dr', \quad (2.4.3)$$

with r being the image coordinates and r' is the object coordinates.

2.5 Image reconstruction: deconvolution

The knowledge of the PSF can be used for many things such as a prediction model or for characterization of a given optical system [57] and especially for image reconstruction [35]. Image reconstruction, also called deconvolution, is of importance in retrieving the best estimate of an object from a diffracted measured data given the measured noisy image of the object. In other words, it consists of undoing the convolution of the object by the PSF during the imaging by minimizing a pre-defined cost function. Deconvolution is an ill-posed problem [58]. The OTF is band-limited as the system is diffraction-limited. It generally does not have an inverse and may lead to an unstable solution in presence of noise [59]. Higher frequencies in the object will be cut-off and lost during the imaging process. Important information in the object along the axial frequency is removed and not contained in the recorded widefield images due to the missing cone in the OTF. Retrieving the object from the measured image may not give a solution or lead to non-unique results. A set of additional assumptions and parameters has to be adopted to avoid this indifference and recover the object. This includes prior knowledge about the object to recover such as non-negativity constraint and noise distribution [35, 60].

Deconvolution is characterized by the loss or cost function which is to be minimized, the minimization algorithm itself, the prior knowledge about the object to retrieve and the associated noise model that is predicted to be contained in the measured data. The choice of the regularizer is pivotal for the best restoration and it can speed up convergence of the restoration [60]. Some deconvolution techniques and algorithms assume a Gaussian distribution of noise while others assume the Poisson distribution or a mixture of Gaussian and Poisson noise. If the noise level is significant, a Poisson noise model can be approximated by Gaussian distribution. A trade-off between the number of iterations and the quality of the reconstruction must also be considered carefully as higher number of iterations may lead to noise amplification [35, 60, 61]. The cost function is given as follows:

$$C(I, O) = L(I, O) + \gamma P(O), \quad (2.5.1)$$

with I being the noisy measured image, O the object to estimate, L the negative likelihood function, P the penalty or regularizer function which contains prior knowledge of the object and γ the regularization parameter which determines the strength of the regularization. Maximizing the probability of obtaining the best estimate of O , given I , is equivalent to minimizing the negative log likelihood function in addition to the penalty function (the regularization). The data term $L(I, O)$ is given by the following equations for a Gaussian and Poisson noise respectively:

$$L_G(I, O) = \|h \otimes O + b - I\|^2 \quad \text{Gaussian noise} \quad (2.5.2)$$

$$L_P(I, O) = \sum h \otimes O - I \log(h \otimes O + b) \quad \text{Poisson noise,} \quad (2.5.3)$$

with h being the PSF, b the background light.

The penalty function with a Gaussian, entropy and Good's roughness prior are given as follows respectively [35, 60, 62]:

$$P_G(O) = \sum \|O\|^2 \quad \text{Gaussian prior,} \quad (2.5.4)$$

$$P_E(O) = \sum O \log(O/m) - \sum O + \sum m \quad \text{Entropy prior,} \quad (2.5.5)$$

$$P_R(O) = \sum \frac{|\nabla O|^2}{O} \quad \text{Good's roughness,} \quad (2.5.6)$$

with m being an unknown parameter which assumes a knowledge of the shape of the object. The operations in the two equations above are point-wise. Solving the minimization problem using the cost function may or may not necessarily lead to an analytical solution. Some techniques solve this problem in an iterative way instead of using the analytical solution. An accurate PSF is required for a successful deconvolution. If the PSF is unknown, the deconvolution is done blindly by estimating the object and the PSF in parallel [63] or estimating the PSF blindly and proceeding to the standard deconvolution using the estimated PSF afterwards. In this case, the recovery process is becoming more complex and is called blind deconvolution.

The next chapter focuses on presenting efficient methods for calculating a realistic and accurate PSF model.

Chapter 3

Point Spread Function Calculations

Practical approaches for calculating realistic PSFs for wide-field microscopy are still lacking in the field and constitute the focus of this chapter. The models are extended to account for a possible tilt of a plane which is a common alignment issue or due to the sample property. Furthermore, the computation of a dipole emission PSF and the consideration of the space-variance property of an imaging in the PSF calculation are discussed. We conclude this chapter by describing the limitation of wide-field imaging.

3.1 Introduction

The electric field's amplitude derived from this study satisfies Maxwell's equations and is limited to propagating far-field waves. *Four methods are discussed:* slice-propagation method using fast Fourier transform (SP-FFT) and chirp-Z transform (SP-CZT), Fourier shell interpolation method (F-Shell) and Sinc-R method (Sinc-R). These methods share as a starting point in the PSF calculation the computation of the three-dimensional (3D) Fourier spectrum on the pupil plane, a segment of the k -sphere called Mc-Cutchen pupil, which constitute the focus of Section 3.2 and 3.3. The four methods differ in the ways they propagate the field in free space. In the first two methods, SP-FFT and SP-CZT, the wave propagation are based on the angular spectrum methods. Although the original ideas of these two methods are not new and have been discussed widely in the literature especially the SP-FFT, here we present *a practical approach taking into account the pitfalls of the mathematical operators* (FFT and CZT) used in the models and the ways around them that we believe have not been discussed elsewhere in the literature to the best of our knowledge. These studies are in the goal of achieving an accurate and efficient calculation. The F-Shell method uses the iterative Fourier transformation algorithm to interpolate the necessary Fourier space kernel forming the field propagator. The last method Sinc-R or sinc-shell is based on the knowledge that the 3D Fourier transform of a complete spherical shell has a sinc function solution in real space. The half of the 3D spherical shell is used to represent

the field propagator in free space. These two last methods are totally new from the idea conception to the implementation to the best of our knowledge.

A more realistic PSF model accounts for the vector features of light and the experimental parameters. A tilt of one or many planes about the axis normal to the optical axis is one those experimental parameters that is most probable to be present during an image acquisition alongside of the refractive index mismatch in the sample and immersion medium. The deformation in the McCutchen pupil and induced phase aberration due to this tilting are discussed in details in this chapter. The particular case of a tilted coverslip is considered. To the best of our knowledge, *the approach of using the tilted McCutchen pupil combined with the very first analytical expression of the phase aberration from a tilted plane such as a coverslip through a stratified medium and the linear decomposition of this phase into Zernike polynomials are new to the literature.*

The above-mentioned consideration is for calculating the PSF of a wide-field microscope from an isotropic emitter. We also present in this chapter the derivation of the emission dipole PSF. These calculations are based on the assumption of a shift-invariant system. In reality, the system may be shift-variant, for instance the case when the sample refractive index is heterogeneous. As a response to this, we discuss the shift-variance possibility of the PSF and conclude the chapter with a description of the optical limitation of a wide-field imaging.

The MATLAB programming language is used for writing the codes. The calculation generating the figures displayed in this thesis was done with MATLAB2018a on Windows 10 64-bit, Intel Core i5-6200U CPU @ 2.30GHz, 8,0GB RAM, Intel HD Graphics 520. *A MATLAB PSF toolbox is therefore an output from this study.* The code can be reproduced in any other programming languages such as Python.

3.2 The k -sphere

In Fourier space, each ray of a given wavevector \vec{k}_W corresponds to a point on a sphere of radius k_0 (see Fig. 3.1b). The medium in the image space is usually air while the medium in which the wave is propagating in the object space is the immersion medium of the objective lens. The sphere is called the Ewald sphere or k -sphere (see Fig. 3.1). Due to the limiting factor in the numerical aperture of the objective lens, only a portion of the emitted light from the emitter is collected and transmitted by the optical system. In a system with a stratified medium of N number of layers where each layer in the object plane (sample, coverslip and immersion medium) has different refractive index, the effective numerical aperture, NA_{eff} , is the minimum between the designed NA and the different refractive indices in the stratified medium *i.e.* $NA_{\text{eff}} = \min\{NA, n_j; j = 1, \dots, N\}$, n_j being the refractive index of the j^{th} layer. This effective NA enables the block of any evanescent wave due to total internal reflection to contribute to the final field. The 3D frequency spectrum in Fourier space

is therefore only non-zero in a segment of the Ewald sphere delimited by this effective NA . This segment is called McCutchen pupil or generalized aperture (thick solid line in Fig. 3.1).

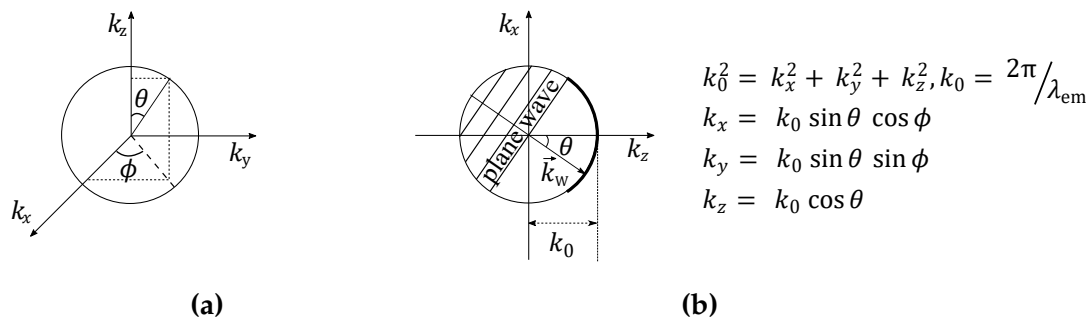


Figure 3.1: (a) Coordinate system in Fourier space: θ and ϕ are the elevation and azimuthal angles respectively. (b) Fourier space representation of a plane wave from a wavelet W at a point source P_W in the pupil plane called McCutchen pupil (thick cap). The k_y -axis in (b) is oriented towards the front plane of the paper.

3.3 The electric field on the k -sphere

To derive the 3D spectrum on the McCutchen pupil, let us firstly limit ourselves to a scalar electric field before we consider the vector nature of the electric field.

The end goal is to calculate the focal field intensity of an objective focusing a spherical wave to a low NA tube lens (see Fig. 3.2). The beam is entering the objective system from the left side and is spatially limited by the entrance pupil of the optical system, which represents the image of the aperture stop as created by the optics to the right of the aperture in Fig. 3.2. Such a limit, “aperture stop”, is in practice either intentionally introduced or effectively provided by the inner geometry of the objective, to warrant the linear shift invariance performance of the system. It is also used to avoid unwanted beams, which would introduce aberrations if propagating through the system. At the aperture stop, every point, P_W , on the wavefront is considered as a source of a spherical Huygens wavelet [64].

Each of the wavelet denoted by W in Fig. 3.2 gives rise to a plane wave after the tube lens. The plane waves are directed towards the nominal focus denoted by S , belonging to the image plane. Due to the Abbe sine condition and the notion of Gaussian reference sphere, the wavelets have to acquire exactly the same optical path and interfere constructively at this nominal focus S . The plane waves superimpose to form the spherical wave converging at S . This superposition is derived from Huygens-Fresnel principle [64].

The pupil plane aperture stop gives rise to a 3D cap residing on the k -sphere in Fourier space. A pupil position in real space exactly corresponds to the lateral component (k_x, k_y) of the wave-vector \vec{k} (see Fig. 3.2). The Fourier spectrum, which

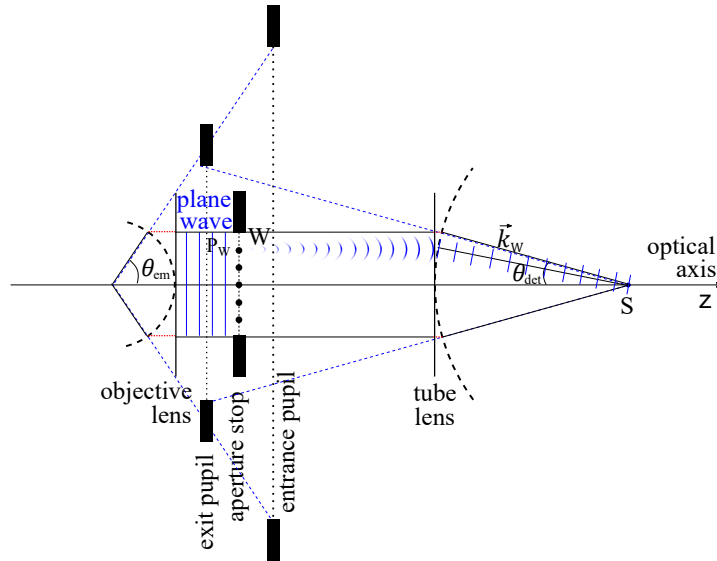


Figure 3.2: A monochromatic coherent plane wave formed by a high NA microscope objective in the pupil plane is a source of Huygens wavelet which becomes a plane wave when focused by a lens at a point S in the image plane.

corresponds to the field in the object as well as the image plane are illustrated in Fig. 3.3.

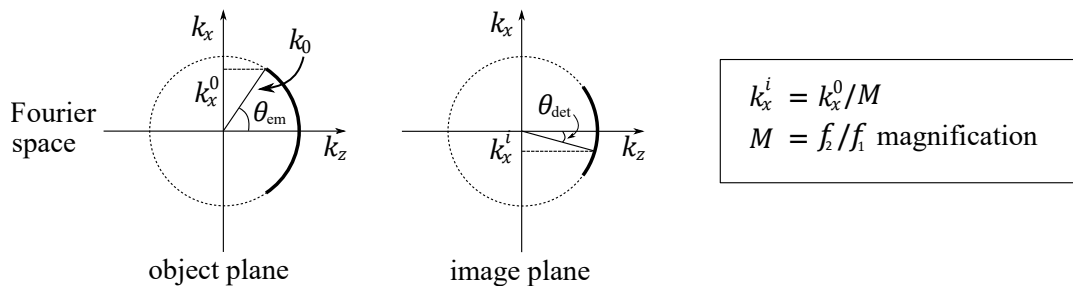


Figure 3.3: Representation of the waves on the k -sphere in the object plane (left) and in the image plane (right). The bold solid line represents the McCutchen pupil.

The above-mentioned formulation is for wave propagation from an emitter placed at the focal length before the objective lens, a point-like emitter in focus. We assume a perfect anti-reflection coated objective lens and all the energy is transmitted for such a ray. As the tube lens is assumed to be with a low NA, its can be approximated as a digital Fourier transform operation (FFT) in our calculation. The field obtained from the FFT of the field on the k -sphere represents the field in the image plane. To calculate the electric field on the k -sphere, let $\vec{E}_i = (E_x, E_y)$ be the transverse electric field incident at the pupil plane. The field is polarized along the direction given by the spatial components of \vec{E}_i . The components of \vec{E}_i are given in the coordinate system of the 2D pupil of Fig. 3.4b. The field of the plane waves on the McCutchen pupil is a 3D-projection $\vec{E}_k = (E_x, E_y, E_z)$ of \vec{E}_i . The directional change of the electric field is illustrated in Fig. 3.4. The coordinate (x, y, z) is the spatial position at which the

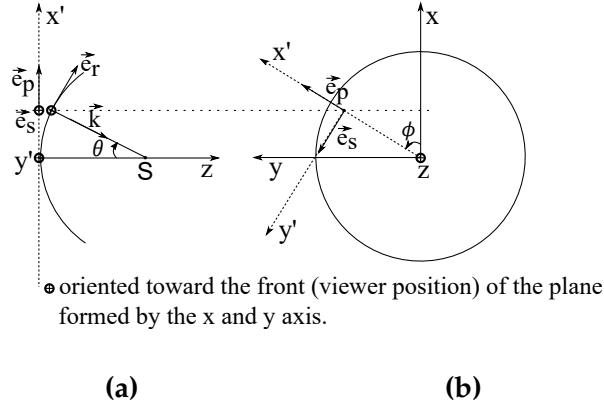


Figure 3.4: Schematic diagram of the coordinate systems for the directional change of a wave field E_i through an objective lens. (a) Adaptive coordinates on the McCutchen pupil. (b) 2D pupil plane.

field is evaluated. It is however useful to consider a locally varying coordinate system along azimuthal (\vec{e}_s) and radial (\vec{e}_p) directions respectively to facilitate the calculation. The subscript p and s represent the polarization state of the vector quantity with p and s stand for parallel and perpendicular (derived from the German word “senkrecht”) to the plane of incidence.

The wave propagation is directed by the wave vector \vec{k} (see Fig. 3.4a). The system is assumed to fulfil the Abbe's sine condition, requiring the beams to change direction at the Gaussian reference sphere. This changes the direction of the unit vector corresponding to the radial component \vec{e}_p refracted by θ to become \vec{e}_r . The azimuthal component oriented along \vec{e}_s however remains the same. The new coordinate system is illustrated in Fig. 3.4 and the coordinates of the three above-mentioned unit vectors are given by:

$$\vec{e}_s = \begin{pmatrix} -\sin \phi \\ \cos \phi \\ 0 \end{pmatrix}, \quad \vec{e}_p = \begin{pmatrix} \cos \phi \\ \sin \phi \\ 0 \end{pmatrix} \Rightarrow \vec{e}_r = \begin{pmatrix} \cos \phi \cos \theta \\ \sin \phi \cos \theta \\ \sin \theta \end{pmatrix} \quad (3.3.1)$$

The field amplitude distribution at a point (x, y, z) which forms one point at the spherical coordinate (k_0, θ, ϕ) of the McCutchen pupil is therefore given by:

$$\vec{E}_k(k_x, k_y, k_z) = (\vec{E}_i \cdot \vec{e}_p) \vec{e}_r + (\vec{E}_i \cdot \vec{e}_s) \vec{e}_s. \quad (3.3.2)$$

In N -layers of homogeneous dielectric stratified medium, the radial unit vector \vec{e}_p is rotated $(N - 1)$ times before it gets into the final unit vector \vec{e}_r in the N -th medium. Taking into consideration the Fresnel coefficients and transmittance due to the interfaces, the field amplitude distribution is generalized as:

$$\vec{E}_k(k_x, k_y, k_z) = T_p^{(N-1)} (\vec{E}_i \cdot \vec{e}_p) \vec{e}_{r_N} + T_s^{(N-1)} (\vec{E}_i \cdot \vec{e}_s) \vec{e}_s, \quad (3.3.3)$$

where $T_p^{(N-1)}$ and $T_s^{(N-1)}$ are the transmission coefficients for the N layers for p and s polarization respectively (see Section 2.2.4.1). The expression of the radial unit vector in the final medium near the Gaussian focusing point S is given by:

$$\vec{e}_{r_N} = \begin{pmatrix} \cos \phi \cos \theta_N \\ \sin \phi \cos \theta_N \\ \sin \theta_N \end{pmatrix}, \quad (3.3.4)$$

θ_N is the elevation angle of the wavevector in medium N . It is linked to the elevation angle in the other medium by the Snell's law.

According to McCutchen, the 3D diffraction pattern obtained by imaging a point source with a lens is the 3D-Fourier transform of the generalised aperture [65]. In other words, the complex amplitude of the diffraction pattern in the image plane can be derived from the 3D-Fourier transform of the McCutchen pupil. The methods for computing the PSF that we describe in this study are based on this finding of McCutchen. As the methods are therefore Fourier-based, it is important to firstly discuss the techniques that we adopt in the calculation in order to avoid the pitfalls that may arise from the mathematical operators such as the digital Fourier transformation before we discuss the techniques for computing the PSF from the knowledge of the McCutchen pupil.

3.4 Digital Fourier transformation and its pitfalls

The digital Fourier-transformation, fast Fourier transform (FFT), is a very handy tool to speed up PSF calculations, but its pitfalls must be avoided carefully.

3.4.1 Sampling condition

Experimentally speaking, the PSF is detected on a pixelated device, commonly CCD or CMOS Camera. During the acquisition of the image, the signal is integrated in each of the pixels of the detectors with weight defined by a pixel sensitivity function. A numerical calculation of the PSF samples its continuous mathematical expression predicting values on a delta-shaped grid. The local integration of the PSF in every pixel by the detector can be described as a sampling on a regularly spaced grid of the convolved PSF with the pixel sensitivity function.

In Fourier space, this corresponds to a multiplication of the OTF with the transfer function of the camera which is given by:

$$T_C(k_x, k_y) = \text{sinc} \left(\pi k_x \frac{p_x}{2} \right) \text{sinc} \left(\pi k_y \frac{p_y}{2} \right), \quad (3.4.1)$$

where (p_x, p_y) are the pixels size along x and y -axis respectively. The transfer function of the camera is the Fourier transform of the pixel sensitivity function. Solving

Eq. (3.4.1), the function T_C is crossing zero if the spatial frequencies (k_x, k_y) are at double the current sampling frequency ($k_{x|samp} = 1/p_x, k_{y|samp} = 1/p_y$) respectively. It is also important to emphasize that a decrease in sensitivity of the camera may cause the PSF for perfect circular symmetry (e.g. using circular or random polarization) to lose its symmetry, especially along the diagonals.

3.4.2 Nyquist Shannon theorem

As mentioned earlier, the minimal resolvable spatial structure in lateral plane is given by Eq. (2.2.18). Taking the simplest case where the pixel pitch is a square of width $p_{x,y}$, the Abbe diffraction limit is given by $p_{x,y|min} = \lambda_{em}/(2NA)$. As seen from the zero-crossing of the pixel sensitivity function in the previous section, the maximal lateral frequency component is given by $k_{r|max} = 1/p_{x,y|min} = 2NA/\lambda_{em}$. According to the Nyquist Shannon theorem, the highest frequency has to be sampled with at least two positions per wavelength [66]. Spatial frequencies above this limit would come to be outside the digital Fourier-space representation and then aliased to a wrong place within it. To avoid aliasing, this implies that the pupil needs to fit into half the digital Fourier-space representation such that its autocorrelation (i.e. the incoherent OTF) fits in the digital Fourier space. The autocorrelation of the pupil corresponds to its absolute square. The maximal pupil radius in Fourier space along x or y should be lower than half the maximally represented frequency along k_x or k_y in our Fourier-space representation.

3.4.3 Fourier sampling pitfall

Working with discrete data requires care when dealing with the digital Fourier transform. A digital misrepresentation of the usually round pupil in Fourier space may induce a severe artefacts especially if the number of pixels inside the jagged representation of a disk is few. The discontinuity at the edge of the pupil with the pixel pitch being a square in most cases can cause a significant error in the calculation. To illustrate this effect, let us consider a field distribution imaged through a high- NA optical system with $NA = 1.4$ in a sample medium of refractive index equal to 1.518. The emission wavelength is assumed to be $\lambda_{em} = 580$ nm. The pupil radius which corresponds to the Nyquist theorem is $\lambda_{em}/(2NA)$. We denote by k_{max} the radial frequency coordinate at the edge of the pupil radius. To compare the effect of the pupil aperture on the field distribution, we compute two hard apertures H_1 and H_2 with window size 128×128 and 1024×1024 and radius $k_{max}/8$ respectively. The pixel size in real space is chosen to be 80 nm which yields to k_{max} being at about 25 and 198 pixels from the centre of the pupil for H_1 and H_2 respectively. The field distribution calculated from the digital fast Fourier transform of the pupil H_1 and H_2 are displayed in Fig. 3.5a and 3.5c respectively.

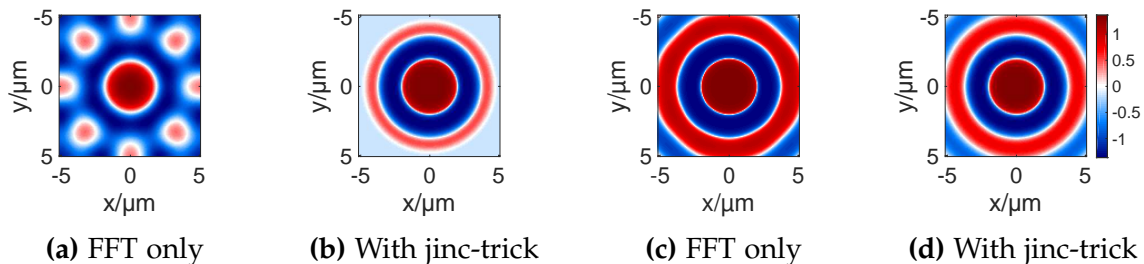


Figure 3.5: Illustration of the Fourier sampling pitfall. Field distribution calculated from the Fourier transform of (a) a hard aperture of size 128×128 pixels, (b) a jinc aperture aperture of size 128×128 pixels, (c) a hard aperture of size 1024×1024 pixels cropped to 128×128 pixels size for display and, (d) a jinc aperture aperture of size 1024×1024 pixels cropped to 128×128 pixels size for display. A DampEdge of 15% is applied to the generated field (full size) using the jinc-trick. Figures are displayed at $\tan^{-1}(\gamma E)$ and centered at the zero of the display, E being the field distribution and $\gamma = 20$.

For symmetry reasons, one would expect those two fields in Fig. 3.5a and 3.5c to be perfectly circular and symmetric. However, as seen in Fig. 3.5a, the field is not circular as it should be. With H_2 , the discrepancy in the field has significantly been reduced even though it still not perfectly round (see Fig. 3.5c). Computing the hard aperture H_2 is on average 5.6720 times slower than computing H_1 . The solution we propose to remedy this issue is based on the fact that the Fourier transform of a disk is given by a jinc function: $\text{jinc}(r) = J_1(k_r r) / (k_r r)$, J_1 being the Bessel function of the first kind, k_r and r the radial coordinate in Fourier and real space respectively. The “ideal” representation of a disk in Fourier domain is calculated using a digital fast Fourier transform (FFT) of a 2D jinc function. This “interpolated” disk can then be appropriately modified with k -space dependent phase and magnitude alterations. We call this method for computing a disk using a jinc function the “jinc-trick”. In Fig. 3.5b, we observe that at a smaller window size as 128×128 , the real space representation of the field distribution is perfectly circular and symmetric. The computation of a jinc aperture of window size 128×128 is only 1.496 times slower than the computation of an hard aperture with the same window size. This offers a high advantage in accuracy and computation time. One pitfall of this technique that we should care about is that the jinc-function possesses first order discontinuities in real space at the border. This causes unwanted high-frequencies in the Fourier-transformation [67]. To avoid this, the jinc-function is modified at the outer ends by appropriately smoothing the 15% of its edges. The smoother function is called “DampEdge” in our toolbox.

3.4.4 Fourier wrap-around

The digital Fourier transformation also has periodic boundaries. There is a maximum Δz range threshold under which the waves can still be inside the available lateral space provided by the real-space grid. Outside this region, *i.e.* at higher depth, the wave at higher lateral spatial frequency position will wrap-around and causes undesirable

standing waves [68]. This problem is called Fourier wrap-around (see Fig. 3.6a and 3.6d). This effect can cause inaccuracy in PSF calculation. We present here three ways that can help to avoid this effect.

Firstly, one can zero-pad the in-focus plane to provide space for the standing wave to occur outside of the region of interest. However, the time complexity of a 2D FFT operator is $O(M \times N \log(M \times N))$, where $M \times N$ is the size of the image [68]. Zero-padding the initial image window by a factor q slows the calculation of FFT by $q^2 \times M \times N \log(q^2)$. Under MATLAB, doubling the initial image window size takes on average 5 times longer than computing the FFT of the initial size. Zero-padding is computationally expensive yet it can still lead to non-desirable artifact for typical z range used in 3D PSF calculations.

Secondly, one can establish absorptive boundary conditions. In this regard, an ideal absorptive boundary condition is applied to the edge and the propagation is carried out by re-projecting the filtered field onto the pupil plane at every propagated slice [69]. This has the disadvantage of sacrificing a good PSF for a portion of pixels near the edge in the lateral surface xy sides of the calculation. In addition, every propagation requires two Fourier transformations, instead of only one.

The last alternative consists of using another mathematical transform, the chirped-Z transform (CZT) [70, 71]. With the help of CZT, we can increase the resolution in Fourier domain by zooming onto the pupil. The zooming factor is function of the required z -depth. Higher depth requires bigger zoom, but we limit the upper bound of the zooming factor based on the available grid size in x and y directions. This zooming process in the pupil plane serves two purposes: representing the pupil better and expanding the range in the Fourier-transformed field.

If the z -depth is however significantly large and the grid size in x and y are small, a zooming factor on the field in the pupil plane to be confined within the available space may not be sufficient to avoid the Fourier wrap-around. An extension of the grid may be necessary to confine all the necessary zoomed spectrum information in Fourier space. This is still advantageous compared to the zero-padding as only the necessary grid is calculated and used at each z -depth. If the window size is not changed but kept constant throughout the field propagation, wrap-around artefacts may still be present as we go from one space to another but the signal is more enhanced than a standard FFT due to the zooming factor, reducing the effect of the artefacts.

The choice between a CZT and a zero-padded FFT mainly depends on the working depth. On one hand, it is more practical to use CZT to calculate a volume field with higher depth as a highly zoomed sampled pupil can be enough to propagate the desired ranges while zero-padding can be costly in time and memory without assurance that the artefact will be avoided. On the other hand, a simple FFT can be sufficient to obtain a more accurate and faster computation of the field than the CZT method while avoiding the wrap-around if only the computation of the field near the

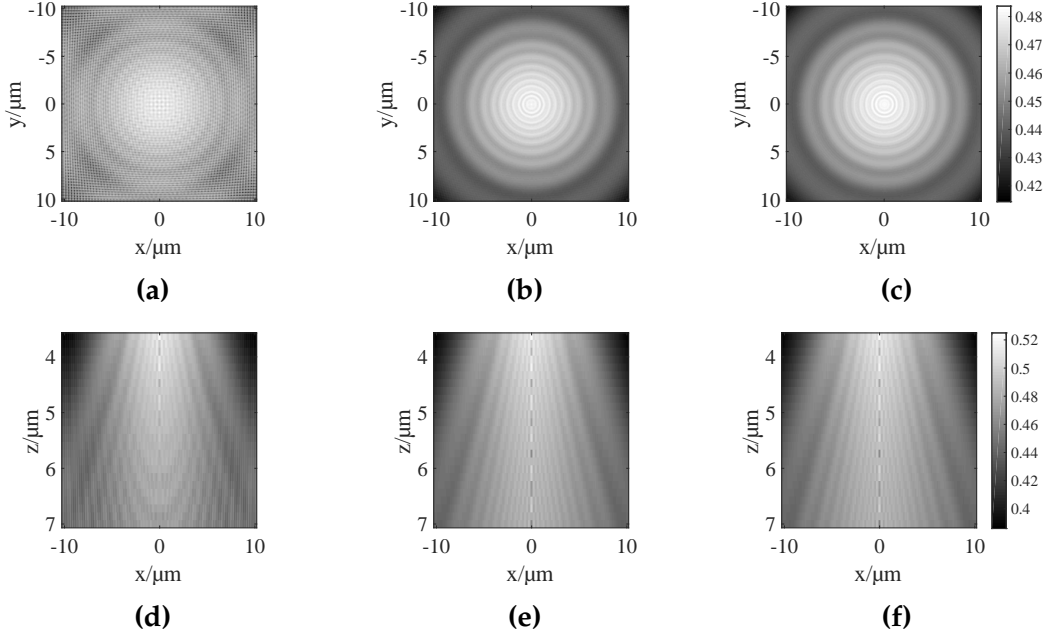


Figure 3.6: Wrap-around of using FFTs in PSF calculations. Profiles displayed at $\gamma = 0.05$ of the PSFs calculated from the slice propagation method. (a, b, c) xy -plane at defocus position $7\mu\text{m}$. (d, e, f) xz -cut parallel to the optical axis at $3.5\mu\text{m}$ away from the focus and with $\Delta z = 3.5\mu\text{m}$. (a, d) Using the standard FFT. (b, e) By zero-padding the image window size to twice. (c, f) Using CZT. The parameters are $NA = 1.4$, immersion medium : water ($n = 1.33$), polarization : circular; emission wavelength $\lambda_{\text{em}} = 580\text{ nm}$, voxel size $80\text{ nm} \times 80\text{ nm} \times 140\text{ nm}$ and, window size : $256 \times 256 \times 25$ pixel.

focal region is required and the working depth is not large.

3.4.5 Chirp-Z transform

For a 1D signal $X_n, n \in [0, N - 1] \cap \mathbb{N}$ with N being the number of points of the signal and \mathbb{N} the set of natural numbers, the \mathcal{Z} transform $\tilde{X}_z, z \in \mathbb{C}$ is given as follows:

$$\tilde{X}_{z_m} = \text{CZT}(X_n) = \sum_{n=0}^{N-1} X_n \mathcal{Z}_m^{-n}, \quad (3.4.2)$$

where $\mathcal{Z}_m = AW^{-m}, m \in \mathbb{N}$ is a spiral path in \mathcal{Z} -path with A being the starting point and $W = \exp(-i\Delta\Gamma)$ the ratio of two consecutive points with a given angular increment phase $\Delta\Gamma$. For $A = 1$ and $\Delta\Gamma = 2\pi m/N, \mathcal{Z}_m$ is computed over an unit circle and the CZT operation becomes a discrete FFT. To zoom the signal X_n in by a scalar factor $c, A = \exp(-i\pi/c)$ and $W = \exp(-i2\pi/Nc)$ [71]. Therefore, Eq. 3.4.2 can be expressed in terms of convolution as follows [44]:

$$\tilde{X}_{z_m} = W^{m^2/2} \text{FFT}^{-1} \left(\text{FFT} \left(X_n A^{-n} W^{n^2/2} \right) \cdot \text{FFT} \left(W^{n^2/2} \right) \right). \quad (3.4.3)$$

The inverse CZT of a signal \tilde{X}_{z_m} in a frequency-domain representation is defined as the complex conjugate of the CZT of the complex conjugate $\tilde{X}_{z_m}^*$ of \tilde{X}_{z_m} within some scaling factor for a CZT operating on a unit circle [70].

3.5 Methods for computing PSFs

Using the determined field on the McCutchen pupil, here we present the four methods that are mainly the output of this study, taking into account the techniques we discussed in the previous section for avoiding the pitfalls of the FFT operator in the calculation.

3.5.1 Angular spectrum method

The first two methods use the Fourier slice theorem to determine the field at a given arbitrary axial position z [72]. Using this theorem, a z -slice in real space corresponds to an integral of the amplitude over the axial spatial frequency k_z in Fourier space. The 3D McCutchen pupil is firstly multiplied by $e^{ik_z z}$ and the result is projected onto the $k_x k_y$ -plane to obtain the field at the axial position z .

Since the McCutchen pupil is infinitely thin and we have a transversal wave propagating along one direction, the z -axis, there is only a single value at each point in the pupil which contributes to the 2D Fourier transform integral. A $1/\cos\theta$ factor arises when projecting a thin shell to a plane. This establishes a direct correspondence between the pupil plane amplitude and the two-dimensional (2D) Fourier transformation of the xy -amplitude at the focus. The 3D Fourier transform of the 3D McCutchen pupil to obtain the amplitude electric field in the image plane is reduced to a 2D Fourier transform of the projected pupil. The factor $e^{ik_z z}$ is called propagator and the propagating process is an angular spectrum method.

In addition to the above-mentioned theory, the energy must also be conserved and considered in the PSF calculation to satisfy the imaging condition invariant (see Section 2.1.2). The aplanatic factor discussed in Section 2.1.3 needs to be taken into consideration in the calculation.

3.5.1.1 Slice propagation with FFT (SP-FFT)

We refer as “Slice Propagation” (SP) the angular spectrum method (ASM) for free space field propagation as the method consists of propagating the wave slice by slice. The method uses the acquired knowledge discussed earlier in Section 3.3. For a system with a stratified medium with refractive index mismatch, the effective NA described in Section 3.2 is considered in place of the nominal NA of the optical system. The steps to follow are described in Algorithm 1.

3.5.1.2 Slice propagation with CZT (SP-CZT)

Using the CZT in order to avoid or reduce wrap-around effect of FFT operation, we firstly need to calculate the zoom factor to apply on the pupil based on the desired depth. A zoom-in factor c is calculated such that the pupil fits perfectly near the edge

Algorithm 1 Slice propagation: SP-FFT**Input:** $NA_{\text{eff}}, \lambda_{\text{em}}, z, p_{x,y}$: lateral pixel pitch**Output:** [h : PSF intensity; \vec{h}_{amp} : complex amplitude field]

- 1: Define the 2D incident polarized transverse wave $\vec{E}_i = (E_x, E_y)$ at the pupil plane
- 2: With the knowledge of \vec{E}_i , compute the field $\vec{E}_k(k_x, k_y, k_z) \in \text{McCutchen pupil}$ using Eq. 3.3.3 with the jinc-FT trick as an aperture delimiter
- 3: Apply the factor $1/AF_{\text{amp}}$ for energy conservation and other phase modification:

$$\vec{E}'_k(k_x, k_y, k_z; \Phi) = 1/AF_{\text{amp}} \cdot \vec{E}_k(k_x, k_y, k_z) \cdot e^{i\Phi}$$
- 4: Calculate the propagator $e^{ik_z z}$
- 5: Propagate the field to the desired z -position (sum over k_z): $\vec{h}_{\text{amp}}(x, y, z) = \text{FFT}_{2D|xy}^{-1} \left(\vec{E}'_k(k_x, k_y, k_z; \Phi) \cdot e^{ik_z z} \right)$
- 6: Calculate the PSF intensity: $h = |\vec{h}_{\text{amp}}|^2$

of the lateral window size. If the PSF at a given z -depth requires a bigger window, a new window size N'_{xy} is firstly calculated and the zoom-in factor c is calculated using this new size. We therefore calculate the pupil with the new size N'_{xy} and the lateral pixel pitch which is c -times bigger than the given pitch. To calculate c , let us consider a plane wave originating at the centre of the real space in focus-plane. The maximum angle at which an oblique emission at this position will be propagating is given by the maximum angular aperture of the optical system. The lateral radius of this beam is therefore given by D (see Fig. 3.7). Given that the in-focus plane is calculated over N_{xy} pixels, the PSF requires at least $N'_{xy} = 2(N_{xy}/2 + D)$ window size to fit the PSF at a higher depth z without standing waves. The appropriate c factor is calculated as $c = (N_{xy}/2 + D)/(N_{xy}/2)$, where $\tan \theta_{\text{max}} = D/\Delta z$ in real space and $\tan \theta_{\text{max}} = k_{xy}/k_z$ in Fourier space.

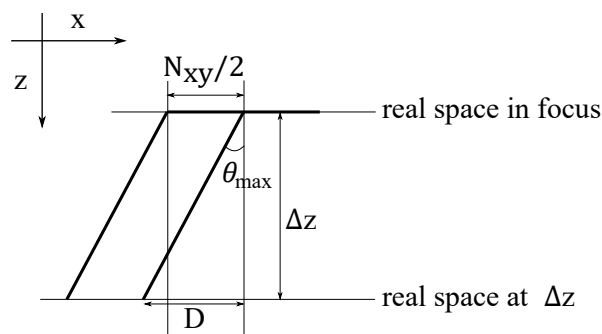


Figure 3.7: Diagram of the wave propagation in real space for calculating the zoom factor c .

The ASM is adapted and described in Algorithm 2 with the use of CZT.

3.5.2 Fourier-shell interpolation method (F-Shell)

This method aims at representing the useful part of the McCutchen pupil directly in 3D-Fourier-space and projecting the two-dimensional pupil functions onto this three-

Algorithm 2 Slice propagation: SP-CZT**Input:** $NA_{\text{eff}}, \lambda_{\text{em}}, z, N_{\text{xy}}, p_{x,y}$ **Output:** [h : PSF intensity; \vec{h}_{amp} : complex amplitude field]

- 1: Calculate the desired window size N'_{xy} and the zoom-in factor c
- 2: Define the 2D incident transverse wave \vec{E}_i at the pupil plane under the required window size N'_{xy} and pixel pitch $p'_{\text{xy}} = c \times p_{x,y}$
- 3: Compute the field $\vec{E}_k(k_x, k_y, k_z) \in \text{McCutchen pupil}$ using Eq. 3.3.3 with the jinc-FT trick as an aperture delimiter
- 4: Apply the factor $1/\text{AF}_{\text{amp}}$ for energy conservation and other phase modification:

$$\vec{E}'_k(k_x, k_y, k_z; \Phi) = 1/\text{AF}_{\text{amp}} \cdot \vec{E}_k(k_x, k_y, k_z) \cdot e^{i\Phi}$$
- 5: Calculate the CZT^{-1} of the result from Step 4 and zoom-out by the factor c from Step 1 to obtain $\vec{h}_{\text{amp}}(x, y, z) = \text{CZT}_{2\text{D}|_{\text{xy}}}^{-1} \left(\vec{E}'_k \right)$
- 6: Calculate the PSF intensity: $h = |\vec{h}_{\text{amp}}|^2$
- 7: Crop the needed h and \vec{h}_{amp} within the desired initial window size N_{xy}

dimensional shell. The difficulty is that the shell, at each integer $[k_x, k_y]$ position, has a non-integer k_z position which needs to be represented by interpolating along k_z in Fourier space.

As a credible representation of such a non-integer k_z would require essentially the full k_z -range for its interpolation, an appropriate compromise to keep the computation efficient is made. We aim to represent only the central part of the corresponding real-space representation as faithfully as possible and label a border region as “don't care” region (see Fig. 3.8b). This “don't care” region is limited by a chosen factor b_{reg} (here it is chosen to include 8 pixels from both edges). The part of real space in this border is iteratively updated, while the central part is forced to the expected values in each iteration in this iterative Fourier transformation algorithm (IFTA).

In addition, a pre-defined cut-off frequency $n_{k_{\text{cut-off}}}$ is chosen. This cut-off frequency limits the number of interpolation coefficients given by $n_z = 2n_{k_{\text{cut-off}}} + 1$, which can be used to fill the voxels along k_z in Fourier-space adjacent to the one nearest to the non-integer $k_z(k_x, k_y)$ position of the McCutchen pupil. The required interpolation coefficients are generated with the help of the IFTA [73]. We denote n_{subpix} the number of sub-pixel positions along k_z . As initialization, ideal $\exp(2\pi i k_z z)$ waves are generated in real space corresponding to the respective sub-pixel frequencies in Fourier space. The ideal waves are then Fourier-transformed and only n_z interpolator values are kept while all others are set to zero. The result is transformed back to real space, where the central area is replaced by the original perfect waves, but the “don't care” region is not touched. This is repeated over N iterations (typically 500 times) until convergence. The so-generated interpolation table of size $n_z \times n_{\text{subpix}}$ is stored for later use (see Fig. 3.8c).

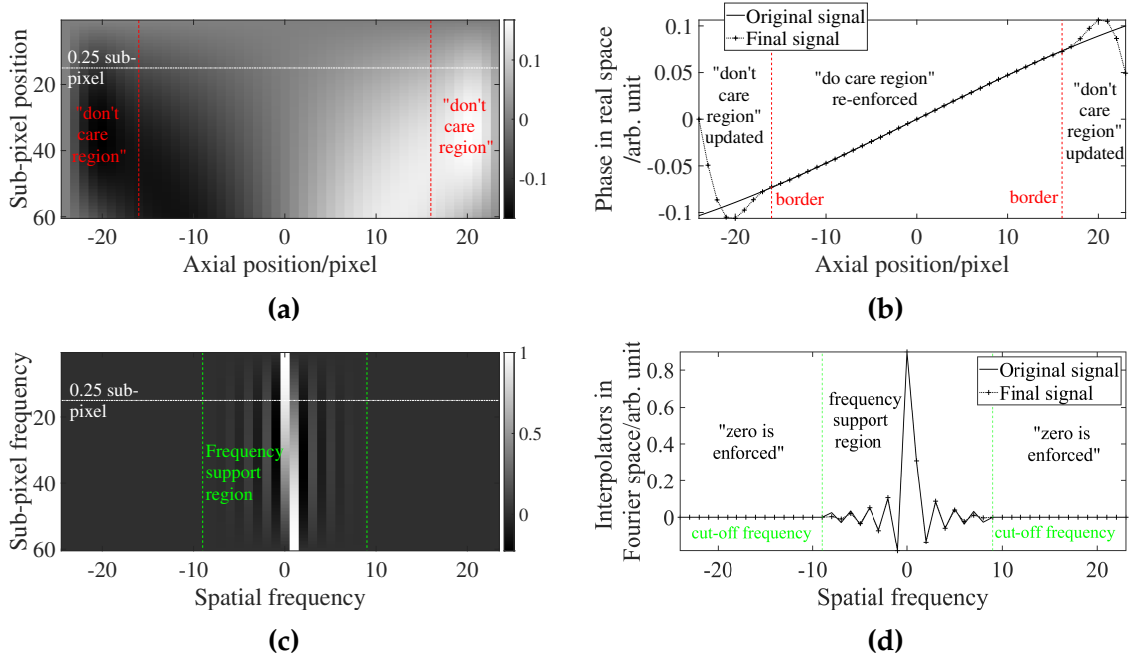


Figure 3.8: (a) Phase shift in the ideal wave $\exp(2\pi i k_z z)$. (b) Phase at a sub-pixel 0.25, indicated by the horizontal white line in (a). (c) Interpolation table in Fourier space containing the interpolator coefficients at 60 different sub-pixels. (d) Interpolation coefficients in Fourier space along the 0.25 sub-pixel indicated by the horizontal white line in (a) and (c).

In the example presented here, $n_{k_{\text{cut-off}}} = 8$ yielding $n_z = 17$ interpolation coefficients to be determined. An interpolation table of $n_{\text{subpix}} = 60$ sub-pixel positions of the 17 complex valued coefficients is pre-computed via IFTA. The inner part in the real space regime which represents the “do care region” is about 66% of the given z -range. A typical example for the offset of 0.25 pixels is shown in real and Fourier space in Fig. 3.8b and 3.8d respectively, overlaid with the ideal subpixel wave (solid line which corresponds to the legend ‘Original signal’). The border of the “don't care region” is indicated by the dashed vertical lines. A real space representation of the full interpolation table is shown in Fig. 3.8a with the “don't care region” also indicated by the vertical red dashed lines.

The size of the border factor b_{reg} (in pixels) and the cut-off frequency $n_{k_{\text{cut-off}}}$ defining the number of interpolation coefficients n_z should be roughly the same. If the “don't care region” is far bigger than the “do care region”, there tend to be fewer interpolation coefficients generated for the given region of support frequencies in Fourier space. Only few interpolation coefficients can be used. This yields to the integrated intensity of the PSF not uniform and increases the violation of missing cone which will be further discussed in Section 3.9. A small “don't care region” on the other hand can lead to inaccuracies inside the “do care region” hence the region of support frequencies in Fourier space. The principle of this PSF generation is summarized in Algorithm 3.

Algorithm 3 Fourier shell interpolation (F-Shell)**Input:** $NA_{\text{eff}}, \lambda_{\text{em}}, z, N_{\text{xy}}, p_{\text{xy}}, b_{\text{reg}}, n_{k_{\text{cut-off}}}, n_{\text{subpix}}, N$ **Output:** [h : PSF intensity; \vec{h}_{amp} : complex amplitude field]

- 1: Generate the McCutchen pupil projections as described in Algorithm 1 Step 1-2 using the jinc-FT trick as an aperture delimiter (see Section 3.4.3)
- 2: Apply the factor $1/AF_{\text{amp}}$ for energy conservation and other phase modification:

$$\vec{E}'_k(k_x, k_y, k_z; \Phi) = 1/AF_{\text{amp}} \cdot \vec{E}_k(k_x, k_y, k_z) \cdot e^{i\Phi}$$
- 3: Calculate $k_z(k_x, k_y)$ for every pixels within the pupil and round it to the nearest $1/n_{\text{subpix}}$ subpixel k_z position
- 4: Generate a 3D index of the full k -sphere
- 5: Write the field \vec{E}'_k calculated in Step 1 with the appropriate interpolation kernel for the sub-pixel at the 3D index position of the k -sphere
- 6: Store the interpolation coefficients for future use
- 7: Perform a three-dimensional Fourier transformation of the result from Step 5 to obtain the three-dimensional field distributions \vec{h}_{amp} (with expected errors in the “don't care region”)
- 8: Calculate the PSF intensity: $h = |\vec{h}_{\text{amp}}|^2$

This method can be performed fast and memory efficient as a single access operation in MATLAB by exploiting its indexed addressing capabilities. In this way, the complex-valued 2D pupil can be rapidly filled into the appropriate Fourier space region with the optimized interpolation coefficients as described above and the “don't care” region can be later removed. The required k_z -range can be kept to a minimum. This method was originally constructed to help with the reconstruction of coherent tomography data, where each entirely different phase projections (shells) can then directly added into Fourier-space without the need of any immediate propagation (e.g. by the slice propagation method) for each projection, which saves an enormous computational overhead.

3.5.3 Sinc-R method (Sinc-R)

This method is derived using the knowledge that the three-dimensional Fourier transform of a complete spherical shell is a $\text{sinc}(k_0|r|)$ function, r the spatial radial coordinate. To compute the k -sphere, we can determine the Fourier space which correspond to this function. Given this, the sinc-shell method is described as follows:

Algorithm 4 Sinc-R method

Input: $NA_{\text{eff}}, \lambda_{\text{em}}, r = (x, y, z), N_{xy}, p_{xy}$ **Output:** [h : PSF intensity; \vec{h}_{amp} : complex amplitude field]

- 1: Generating a $\text{sinc}(k_0|r|)$ amplitude distribution in three dimensions in real space
 - 2: Performing an appropriate DampEdge to the edge region of the image (e.g. 5% on each side of the image border) or extending the border of the desired window size by 25% in both direction x and y
 - 3: Fourier-transforming the distribution in Step 2
 - 4: Setting all values at negative k_z to zero (akin to a Hilbert-transform) or and/or keeping only the k_z -range which contains valid \vec{k} vectors (yielding a change in z -sampling and a phase ramp in real space, not affecting intensity values)
 - 5: Calculating the three components of the field in the McCutchen pupil using Eq. 3.3.3 using the jinc-FT trick as described in Section 3.4.3 and including the aplanatic factor for energy conservation
 - 6: Projecting the 3D spectrum of the propagating sinc wave calculated from Step 4, which correspond to a half of sinc-shell, onto the 3D McCutchen pupil in Step 5
 - 7: Compensating for the curvature of the sinc-shell by applying a factor $\cos \theta$, θ being the angular aperture that is previously defined
 - 8: Performing a three-dimensional Fourier-transformation for each of the field components to obtain the sought-after field components \vec{h}_{amp} in real space
 - 9: Calculate the PSF intensity: $h = |\vec{h}_{\text{amp}}|^2$
 - 10: In Step 2, **if** The border was extended by 25% instead of being damped at the edge **then** Extract the field within the desired window
-

This method has the attractive property that it does not suffer from the Fourier wrap-around effect since the field was directly generated in real-space. A disadvantage is each step has to be performed observing Nyquist sampling along k_z for the full field including its z -propagation. This method is also not readily applicable to a single slice (in or out-of-focus).

3.6 Aberrant PSF

In the previous algorithms, we have already considered the optical aberration that may be present in the system. The theory for computing the PSF that we have discussed so far is under the assumption that each interface and planes in the system are normal to the optical axis. In reality however, one plane might be inclined from the normal to the optical axis. A concrete example is an inclined coverslip. This often occurs when imaging biological sample especially with water-immersion objective lens [74]. In the particular case study described in this thesis, we assume that each medium's plane in a stratified medium is parallel to the inclined coverslip. The thickness of the immersion is not uniform at different lateral position. This inclination induces aberration and change in the diffraction pattern itself. In the next section, we will discuss the field on the k -sphere in the presence of a tilted plane such as an

inclined coverslip. The computation of the optical path difference, hence the phase aberration induced by refractive index mismatch and tilted coverslip, will follow the discussion. These results will be summarized in the algorithm for calculating an aberrant PSF with tilted coverslip. Moreover, we will show an example of the resulting fields in the pupil and the PSF intensity.

3.6.1 The k -sphere formulation in the presence of a tilted plane

As the Fourier transform operator is rotationally invariant [14], an elevation of one plane, which is assumed to be at the coverslip plane, by an angle α about one axis (e.g. x -axis) in real space rotates the McCutchen pupil by the same elevation angle about the reciprocal axis (e.g. k_x -axis) in Fourier space (see Fig. 3.9).

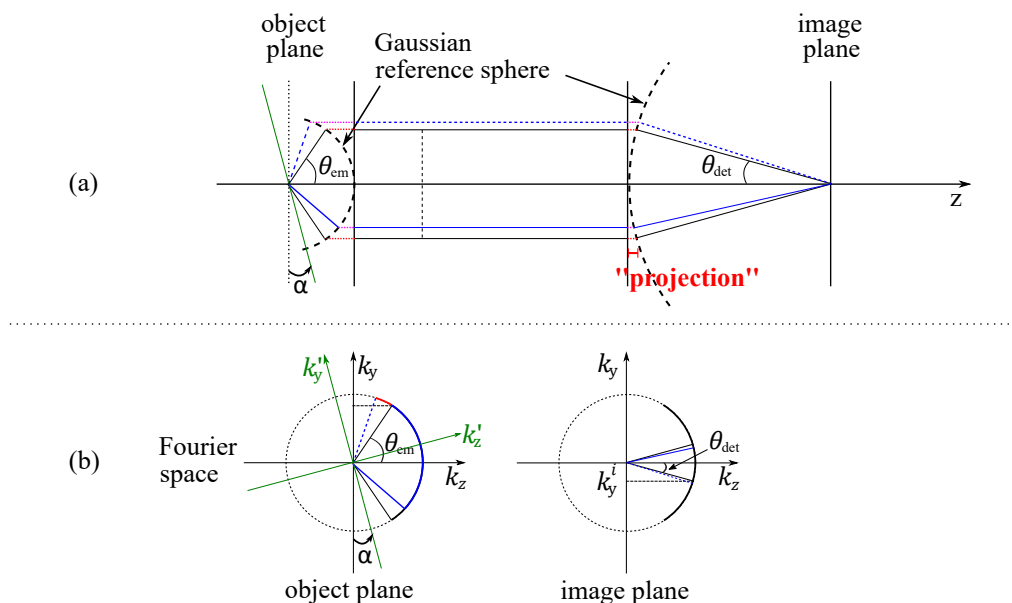


Figure 3.9: 4f-imaging with a tilted object plane in real (a) and Fourier space representation (b). Left: Emission path from the emitter in the object plane. Right: Detection path towards the image plane.

Due to the tilt in the coverslip, some information that is supposedly transmitted in a planar system (red cap in Fig. 3.9b of the McCutchen pupil which corresponds to the object plane) will not be collected by the optical system and some information that is usually not captured due to the limiting numerical aperture of the optical system will be recorded by the system (black cap). The field in the image plane corresponds to the superposition of the waves that are presented within the McCutchen pupil (blue and black cap). This is however only true if a refractive index mismatch is present in the system. In the case of an isotropic emitter and a non-aberrant system, this rotation does not change the information that is being recorded by the system as the signal is emitted uniformly in all directions from the point emitter. On one side (red cap) some sample spatial frequencies of the electric amplitude distribution at the coverslip

are lost, but on the other side some spatial frequencies (black cap) are gained. For the incoherent 3D OTF, *i.e.* the autocorrelation of the pupil, this leads to a change of its 3D shape corresponding to a rotation of the incoherent OTF.

Let us denote the k -sphere the McCutchen pupil which corresponds to the non-tilted system with coordinate system (k_y, k_z) and k' -sphere the one which corresponds to the tilted system, expressed under the coordinate system (k'_y, k'_z) . To calculate the field at a given image plane that is normal to the optical axis, the electric field belonging to the k' -sphere is firstly calculated with consideration of the relevant Fresnel coefficients of the field. Only the part of the field that is within the McCutchen pupil is collected. The field on the 3D k' -sphere is propagated to the desired z -plane and is projected onto the plane normal to the optical axis. In addition to the aplanatic correction (see Section 2.1.3), the energy due to the tilting needs to be conserved. This corresponds to the integrated intensity of the Fourier spectrum of the field in the object plane having to be the same to the Fourier spectrum of the field in the image plane in a lossless system. This implies that the superposition of the field in the pupil plane to obtain the field in the image plane must be done over the coordinate system (k_x, k_y) . In addition, since the field in k' -sphere is expressed in the coordinate system (k'_x, k'_y, k'_z) and the field at frequency equal to (k_x, k_y, k_z) is needed in the image plane, a Jacobian factor, \mathfrak{J} , is required to change the integration limits (k_x, k_y) of the projected field from the k' -sphere to be (k'_x, k'_y) . This physically expresses the energy conservation. We have $(k'_x, k'_y, k'_z) = M^{01}(\alpha, \beta)\{k_x, k_y, k_z\}$ with M^{01} being a rotation matrix to go from k -sphere to k' -sphere and given by:

$$M^{01}(\alpha, \beta) = \begin{pmatrix} \cos \beta & \sin \beta & 0 \\ -\sin \beta \cos \alpha & \cos \beta \cos \alpha & \sin \alpha \\ \sin \beta \sin \alpha & -\cos \beta \sin \alpha & \cos \alpha \end{pmatrix} \quad (3.6.1)$$

Eq. (3.6.1) is a general rotation matrix accommodating the azimuthal angle, β , of rotation of the pupil about k_z .

The same principle can be applied if instead the object plane is normal to the optical axis but the image plane is inclined. This has been demonstrated to be true in [45]. In this case, a special care needs to be taken in the definition of the coordinate system in the object and image plane. The rotation matrix M^{01} and the limits of integration in Step 11 of Algorithm 5 should be in the coordinate system of the inclined image plane. Therefore, an appropriate Jacobian factor should be applied to conserve the energy and to integrate the field in the coordinate system of the object plane in order to obtain the field in the image plane.

3.6.2 Aberration due to refractive index mismatch and tilted coverslip

A refractive index mismatch in the sample and immersion medium and tilt in the coverslip induce aberration into the system. The standard design condition (DC) for conventional light microscope is such that the sample is placed at the sample-side surface of the coverslip with a given thickness and imaged through a microscope objective lens with a given immersion medium and working distance. This is however not the case in real life experiment. The optical path deviates from this DC to a non-design condition (NDC) as the constant parameters (refractive index, sample thickness) and acquisition parameter may differ from the desired parameters in the DC. The optical path difference (OPD) between the DC and NDC is not zero and represents the phase aberration in the system. To calculate this OPD at a given azimuthal angle ϕ and at a refracted angle θ in the back focal plane region, a vector formulation of each ray at each interface is needed if the coverslip is tilted. If each interface is perpendicular to the optical axis, a scalar formulation is sufficient to calculate the OPD. In this calculation, we consider the general formulation of the OPD in case the coverslip is tilted and the sample plane is parallel to the coverslip surface. The present formulation is valid for one layer of the sample but it can be extended to many layers of samples which are assumed to be parallel to the inclined coverslip. For the calculation of the OPD, let us consider the Fig. 3.10. The optical path in the DC follows the black path formed by the points O , B , C , and H while the optical path in the NDC is formed by O_s , A_1 , B_1 , and C_1 . The two optical paths are parallel and in phase after the points H for the DC and C_1 for the NDC. In the NDC, the coverslip is tilted, hence the immersion medium - coverslip and coverslip-sample interfaces, $\kappa_{\text{im-cs}}^1$ and $\kappa_{\text{cs-s}}^1$ respectively. The OPD is given by:

$$\text{OPD} = [O_s A_1 B_1 C_1] - [OBCH], \quad (3.6.2)$$

The expression of the OPD which corresponds to a tilted coverslip with varying refractive index is found to be:

$$\text{OPD} = n_i t_i \Delta z \cos \theta_i + \text{OPD}_g + \text{OPD}_s - \text{OPD}_g^* - \text{OPD}_i^*, \quad (3.6.3)$$

with the first term $n_i t_i \Delta z \cos \theta_i$ corresponds to defocus aberration, OPD_g and OPD_s are the terms of the OPD which correspond to the variation in refractive index and thickness of the coverslip and sample in non-design condition respectively, OPD_g^* and OPD_s^* correspond to the terms of the OPD which are function of the refractive index and thickness of the coverslip and the working distance in the design condition. The

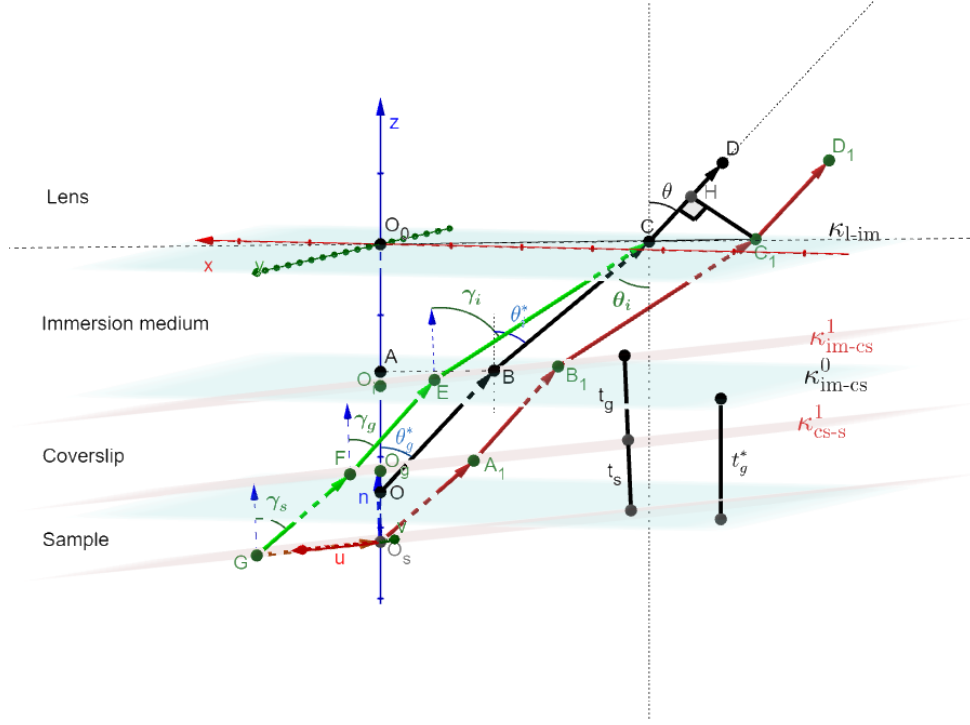


Figure 3.10: Illustration of the optical path at a given design condition (DC) and under an arbitrary non-design condition (NDC) at a given azimuthal angle ϕ and refracted angle in the lens system θ . $[O_s A_1 B_1 C_1 D_1]$: optical path in NDC (red line). $[OBCD]$: optical path in DC (black line). $[GFEH]$: translation of the path $[O_s A_1 B_1 C_1 D_1]$: from C_1 to C .

expressions of $OPD_{j|j=g,s}$ and $OPD_{j|j=g,i}^*$ are found to be as follow:

$$OPD_j^* = n_j^* t_j^* \left[\cos \theta_j^* - \left(\frac{n_i}{n_j^*} \right)^2 \cos \theta_i \right], \quad (3.6.4)$$

$$OPD_j = n_j t_j \left[\cos \gamma_j + \frac{n_i}{n_j} \left(-\cos \gamma_i + \left(1 - \frac{n_i}{n_j} \right) \cos \theta_i \right) \right]. \quad (3.6.5)$$

A detailed description of the derivation of Eq. (3.6.3), (3.6.4) and (3.6.5) is given in Appendix A. By investigating the decomposition of the cosine terms of those equations in terms of Zernike polynomials (see Appendix A.2.3 and A.2.2), it is found that the expression of the OPD throughout the sample (s), coverslip (g) and immersion (i) medium can be linearized to:

$$OPD = \sum_{j=s,g,g^*,i^*} n_j t_j \left\{ C_0^0 + C_2^2 Z_2^2 + C_2^{-2} Z_2^{-2} + \sum_{n=0}^N C_n^0 Z_n^0 + \sum_{n'=1}^{N+1} C_{n'}^1 Z_{n'}^1 + \sum_{n'=1}^{N+1} C_{n'}^{-1} Z_{n'}^{-1} \right\}. \quad (3.6.6)$$

Astigmatism (Z_2^{-2} and Z_2^2) and coma aberrations ($Z_{n'|n'>1}^{-1}$ and $Z_{n'|n'>1}^1$) are induced alongside with spherical ($Z_{n>2}^0$), defocus (Z_2^0) and tilt aberrations (Z_1^{-1} and Z_1^1). A piston or bias is contained in the constant C_0^0 . The aberrations coefficients C_n^m and piston C are functions of the refractive index ratio n_{ij} related to the medium j and the immersion medium i , the tilt parameters α and β and η . A further investigation of the

amplitude of each aberration and wavefront error with respect to the tilt angle and refractive index mismatch is conducted in Chap. 4. In this investigation, the factor $n_j t_j$ is included in the Zernike coefficients C_n^m . We regroup all the coefficients which correspond to a given Zernike polynomial of order (n, m) in C_n^m . The coefficients are therefore expected to vary linearly with the thickness t_j but not necessarily with n_j . The coefficients are non-linear with the tilt parameters (α, β) .

3.6.3 Algorithm for calculating an aberrant PSF with tilted coverslip

Here we present one way for calculating an aberrant PSF with a tilted coverslip. This method is based on the SP-FFT method described in Section 3.5.1.1. The Algorithm 1 is modified to accommodate the theory discussed in the previous sections 3.6.1 and 3.6.2 and obtain the result in Algorithm 5.

Algorithm 5 Slice propagation: SP-FFT with Tilt

Input: $NA_{\text{eff}}, \lambda_{\text{em}}, z, N_{xy}, p_{x,y}, \alpha, \beta$

Output: [h : PSF intensity; \vec{h}_{amp} : complex amplitude field]

- 1: Calculate (k_x, k_y, k_z) given $NA_{\text{eff}}, \lambda_{\text{em}}, z, N_{xy}, p_{x,y}$
 - 2: Calculate the rotation matrix $M^{01}(\alpha, \beta)$
 - 3: Calculate $(k'_x, k'_y, k'_z) = M^{01}(\alpha, \beta) \{k_x, k_y, k_z\}$
 - 4: Calculate $\cos \theta = k'_z/k_0$ and $\sin \theta = \sqrt{k'^2_x + k'^2_y}/k_0, k_0 = 2\pi/\lambda_{\text{em}}$
 - 5: Calculate the Jacobian $\mathfrak{J}(k'_x, k'_y) = \frac{\partial k_x}{\partial k'_x} \frac{\partial k_y}{\partial k'_y} - \frac{\partial k_x}{\partial k'_y} \frac{\partial k_y}{\partial k'_x}$
 - 6: Define the 2D incident polarized transverse wave $\vec{E}_i = (E_x, E_y)$ at the pupil plane
 - 7: Project \vec{E}_i onto the k' -sphere using Eq. 3.3.3 to obtain $\vec{E}'_k(0) \in \text{McCutchen pupil}$
 - 8: Apply the factor $1/AF_{amp}$
 - 9: Propagate to the desired z -plane: $\vec{E}'_k(z) = 1/AF_{amp} \cdot \vec{E}'_k(0) \cdot e^{ik'_z z}$
 - 10: Apply the phase aberration modification: $\vec{E}''_k(z) = \vec{E}'_k(z) \cdot e^{i\Phi}$
 - 11: Project along $k_x k_y$ -plane (sum over k_z) and apply the energy conservation due to the tilt: $\vec{h}_{amp} = \text{FFT}^{-1}_{2D|_{xy}} \left(\vec{E}''_k(z) |\mathfrak{J}(k'_x, k'_y)| \right)$
 - 12: Calculate the PSF intensity: $h = |\vec{h}_{amp}|^2$
-

The SP-CZT, F-Shell and Sinc-R methods can be modified in a similar fashion to include the effect of a tilted plane. To illustrate the effect of the tilt aberration, we simulate the three components of the electric field in the pupil plane (see Fig. 3.11) and the corresponding PSFs at the focus and at a defocus position equal to $u = 60$ o.u., o.u. being the axial optical unit, using Algorithm 5. The radial and axial optical coordinates are used to represent the spatial coordinates in scale of the optical resolutions. They are dimensionless. Those coordinates will be used throughout this

document and are defined as follows [75]:

$$v = \frac{2\pi NA}{\lambda_{\text{em}}} \sqrt{x^2 + y^2} \quad \text{radial optical coordinate} \quad (3.6.7)$$

$$u = \frac{8\pi n}{\lambda_{\text{em}}} \sin^2\left(\frac{\theta_{\text{max}}}{2}\right) z \quad \text{axial optical coordinate} \quad (3.6.8)$$

The optical system consists of a water immersion objective lens of $NA = 1.2$ and working distance equal to $1.5 \cdot 10^5$ nm. The emission wavelength is 510 nm. The point emitter is embedded in an embedding medium of the same refractive index as water 1.33 and the sample thickness is $t_s = 10^3$ nm. The coverslip is of refractive index 1.518 and thickness $1.7 \cdot 10^5$ nm. Here, we visualize the effect of a 1° tilt about the y -axis in the coverslip (Fig. 3.11(top line)) compared to a non-tilted plane (Fig. 3.11(bottom line)).

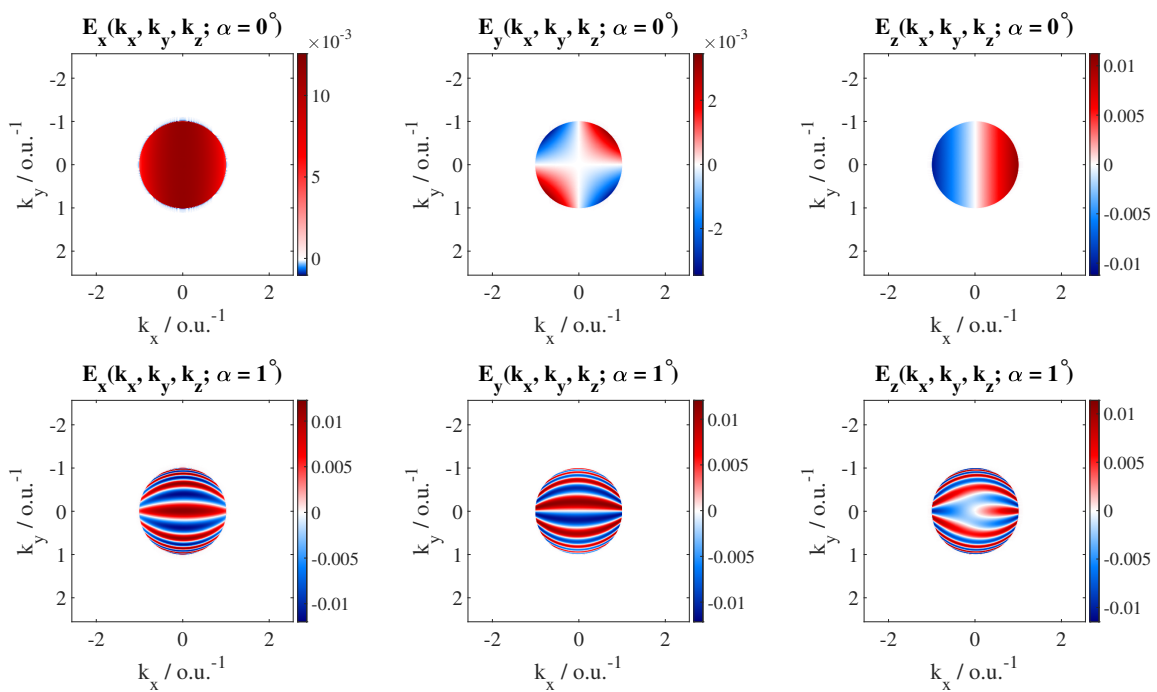


Figure 3.11: The three components (E_x, E_y, E_z) of the electric field in the pupil plane for a non-tilted coverslip (top line) and a tilted coverslip by $\alpha = 1^\circ$ (bottom line). o.u. stands for optical unit.

The tilt induces periodicity, along the direction under which the system is tilted, in the electric field pattern in the back focal plane. The radial symmetry in the PSFs is broken due to the aberrations induced by the tilt in addition to the spherical aberration. The center of the beam is also shifted from the centre of the figure (see Fig. 3.12). With just a 1° tilt, the discrepancy in the PSF is already much more pronounced (Fig. 3.13(top line) for tilt angle $\alpha = 0^\circ$ vs Fig. 3.13(bottom line) for tilt angle $\alpha = 1^\circ$).

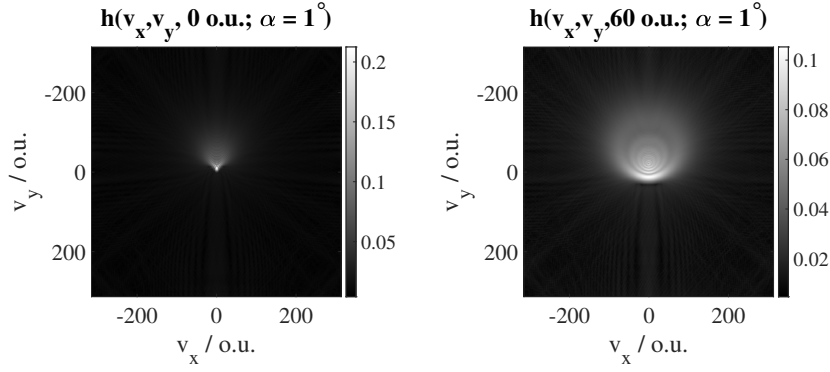


Figure 3.12: Display at $\gamma = 0.2$ of the lateral profiles of tilted PSFs at $\alpha = 1^\circ$ about the x -axis at the focus (left) and at a defocus position $u = 60$ o.u. (right).

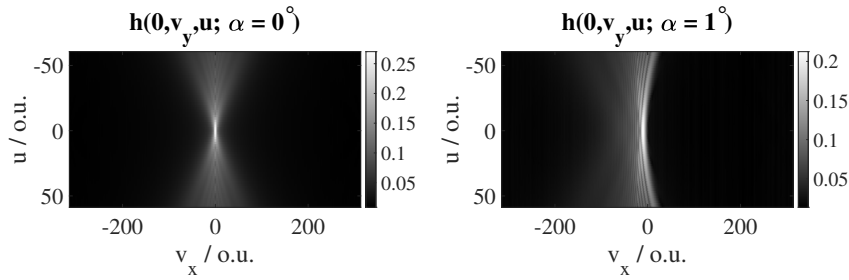


Figure 3.13: Display at $\gamma = 0.2$ of the yz -profiles of non-tilted PSF (left) and tilted PSF (right)

3.7 Dipole emission Point Spread Functions

A fluorescent emitter can radiate isotropically, but it can also behave like an electric dipole emitter. It can rotate freely between the excitation and emission or be fixed [28]. The PSF of an emitting dipole in the focal plane depends on the polarization of the illumination light and the dipole orientation in space. To describe the dipole emission, let $\vec{\mu}(\theta_{\text{dip}}, \phi_{\text{dip}})$ denotes the transition dipole moment, which is function of its zenith θ_{dip} about the x -axis and azimuth ϕ_{dip} about the optical z -axis angles. The following steps describe how to accommodate a fixed dipole into the PSF calculation with a non-polarized illumination light.

To calculate the intensity in the back focal plane of a dipole emitter with a given transition dipole orientation, the same steps as described in Algorithms 1, 2, 3 or 4 are to follow but instead of taking the amplitude field in the image plane, the user is to use the 3D amplitude field in the McCutchen pupil.

If the illumination light is non-polarized or circularly polarized, averaging over all the transition dipole moment or summing over three different perpendicular dipole orientations leads to the same resulted PSF of an isotropic emitter with a circular polarization (see Appendix C). The resulting PSF of an isotropic emitter is:

$$h_{av} = \frac{1}{4\pi/3} \int_0^{2\pi} \int_0^\pi h_{\text{dip}} \sin \theta_{\text{dip}} d\theta_{\text{dip}} d\phi_{\text{dip}}. \quad (3.7.2)$$

However, if the illumination light only contains a single linear polarization, averaging

Algorithm 6 Dipole emission PSF**Input:** $NA_{\text{eff}}, \lambda_{\text{em}}, z, N_{xy}, p_{x,y}, \vec{\mu}$ **Output:** h_{dip}

- 1: Calculate the 3D field amplitude distribution \vec{h}_x from an x -polarized incident light in the image plane using Algorithm 1, 2, 3 or 4
- 2: Project \vec{h}_x on the dipole orientation $\vec{\mu}$ to obtain $\vec{h}_x \cdot \vec{\mu}$
- 3: Calculate the absolute square of the scalar product to obtain the detected intensity $I_x = |\vec{h}_x \cdot \vec{\mu}|^2$ as measured through an analyzer oriented along x
- 4: Repeat steps 1, 2 and 3 for an y -oriented analyzer leading to $I_y = |\vec{h}_y \cdot \vec{\mu}|^2$
- 5: Obtain the PSF of the dipole emitter as the average intensity without analyzer:

$$h_{\text{dip}} = \frac{1}{2}(I_x + I_y). \quad (3.7.1)$$

over all the dipole orientations does not lead to a symmetric PSF. Further study in polarization in fluorescence microscopy is found in [28].

3.8 Space-variant imaging

The last consideration in our PSF calculation in this study is the space-variance condition. Formulating the optical imaging in terms of optical transfer function eases the mathematical modelling of the system but does not necessarily reflect the real imaging process. This formulation is based on the Abbe sine condition when imaging a plane to a plane. The system is shift-invariant in the xy -plane, and linear, and it is called a linear shift invariant system (LSI). Realistic imaging system might not necessarily be space-invariant due to distortions that may be present in the system. The refractive index of the immersion medium or the sample for instance may vary laterally. For this particular case, the McCutchen pupil formed by the \vec{k} -wavevectors from an emitter placed at a radial position $r'_1 = (x'_1, y'_1)$ is different from the McCutchen pupil from an emitter at a different position $r'_2 = (x'_2, y'_2)$ in the same z -plane. The PSF is then different at different positions of the given object plane and the system is no longer shift-invariant but linear shift variant (LSV). The image formation model for a space-invariant system described in Eq. (2.4.3) becomes as follows if the system is shift variant:

$$I(r) = \iint_{-\infty}^{+\infty} O(r')h(r, r')dr', \quad (3.8.1)$$

where $h(r, r')$, the PSF in the image plane, depends on the emitter position r' in the object plane and r is the image coordinate. A LSV-PSF can be approximated using a set of finite LSI-PSFs. An approximation to the LSV situation is obtained by windowing the LSV-PSF to N sections *i.e.* $h(r, r') \approx \sum_{n=1}^N h_n(r - r')w_n(r')$. The window function w_n is defined further down below. The resulting image is given as follows for a LSV-imaging system:

$$I_{LSV}(r) = \sum_{n=1}^N \iint_{-\infty}^{+\infty} [O(r')w_n(r')]h_n(r-r')dr', \quad (3.8.2)$$

with

$$w_n(r') = \begin{cases} 1 & \text{if } r' \in [r'_n, r'_{n+1}] \\ 0 & \text{otherwise} \end{cases}$$

From Eq. (3.8.2), it is seen that the image formed from a LSV system can be approximated by a set of subregions delimited by the coordinates r'_n formed by a spatial convolution of the object with singular LSI-PSF.

3.9 Limitation of wide-field microscopy

The PSF calculated and described until this point corresponds to the PSF of a wide-field microscope, limited by the optical resolution: Abbe limit.

The resolution limit of a conventional microscope can be derived using its frequency support, named optical transfer function (OTF). The OTF represents the three-dimensional region that is transmitting signal through the system [14]. It can be obtained from the 2D Fourier transform of the PSF intensity normalized by its value at zero-frequency, *i.e.* the integrated intensity or the total energy of the PSF over space which is equal to the integrated intensity of the field in Fourier space according to Parseval theorem [14]. For incoherent imaging, the OTF is the normalized autocorrelation of the amplitude transfer function (ATF). The ATF corresponds to the Fourier transform of the amplitude spread function \vec{h}_{amp} . It is the pupil distribution electric field, \vec{E}_k , that is represented on the McCutchen pupil. The mathematical expression of the wide-field OTF is give as follows [14]:

$$\mathcal{H}(k_x, k_y) = \frac{\iint_{-\infty}^{+\infty} \vec{E}_k(p + \frac{k_x}{2}, q + \frac{k_y}{2}) \vec{E}_k^*(p - \frac{k_x}{2}, q - \frac{k_y}{2}) dpdq}{\iint_{-\infty}^{+\infty} |\vec{E}_k(p, q)|^2 dpdq}. \quad (3.9.1)$$

Eq. 3.9.1 enables the interpretation of the OTF as the union of two displaced pupil functions centred at $(k_x/2, k_y/2)$ and $(-k_x/2, -k_y/2)$ respectively. In terms of convolution, this area corresponds to the convolution of the pupil function with itself mirrored at the zero-frequency about the lateral space (see Fig. 3.14).

In Fig. 3.14, the resulting convolution of the field in the pupil plane (Fig. 3.14a) with its mirror as previously described (Fig. 3.14b) forms a volume which represents the OTF of the optical system (Fig. 3.14c). The OTF which corresponds to a radially symmetric PSF with symmetric aberration or aberration-free, is real-valued. Only the information within this frequency support (grey region in Fig. 3.14c) will be transmitted throughout the imaging process. The frequency spectrum within the region having the form of a cone centred at the zero-frequency will be lost (blue region in Fig. 3.14c). This region is called the “missing cone”. This cone explains the

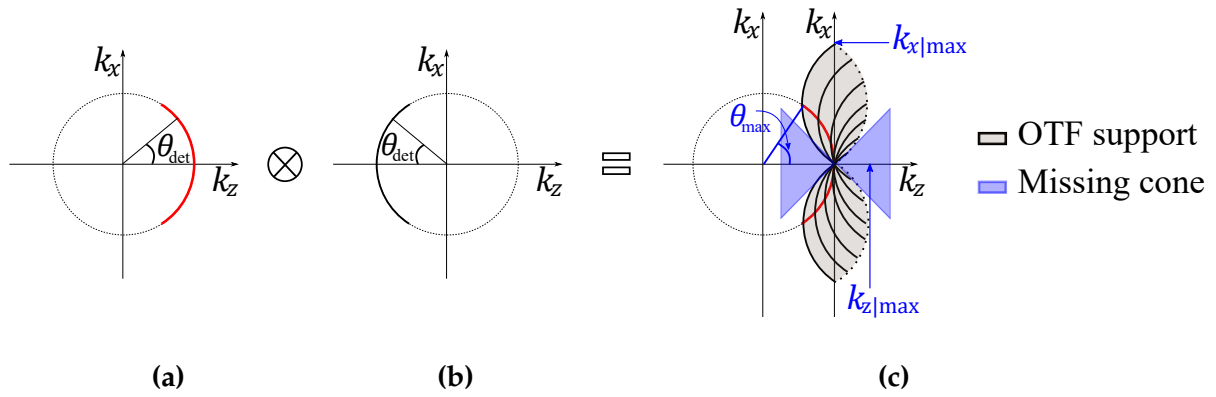


Figure 3.14: Optical transfer function in a conventional incoherent imaging system. (a) ATF in the pupil plane (red solid line). (b) Mirror of the pupil plane about the lateral space (black solid line). (c) Convolution of the pupil function (red solid line) with its mirror (black solid line) forming the OTF support (grey fill).

limitation of a conventional microscope to obtain a sharp image at a higher depth. One of the goals of many advanced techniques is to fill this missing cone such that high resolution imaging is achieved in lateral and axial direction [2, 5, 76, 77, 78, 79]. Using the frequency support, the cut-off frequency $k_{x|\text{max}}$ and $k_{z|\text{max}}$ are found to be:

$$k_{x|\text{max}} = \frac{4\pi n \sin \theta_{\text{max}}}{\lambda_{\text{em}}} \quad \text{and} \quad k_{z|\text{max}} = \frac{2\pi n(1 - \cos \theta_{\text{max}})}{\lambda_{\text{em}}}, \quad (3.9.2)$$

with n being the immersion medium refractive index and θ_{max} is the maximum angular aperture (see Fig. 3.14c). The spatial lateral and axial resolution in real space are derived respectively as:

$$d_{xy|\text{lim}} = \frac{2\pi}{k_{xy|\text{max}}} \quad \text{and} \quad d_{z|\text{lim}} = \frac{2\pi}{k_{z|\text{max}}}. \quad (3.9.3)$$

Fluorescence imaging methods have evolved rapidly in the last past decade to break this limit and to fill the missing cone [8, 9, 79]. The PSF of those advanced imaging techniques can be derived from the knowledge of the wide-field PSF. These advanced imaging techniques can be advantageous in many ways but they can be costly, temporally limited and may compromise the health of the samples [9]. They perform at higher resolution than the wide-field imaging by filling the missing information in the frequency support or extend it (e.g. [76]). Engineering the PSF in a particular way can also yield to high resolution imaging [80].

Chapter 4

Theoretical Analysis of the Point Spread Functions

The Point Spread Function (PSF) is estimated and modelled under a large set of (often) unknown parameters. A numerical investigation on PSF sensitivity to a change on its constant parameters such as coverslip tilt and refractive index mismatch is important to predict the extent at which an experimental validation of the PSF model is accurate. This is one of the focus of this chapter. The newly developed PSF models are also compared to the existing state-of-the-art PSFs to demonstrate the theoretical pros and cons of each PSF model.

4.1 Introduction

The study of the PSF sensitivity to its constant parameters is important to estimate the error and accuracy at which the experimental validation of the PSF is valid. In Section 4.2.1, we firstly investigate *the sensitivity of the PSF to refractive index mismatch and tilt of the coverslip*. A non-aberrant PSF forms the reference in the analysis. In Section 4.2.2, we examine the effects of these aberrations into the optical resolution by analysing the OTF. It is also important to mention that the fluorescence emission typically comprises of an entire spectrum, and not just one single wavelength. Therefore, assuming that an experimental PSF is derived from the fluorescence emission at a single wavelength is incorrect. In Section 4.2.3, we demonstrate *the possible error that might occur given this assumption of a single emission wavelength in the calculation of the PSF*. In the last investigation, we will determine *the point at which the scalar field approximation is no longer valid and a vector formulation of the PSF is necessary* (see Section 4.2.4).

In the second part of this chapter, *we compare the PSF models newly developed and discussed in Chap. 3 with the state-of-the-art PSFs*. These newly developed methods will be distinguished from the state-of-the-art PSFs in the comparison process by marking their names with an asterisk (*). These regroup the SP-FFT*, SP-CZT*, F-Shell* and Sinc-R*. Five different PSF models form the state-of-the-art in this investigation. The

Richards and Wolf vector PSF from PSFGenerator is one of the state-of-the-art PSFs that has been widely used in the literature [33]. This PSF is denoted by PSFGen and is computed at the best accuracy setting of the software in our comparison. The second state-of-the-art PSF model is a scalar PSF model based on the Gibson and Lanni study and was computed by Li et al. using a linear combination of rescaled Bessel functions [34]. We denote this model by GL. The third and fourth state-of-the-art PSF model were developed by Aguet et al. [37]. These models use a numerical integration based on Simpson's rule to compute the scalar, denoted by sPSF, and vectorial diffraction integral, denoted by vPSF. The fifth and last state-of-the-art PSF model is also based on the Richard and Wolf findings. We denote this PSF by RW. The initial code for this model was written using the C programming language by Peter Verveer and uses a DIPimage Library. This software code can be called on MATLAB and is included in our PSF toolbox. It is chosen as a gold standard in the comparison as its mathematical expression still remains the best representation of the diffraction-limited image field. It avoids any fast Fourier transform (FFT), which could be prone to artefacts and calculates the integrals directly in real-space. The pros and cons of each model are discussed in depth in this section.

To complete the investigation, a list of image quality and similarity metrics need to be priorly defined. This list regroups the standard deviation of a signal (Std), the waveront error σ_W , the Strehl ratio S , mean relative error (MRE), and normalized cross correlation (NCC). The wavefront error measures the deviation of the measured wavefront from the wavefront in a design condition. The Strehl ratio quantifies the amount of aberration in an aberrant PSF compared to an aberration-free PSF by measuring the ratio of the intensity of the aberrant PSF at its centre spatial position and the aberration-free PSF at the same position. The MRE measures the errors between a ground truth and a given model. The NCC quantifies the similarities between both ground truth and measured or theoretical model. The NCC is more meaningful over the MRE when the spatial shift in the data is less important. The MRE is more sensitive than NCC to record the error in small variation of intensities. The mathematical expressions of those metrics are given in Appendix E.

4.2 PSFs sensitivities to parameter mismatch

4.2.1 Aberrations in PSFs

4.2.1.1 Simulated data

For this investigation, we simulate PSF data using the "Slice Propagation" technique described in Algorithm 1. The imaging and PSF parameters are summarized in Table 4.1. The refractive index of the sample n_s , the sample thickness t_s , and the elevation angle of the tilt in the coverslip are changed individually.

Table 4.1: Parameters for evaluating the sensitivities of the PSF to refractive index mismatch and tilting in the coverslip

Parameters :	Values
Calculation grid size (N_x, N_y, N_z):	$512 \times 512 \times 50$
Voxel size :	$83 \times 83 \times 100 \text{ nm}^3$
Emission wavelength :	$\lambda_{\text{em}} = 510 \text{ nm}$
NA :	1.2
Immersion medium RI in DC(*) and NDC :	$n_i^* = n_i = 1.33$
Coverslip RI in DC and NDC :	$n_g^* = n_g = 1.518$
Sample RI :	$n_s = n_i + 0.002j, j \in [0 : 1 : 10]$
Working distance :	$WD = 1.5 \times 10^5 \text{ nm}$
Coverslip thickness in DC(*) and NDC :	$t_g^* = t_g = 1.7 \times 10^5 \text{ nm}$
Sample thickness	$t_s = a\lambda_0, a \in [1 : 2 : 9, 50 : 50 : 250]$
Tilt elevation angle :	$\alpha \in [0^\circ : 0.1^\circ : 1^\circ]$
Tilt azimuthal angle :	$\beta = 0^\circ$

RI, DC and NDC stand for refractive index, design condition and non-design condition respectively and $\lambda_0 = \lambda_{\text{em}}/n_s$ is the vacuum wavelength. We vary the refractive index of the sample n_s in step size of 0.002. This value represents the error precision of most Abbe refractometers in measuring the RI of a medium. The step size of α is chosen based on the findings from [74] where the PSF is shown to be sensitive to a tilt of 0.1° . Lastly, the range of t_s is arbitrarily. It is chosen to accommodate a small sample depth $[1 : 2 : 9]\lambda_0$, usually assumed to be at the surface of the coverslip, and larger sample depth $[50 : 50 : 250]\lambda_0$. A water objective lens is chosen as it is mostly used in the case of biological imaging of living samples.

Each calculated PSF is normalized by the integrated intensity of the 3D volume PSF. This normalization statistically means that all photons have the same probability to be anywhere in the available space and the total probability of having photons in all of the 3D space is therefore equal to 1.

4.2.1.2 Tilt and spherical aberration

A small variation of the sample and imaging parameters can influence the PSFs. Fig. 4.1 illustrates this effect by displaying the yz -cross section of the PSFs generated with different set of imaging parameters.

We simulate several aberrant PSFs under different constant parameters ($n_s/n_i, t_s, \alpha$) and compare the resulting aberrant PSFs with non-aberrant PSFs to determine how sensitive the PSF to the change in refractive index and the coverslip tilt is. One at a time of those parameters is changed in the simulation. The details of these parameters and imaging parameters are given in Table 4.1. We compute the wavefront error, the MRE and NCC between the aberrant PSF and non-aberrant PSF and the Strehl ratio using the formulas described in Appendix E. The detailed maps of the results for the variation of each of these parameters are given in Appendix B.

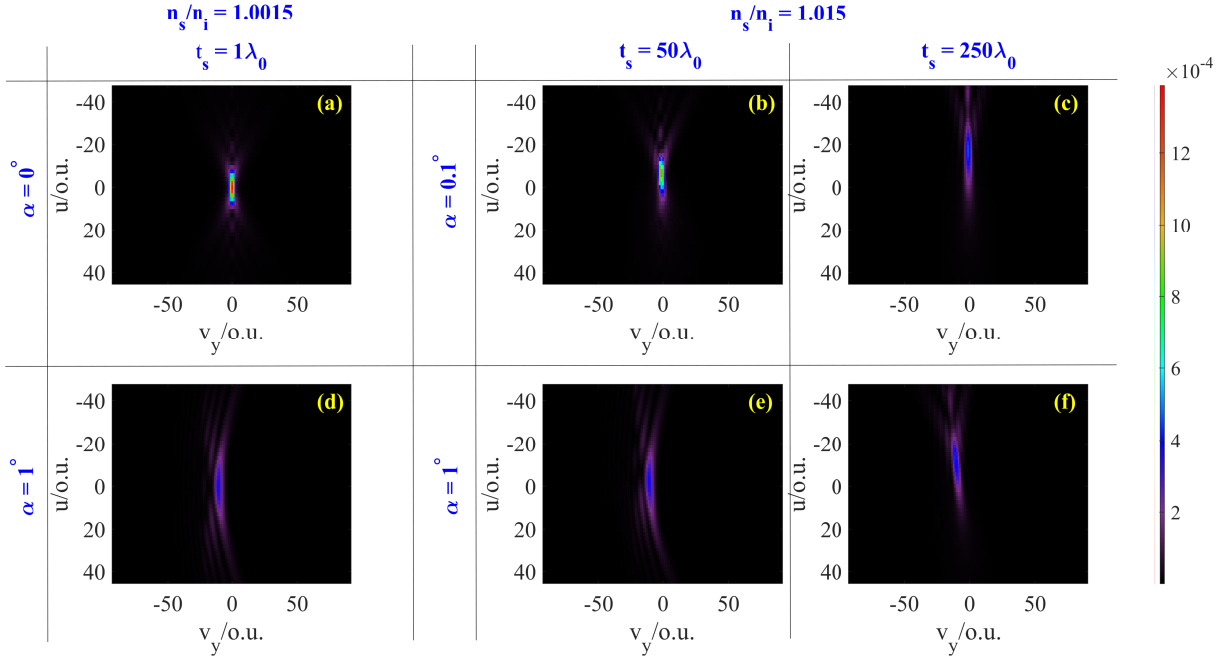


Figure 4.1: yz -cross section of aberrant PSFs with the imaging parameters: $[n_s/n_i, t_s, \alpha] =$ (a) $[1.0015, 1\lambda_0, 0^\circ]$, (b) $[1.015, 50\lambda_0, 0.1^\circ]$, (c) $[1.015, 250\lambda_0, 0.1^\circ]$, (d) $[1.0015, 1\lambda_0, 1^\circ]$, (e) $[1.015, 50\lambda_0, 1^\circ]$, (f) $[1.015, 250\lambda_0, 1^\circ]$.

For the given imaging parameters $NA = 1.2$ and $\lambda_{em} = 510$ nm, we observed from the investigation that a NCC value between non-aberrant and aberrant PSF higher than 0.9923 corresponds to a Strehl ratio higher than 0.8 of a PSF assumed to be ideal. This means that in this condition an aberrant PSF which has a similarity as high as 0.9923 with a non-aberrant PSF can be assumed to be ideal. The sensitivity error in measuring the medium refractive index 0.002 can also induce significant spherical aberration distinguishing an aberrant from a non-aberrant PSF if the thickness of the medium is greater than $50\lambda_0$. A PSF of water immersion objective lens is sensitive to a tilt of $\alpha = 0.2^\circ$ in the coverslip even if $n_s/n_i = 1$ due to the properties of the coverslip itself. The aberration introduced by the tilt of the coverslip distorts the image. This distortion can however be overshadowed and compensated by spherical aberration. By investigating the different range of embedding depth (sample thickness t_s), we found that the PSF varies with the sample thickness for $t_s \in [1\lambda_0, 9\lambda_0]$ with a maximum variation of 0.0154 at $9\lambda_0$ in the MRE. However, as long as t_s is not zero and the refractive index of the sample differs from the refractive index of the immersion medium, a spherical aberration is induced in the PSF and the wavefront error varies more with the coverslip tilt. At $t_s = 50\lambda_0$, the NCC is found to still be less dependent of n_s/n_i but it becomes more sensitive to n_s/n_i when t_s increases.

4.2.1.3 Focal shift and peak intensity

The focal position of a non-aberrant system is usually at the centre position of the 3D image. When there is no aberration, the waves mostly interfere constructively at

this position. In an aberrant system, the wavefront on the Gaussian reference sphere no longer has constant phase and the Huygens wavelets are not in phase, causing partially destructive interference. Consequently, the irradiance at the centre, *i.e.* the peak intensity drops compared to the case of a non-aberrant imaging.

In the presence of Zernike tilt aberration and its derivatives and spherical aberration, the PSF is shifted from this centre position not only along the lateral axis, but also along the axial axis, causing a “focal shift”. In the presence of spherically symmetric aberration only, this shift is only along the optical axis. In Fig. 4.2, we display the normalized relative intensity along the optical axis at the radial centre position. Each figure corresponds to a given sample depth t_s ranging from $50\lambda_0$, $150\lambda_0$ to $250\lambda_0$. The intensity profiles at a given t_s for different ratio n_s/n_i are displayed in each of the figures. The normalization corresponds to the scaling of the aberrant PSF intensity by the intensity value at the centre position of the non-aberrant reference PSF. The intensity at zero-position and displayed in Fig. 4.2 therefore represents the Strehl ratio at a given set of parameters t_s and n_s/n_i . We assumed no coverslip tilt for this particular study.

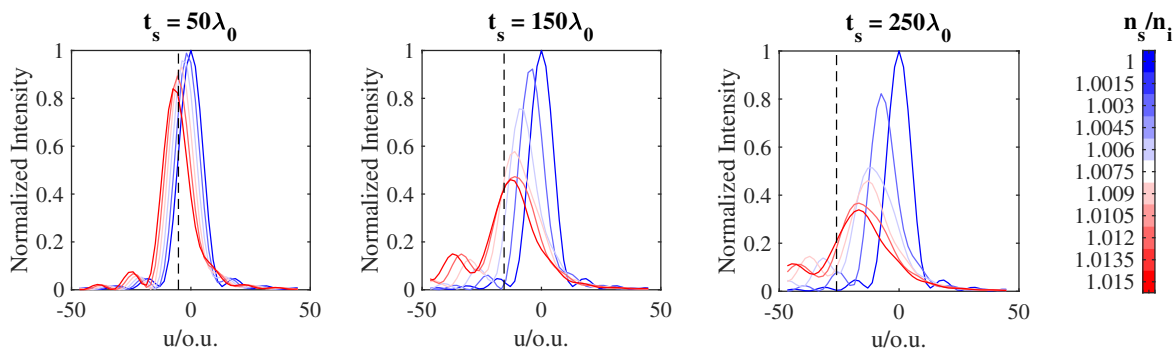


Figure 4.2: Visualization of the focal shift and peak intensity along the optical axis at $\alpha = 0$ for different t_s ranging from $50\lambda_0$, $150\lambda_0$ to $250\lambda_0$ and n_s/n_i values, $NA = 1.2$, $n_i^* = n_i = 1.33$ and $\lambda_{em} = 510\text{ nm}$. The code color blue to red in each figure corresponds to different n_s/n_i setting. The vertical black dashed line corresponds to the predicted focal position for the given $t_s = 50\lambda_0$, $150\lambda_0$ and $150\lambda_0$ at $n_s/n_i = 1.015$. The parameters of the coverslip (t_g , n_g) are fixed.

The predicted focal position can be explained and derived from a simple imaging diagram (see Fig. 4.3-upper row). In this diagram, we present the case study of $n_s/n_i > 1$ where we have a light emission from a denser medium to a less dense medium. This yields to a positive spherical aberration [39, 42]. From Snell’s law, as n_s becomes bigger than n_i , the refracted angle about the normal of incidence in the sample region becomes smaller than the incident angle from the immersion medium (angle indicated by a the black spot in Fig. 4.3-upper row). The actual focus position (AFP) therefore shifts from the nominal focus position (NFP) and yields to the focal shift. The nominal focus corresponds to the focus position in the absence of aberration. This NFP is at the emitter position within the sample so $NFP = t_s$. Due to the

RI mismatch between the sample and the immersion medium, the focus position gets scaled by a stretch factor n_s/n_i yielding to the value of the AFP = NFP $\times (n_s/n_i)^{-1}$. The pixel size in z is re-interpreted and the focal shift (FS) is given by:

$$\text{FS} = \text{NFP} - \text{AFP} = t_s \left(\frac{n_s/n_i - 1}{n_s/n_i} \right). \quad (4.2.1)$$

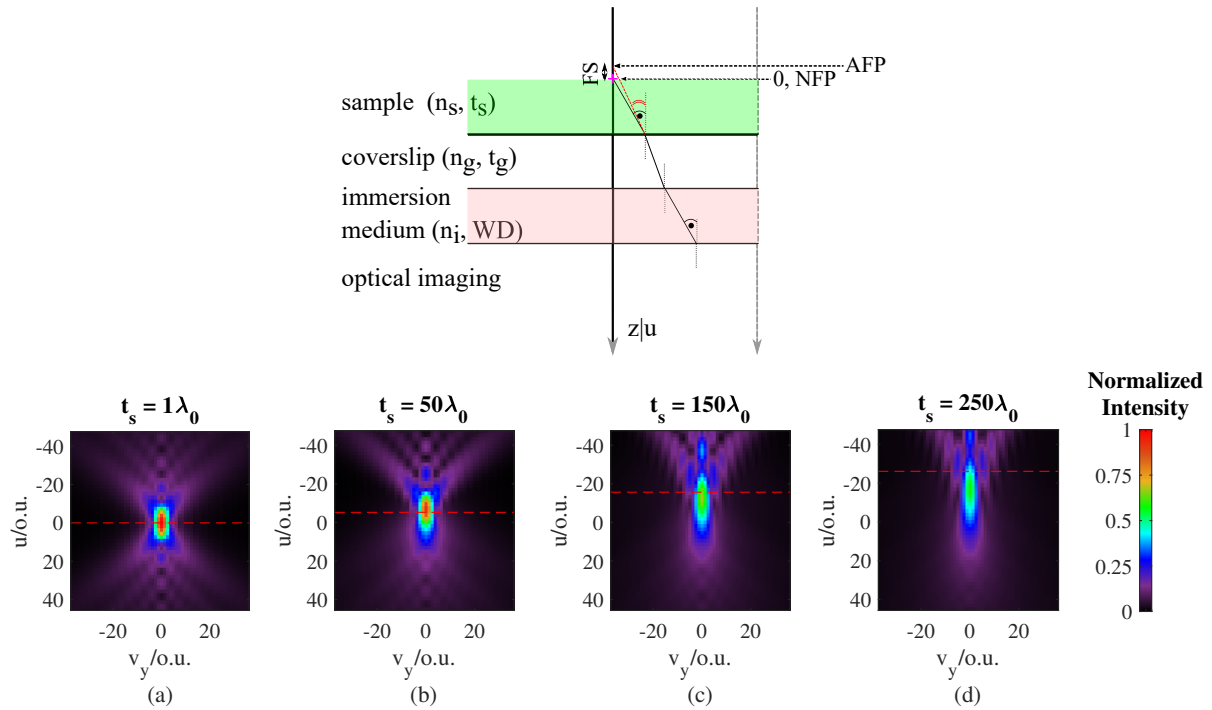


Figure 4.3: Upper row: Representation of the focal shift in a simple imaging diagram, case study of $n_s/n_i > 1$ which corresponds to a positive spherical aberration. NFP: nominal focal position when there is no aberration. AFP: actual focal position in the presence of aberration. FS: focal shift. Lower row: yz -profiles of PSFs at $\alpha = 0^\circ$. (a) $n_s/n_i = 1$ and $t_s = 1\lambda_0$. (b, c, d) $n_s/n_i = 1.015$ and $t_s = 50\lambda_0, 150\lambda_0, 250\lambda_0$ respectively. The red lines indicate the focal positions. The colorbar represents the range of the intensity values in all of the four figures (a, b, c, d).

Fig. 4.3-lower row(a) represents the yz -profile of the non-aberrant reference PSF. The red dashed lines in 4.3-lower row(a, b, c, d) correspond to the black dashed lines in Fig. 4.2. In the case of light transmission from a less dense medium to a denser medium, *i.e.* $n_s/n_i < 1$, we have a negative spherical aberration and the position of the AFP is above the NFP within the sample medium (green region in Fig. 4.3-upper row). The positive direction of z is pointed by the arrow in Fig. 4.3-upper row. By quantifying these focal shifts, we found an estimate of $5.597 \mu\text{m}$ focal shift per λ_0 or 0.1043 o.u. per λ_0 in terms of the axial optical resolution.

4.2.2 Aberrant OTFs

The aberration present in the system also affects the optical resolution of the system and the contrast in the recorded image. As mentioned earlier in Chap. 3, a plane

wave, directed by a wavevector \vec{k} in real space, corresponds to a delta function at a position \vec{k} on the McCutchen pupil in Fourier space. If the wavefront on the Gaussian reference sphere deviates from being spherical, an additional phase Φ is added in Fourier space by multiplying the field distribution on the pupil by $e^{i\Phi}$. For this reason, the real part of the amplitude of the field in the pupil plane is reduced by the factor $\cos(\Phi)$. Computing the autocorrelation of the field in the pupil plane using Eq. (3.9.1), an OTF with a possible negative value is obtained at $\Phi \neq 0$. Due to the Parseval's theorem, the energy is conserved in frequency as in real space. This explains the contrast reversal in the recorded image and possible cut-off frequency of the OTF support. In Fig. 4.4, we display the $k_y k_z$ -cross section of the real part of the aberrant OTFs at $\gamma = 0.5$ under different imaging parameters.

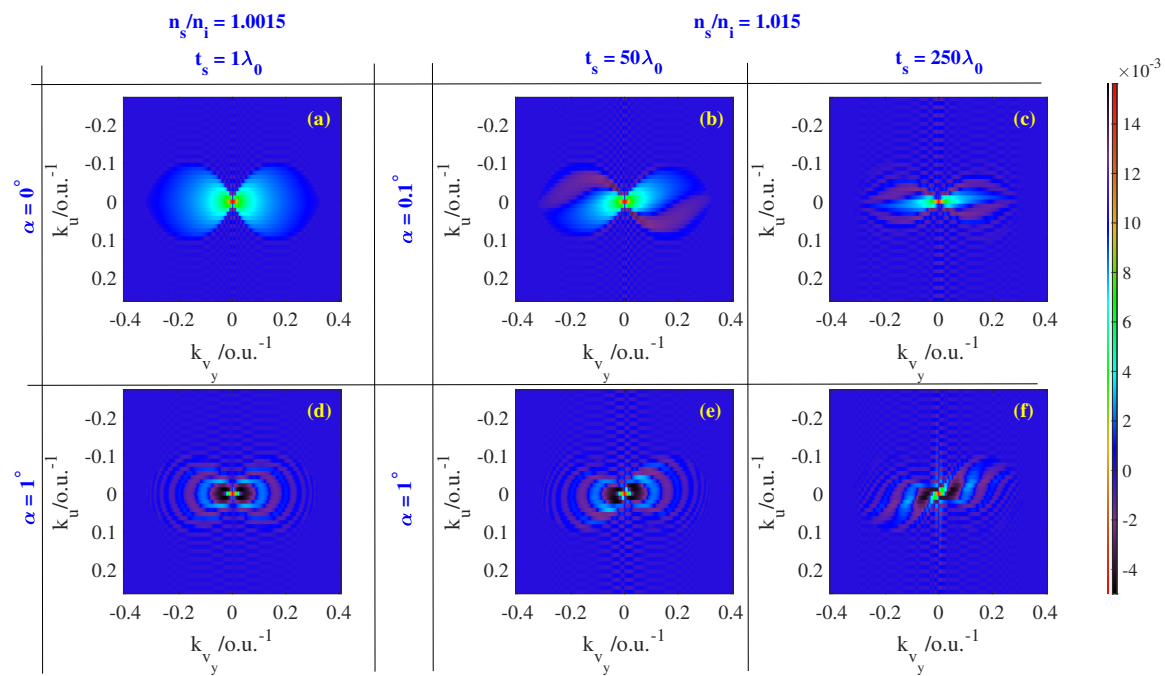


Figure 4.4: The influence of refractive index mismatch and coverslip tilt onto the OTF. The $k_y k_z$ -cross section of the real part of the aberrant OTFs at $\gamma = 0.5$ with the imaging parameters: $[n_s/n_i, t_s, \alpha] =$ (a) $[1.0015, 1\lambda_0, 0^\circ]$, (b) $[1.015, 50\lambda_0, 0.1^\circ]$, (c) $[1.015, 250\lambda_0, 0.1^\circ]$, (d) $[1.0015, 1\lambda_0, 1^\circ]$, (e) $[1.015, 50\lambda_0, 1^\circ]$, (f) $[1.015, 250\lambda_0, 1^\circ]$.

Since the values of the OTF can be negative in the presence of aberrations, the gamma display at 0.5 equals to $\text{sign}(\text{Real}(\text{OTF})) \times [\text{abs}(\text{Real}(\text{OTF}))]^{0.5}$. The $\text{abs}(\cdot)$ stands for the absolute value of the input argument, $\text{Real}(\cdot)$ corresponds to the real part and $\text{sign}(\cdot)$ is the sign.

To visualize the frequency component which corresponds to the field in focus in real space along the y -axis at $x = 0$, the Fourier slice theorem is used and the 2D $k_y k_z$ -section of the OTF is projected along k_z -axis, *i.e.* summing along k_z -axis (k_u -axis). The results under different imaging parameters are displayed in Fig. 4.5. These figures enable us to visualize how much loss in resolution is induced by each parame-

ter $n_s/n_i, t_s$ and the tilt angle α . It is predicted from these figures that the degradation of the image is significant if there is a tilt in the imaging system.

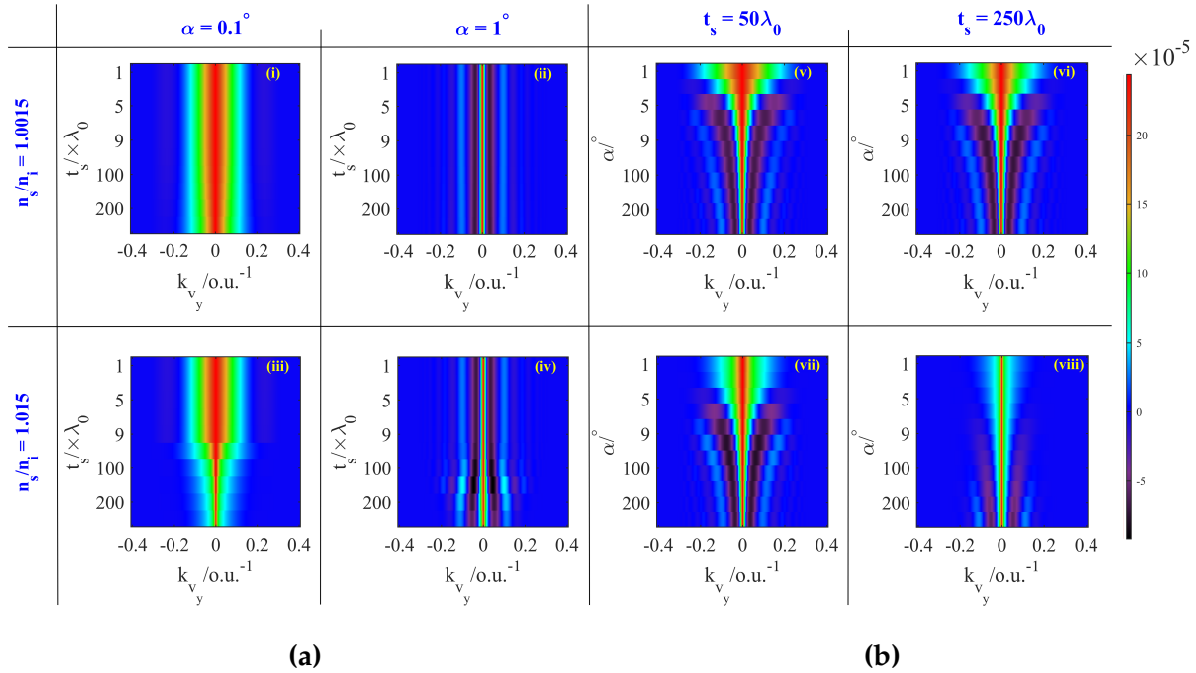


Figure 4.5: Projection of the real part of the OTF summing along k_z -axis (k_u -axis). (a) Variation of the real part of the OTF with t_s at fixed values of $(n_s/n_i, \alpha)$: (i) (1.0015, 0.1°), (ii) (1.015, 0.1°), (iii) (1.0015, 1°), (iv) (1.015, 1°). (b) Variation of the real part of the OTF with α at fixed values of $(n_s/n_i, t_s)$: (i) (1.0015, $50\lambda_0$), (ii) (1.015, $50\lambda_0$), (iii) (1.0015, $250\lambda_0$), (iv) (1.015, $250\lambda_0$).

In most cases, the imaging parameters, especially the coverslip tilt angle α , are unknowns. The phase aberration is therefore only known through a phase retrieval process of the recorded experimental PSF. The phase can easily be added into the pupil plane. Deriving the constant parameters of the imaging from the retrieved phase is not a trivial task. An error may be induced in the McCutchen pupil itself due to the lack of knowledge of α (see Section 3.6). To illustrate this concept and estimate the error that may be induced, let us consider the aberrant PSF with constant parameters at which the higher order spherical aberrations starts to be significant. That corresponds to $n_s/n_i = 1.0075$ *i.e.* $n_s = 1.34, t_s = 50\lambda_0$ and $\alpha = 1^\circ$. We denote h_1 the aberrant PSF computed with a correctly oriented McCutchen pupil and the phase aberration induced by the constant parameters and h_2 is the aberrant PSF which only accounts for the phase aberration and assumes a planar McCutchen pupil.

In this particular case, the errors in the PSFs were calculated to be fairly small and the two PSFs look almost identical. However, the OTF support is slightly extended due to this error and some artefacts can therefore be introduced into the system and might be mistaken for an important information from the object (see Fig. 4.6c).

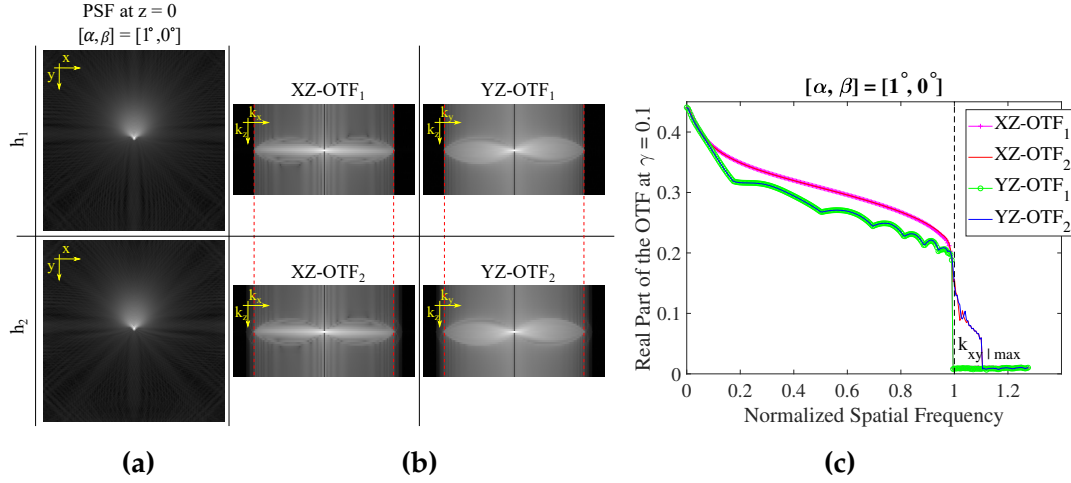


Figure 4.6: Effects of the lack of knowledge of a tilt $[\alpha, \beta] = [1^\circ, 0^\circ]$ (elevation and azimuthal angles respectively) on the OTF. (a) The in-focus PSFs displayed at $\gamma = 0.1$. In addition to the induced phase, the tilt is considered in the McCutchen pupil of the PSF denoted by h_1 . The PSF denoted by h_2 is derived from the McCutchen pupil which corresponds to a non-tilted plane with the additional phase induced by the tilting. (b) The XZ and YZ cross sections of the corresponding OTFs displayed at $\gamma = 0.1$. (c) Real part of the cross sections of the OTFs along $k_z = 0$ at $\gamma = 0.1$. The spatial frequency is normalized by the cut-off frequency $k_{xy|max}$ indicated by the black dashed line in (c) and four red dashed lines in (b).

4.2.3 Fluorescence emission band

In the above investigation, we assume a single emission wavelength in the PSF calculation. An experimental PSF data is however recorded at an emission spectrum not a single wavelength. The reconstructed PSF is obtained from an incoherent sum of PSFs recorded at single wavelengths within the emission spectrum. The range of the spectrum is delimited by the emission filter bandwidth ($\lambda_{em} \in [\lambda_{min}, \lambda_{max}]$). The effective PSF is given mathematically as [81]:

$$h_{eff}(r) = \int_{\lambda_{min}}^{\lambda_{max}} \epsilon(\lambda_{em}) h(r; \lambda_{em}) d\lambda_{em}, \quad (4.2.2)$$

with $r = (x, y, z)$ being the spatial coordinates at which the intensity PSF is evaluated, ϵ being the emission spectrum of the emitter, λ_{min} and λ_{max} are the integration bounds, and $h(r, \lambda_{em})$ is the PSF at a single emission wavelength λ_{em} . As the full-width half maximum (FWHM) of a PSF is proportional to λ_{em} , a contribution of a PSF at a longer or shorter λ_{em} broadens or narrows the effective PSF h_{eff} respectively. To illustrate the broadening effect, we imitate the PSFs of two fluorescent emitters that will be used in our experimental validation in Chap. 6: $0.2 \mu\text{m}$ FluoSpheres Carboxylate-Modified microspheres with $\lambda_{ex}/\lambda_{em} = 505/515$ [Thermo Fischer: F8811] and $0.1 \mu\text{m}$ TetraSpeck microspheres with four distinct channels: $\lambda_{ex}/\lambda_{em} = 360/430$ (blue), $505/515$ (green), $560/580$ (orange) and $660/680$ (dark red) [Thermo Fischer: T7279]. In this particular case, we use a Plan-Apochromat $63\times/1.4$ Oil DIC M27 objective lens. The system is magnified by $1.6\times$ in the tube lens. The grid is of size equal to $512 \times 512 \times 64$ and the voxel size is $64.48 \times 64.48 \times 100 \text{ nm}^3$. The sample is

assumed to be embedded in a mounting medium of refractive index equal to $n_s = 1.46$ and the coverslip is of a high performance with $n_g = 1.518$ and $t_g = 0.17$ mm. These parameters are chosen to showcase the minimum error that can be present in our experimental validation.

We download from Thermo Fisher website the emission spectrum ϵ of each bead [www.thermofisher.com]. The value of ϵ is normalized by the integrated intensity over the effective region delimited by the bandwidth of the chosen emission filters. This normalisation is done such that the probability of having photon anywhere over the available space is equal, yielding to a total probability equal to 1. Using an emission filter $[\lambda_{\min}, \lambda_{\max}]$ centred at λ_c , the lateral FWHM of the PSF calculated at a single wavelength λ_c and the lateral FWHM of the effective PSF are estimated and the results are summarized in Table 4.2.

Table 4.2: FWHM of effective PSF and PSF at a single wavelength

	FluoSpheres bead	TetraSpeck bead	
		Blue	Orange
$[\lambda_{\min}, \lambda_c, \lambda_{\max}]$	[498, 525, 551]	[417, 450, 486]	[565, 595, 637]
FWHM(λ_c)	192.02	157.9	222.49
FWHM($[\lambda_{\min}, \lambda_{\max}]$)	190.91	156.56	218.95

We also download from Omega Optical the values of the transmission coefficients which corresponds to three optical filters: 525/45 [525QM45], 450/60 [450QM60], 595/60 [595AF60] to obtain a realistic values of the transmitted and recorded fluorescent emission [www.omegafilters.com]. The FWHMs of the PSFs are calculated and displayed in Table 4.2 to demonstrate the lateral broadening of the effective PSF. Although this effect is fairly small in this particular case (less than 5 nm) and it may suffice to compute the PSF at λ_c , the broadening effect can be important and not negligible if the emission filters have not been chosen carefully [81]. It is also important to note that the data that has been used here correspond to the perfect case so the result represent the minimal error that can be obtained. Here, the FWHMs of the effective PSFs are calculated to be smaller than the FWHMs of the PSFs at the centre wavelength λ_c because the emission spectrum distribution of each bead displays a positive skewness. The PSFs at shorter wavelength have more contributions to the incoherent summation than those at longer wavelengths.

4.2.4 Scalar field approximation

The scalar field approximation is valid in the region near to the optical axis where the field dependence on the elevation angle θ is negligible ($\sin(\theta_{\max}) \lesssim 0.4$ [82]). At higher opening angle ($\sin(\theta_{\max}) > 0.7$ [82]), the vector features of the field such as the polarization and bending of the rays are no longer negligible. We observed

by comparing the non-aberrant SP-FFT PSF (see Algorithm 1) with the state-of-the-art scalar Gibson and Lanni model developed by Li et al. [34] that the scalar field approximation holds with a MRE less than 0.0349 if $NA \leq 0.4$. The vector PSF here is computed with a circular polarization state. The scalar field approximation departs from the vector formulation of the field distribution with a mean relative error (MRE) of 0.0810 and NCC value of 0.9979 from $NA \geq 0.7$. These values also hold for the comparison of the scalar and vector state-of-the-art PSFs from [37]. By analysing different PSFs with high NA using different immersion medium such that $NA/n_i \geq 0.95$, we observe a loss of at least equal to 0.0103 in the NCC value between the scalar and vector PSFs. In the presence of tilt and spherical aberrations at $\alpha = 0.2^\circ$, $n_s/n_i = 1.0015$, and $t_s = 10\lambda_0$, this loss in NCC increases about 5 times to result into an NCC value equal to 0.95 between a scalar and vector aberrant PSF.

4.3 Comparison of different computation methods

Now, let us compare the different methods for computing the PSFs and limit ourselves to non-aberrant and noise free simulated PSF models. The Richard and Wolf (RW) PSF model [23, 24] is chosen to be the gold standard of the comparison (GS) as it represents the best approximation of the light diffraction through a given optical imaging system and does only rely on calculating integrals in real space. The RW-GS is sampled $5\times$ higher than a standard PSF sampling to avoid any sampling problem in the PSF especially, near the focus position. It is down-sampled by binning 5 neighbouring pixels, centred at the desired position, in both x and y . The standard sampling consists of an xyz -grid of size $128 \times 128 \times 64$ pixels. The voxel size is $83 \times 83 \times 100$ nm³. Only 90% of the calculation grid 128×128 is considered in the comparison to avoid any artefacts that may be present at the border of the calculation region. The same objective lens and emission wavelength for the evaluation of the PSF sensitivity described in Table 4.1 are used: $NA = 1.2$, $n_i = 1.33$ and $\lambda_{em} = 510$ nm.

The methods are compared based on the violation of the missing cone in the resulting PSF, MRE and NCC to the RW-GS, wrap-around effect and calculation speed.

4.3.1 Intensity profile

To visualize the difference in intensity of the PSFs, we plot the radial mean intensity in logarithmic scale (see Fig. 4.7). We can apply the radial mean here since the PSFs are symmetric about the optical axis as only defocus aberration is present in the system. The state-of-the-art routines that we compare to: PSFGen, GL, sPSF and vPSF are not centered at the same center position as our PSFs models with even window size. They are therefore calculated from an odd window and further clipped to get the same window size as our PSFs models.

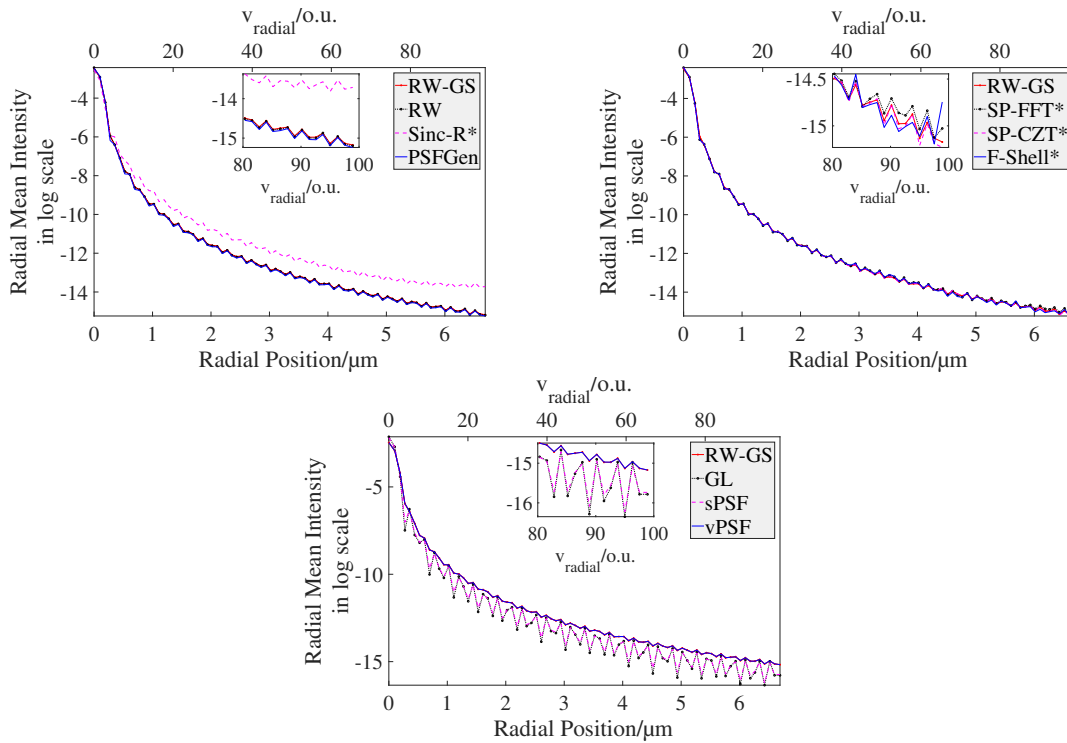


Figure 4.7: Radial mean profiles at the focus position in logarithmic scale. RW-GS refers to the Richards and Wolf gold standard PSF, RW to the Richards and Wolf PSF under a standard sampling, Sinc-R* to the PSF derived from Algorithm 4, PSFGen to the vector PSF from PSFGenerator at the best accuracy [33], SP-FFT* to the method described in Algorithm 1, SP-CZT* to the method employing Algorithm 2, F-Shell* to the Fourier shell interpolation method in Algorithm 3, GL to the scalar PSF based on the Gibson and Lanni model [34], sPSF and vPSF to the scalar and vector PSF from [37].

In Fig. 4.7, the discrepancy in the scalar PSF models are clearly visible. The vPSF and PSFGen fit the gold standard RW-GS with a high precision. The profile of Sinc-R* departs from RW-GS at the edge of the radial position. The profiles of SP-FFT*, SP-CZT* and F-Shell* are also slightly off from the profile of the RW-GS.

4.3.2 Violation of the missing cone

One condition that a wide-field system satisfies is the missing cone condition. As described in Section 3.9, this missing cone corresponds to the frequency spectrum close to the k_z -axis going missing due to the uniform illumination of the sample in a wide-field system. Information within the missing cone is not transmitted by the OTF and out-of-focus light is only spreading but not removed from the image. The integrated intensity at each axial position remains constant as long as the PSF remains confined well within the calculation grid.

A PSF model violates the missing cone problem when the integrated intensity of the PSFs for each xy -plane along the axial axis is not uniform over defocus, especially near the focus position. This violation of the missing cone often happens when the PSF is wrongly sampled. As we are dealing with a finite grid with finite number of

points, this issue must to be taken good care of. It contributes to the performance of the PSF. A PSF which violates the missing cone may no longer represent a wide-field imaging. To observe this property of a PSF model closely, the integrated intensity over xy -plane at each axial position z is calculated and displayed in Fig. 4.8.

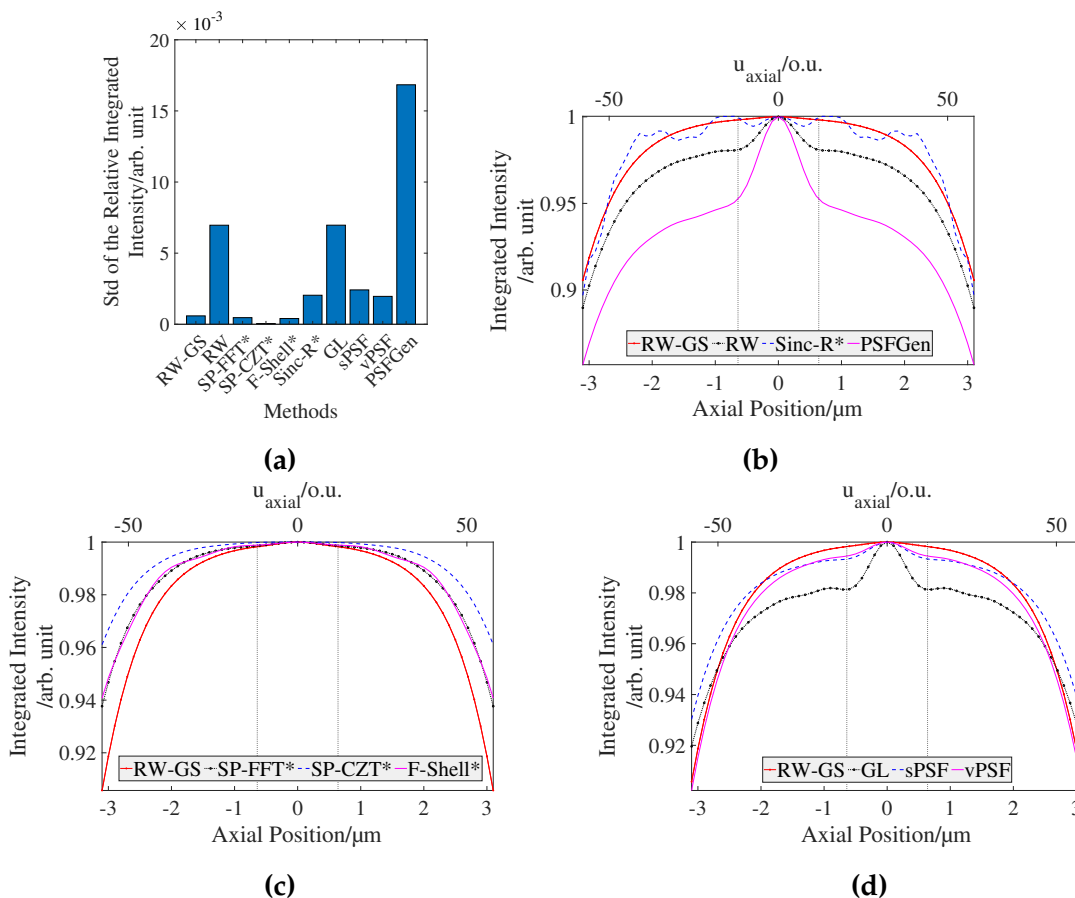


Figure 4.8: Observation of the violation of the missing cone by calculating and presenting the integrated intensity along z .

The effect is quantified by taking the standard deviation (Std) of the integrated intensities within 20% of the z -range around the focus (see the bar graph in Fig. 4.8a). This region of interest is indicated by the two vertical lines in each of the figures representing the integrated intensity. Within this region, the Std of the SP-FFT* and F-Shell* are very close to the Std of the highly sampled RW-GS while the SP-CZT* performs better than the gold standard itself with the lowest value of Std. The newly developed methods SP-FFT*, SP-CZT*, F-Shell* and Sinc-R* all have lower values of Std compared to the state-of-the-art PSF: GL, sPSF, vPSF and PSFGen. The PSFGen is in the highest position for violating the missing cone condition, followed by RW computed with a standard sampling and the GL.

4.3.3 Error analysis

To quantify the difference between each model with the predefined GS, denoted by RW-GS, the MRE and NCC for each model are evaluated using Eq. (E.0.3) and (E.0.5) respectively. The MRE and NCC at each z -position and in 3D are computed. The results are displayed in Fig. 4.9 and 4.10.

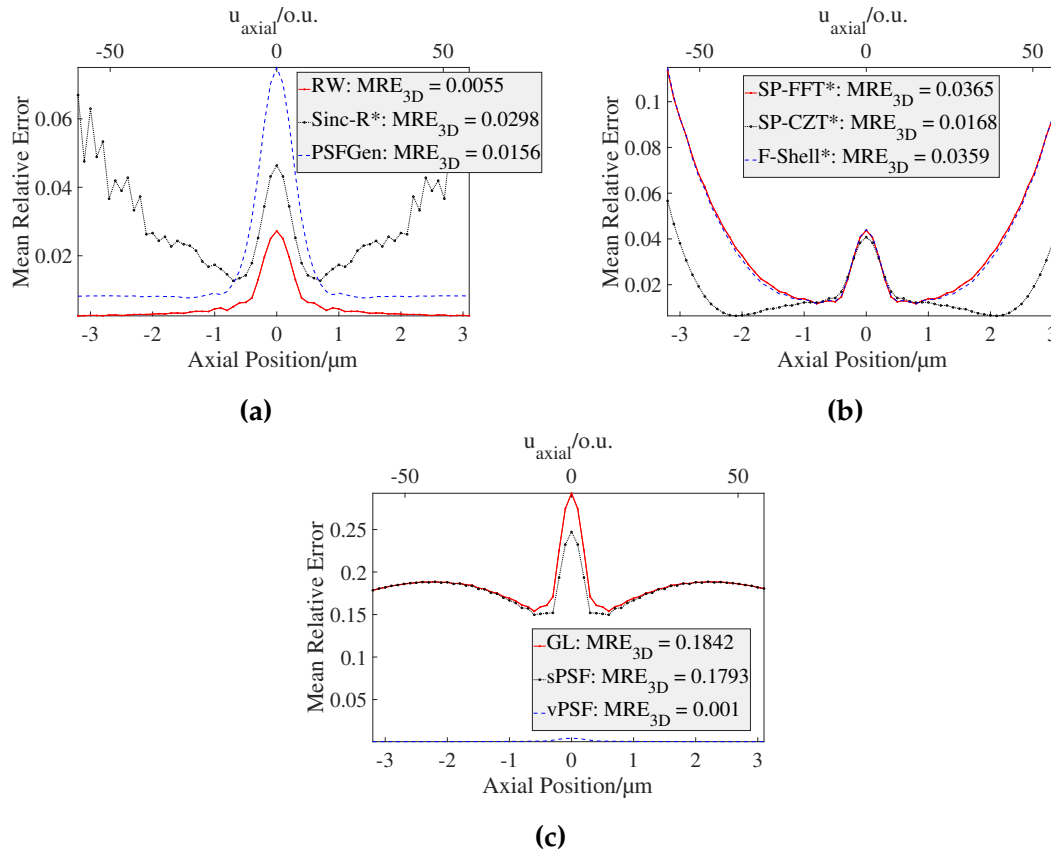


Figure 4.9: Mean relative error between the gold standard RW-GS PSF and PSFs models.

We observed from this investigation that the state-of-the-art vPSF has the least error and highest similarity with the RW-GS. Most of the methods display a peak around the focus position due to the difference in the integrated intensity related to missing cone that was discussed in the previous section. Although the NCC with the RW-GS of the scalar sPSF is at 0.99275 compared to the scalar GL PSF, the MRE errors are more pronounced for those scalar PSFs, 0.1842 for GL and 0.1793. This is due to the limitation of the scalar approximation. The similarities of those scalar PSFs around the focal position are also significant. SP-FFT*, SP-CZT*, F-Shell* and Sinc-R* are similar to the RW-GS with a NCC value higher than 0.99958 compared to a NCC equal to 0.99897 for the PSFGen. In terms of MRE in the intensity however, the SP-CZT* and PSFGen have close MRE values. This is because, the error in the PSFGen is high around the focus but low in out-of-focus while the range of the error in the SP-CZT* is smaller than the PSFGen, yielding to both methods to display a close MRE values. The newly developed methods, SP-FFT*, SP-CZT*, F-Shell* and Sinc-R*, also

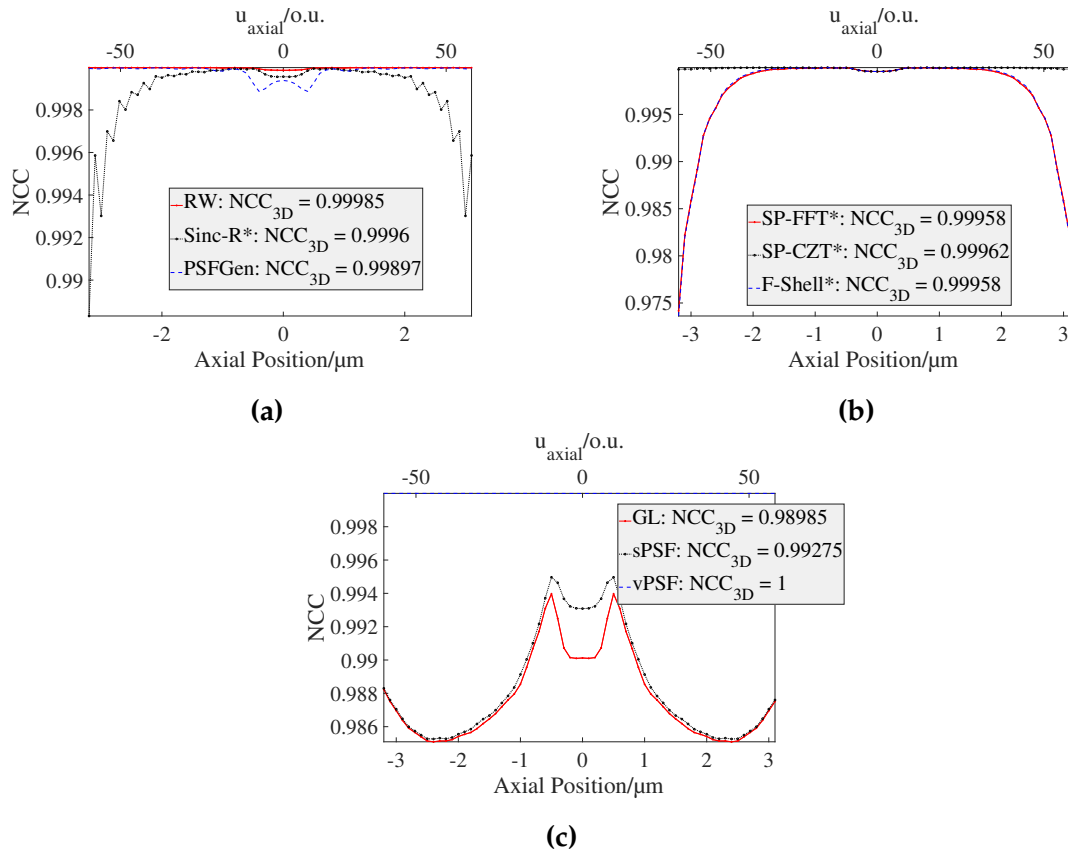


Figure 4.10: Normalized cross correlation between the gold standard PSF and PSFs models.

display higher errors at higher z -position compared to the state-of-the-art PSFs. This can be understood as still a possible presence of small amount of wrap-around in the PSF at higher depth. This wrap-around quantity is discussed in the next section.

4.3.4 Wrap-around effect in the methods

It is known that Fourier transform operation can be decomposed into Fourier series of periodic functions cosine and sine [14]. The Fourier transform (FT) of a signal is also periodic. If the sampling grid is not fine enough for a given desired computation or if the PSF is sampled wrongly and the Nyquist theorem is not satisfied, the FT operation leads to a wrap-around of the waves from the border to the center of the image. The wrapped information is an artefact that needs to be avoided as it approximates the field distribution wrongly. Techniques that do not employ FT do not suffer from this issue. As the models developed under this project are Fourier-based, it is necessary to investigate the wrap-around effect of each model. In our calculation in Chap. 3, we took this into consideration and we presented a way to go around it. As seen from the previous quantification of the errors however, this effect may still not be fully suppressed. To quantify the wrap-around effect, we calculate densely sampled PSFs from each technique using a large calculation window, denoted by W_{ref} and given by the formula in Eq. (5.1.1). This PSF is denoted by h_{ref} . A large amount of

wrap-around effect should be avoided within this large computation grid W_{ref} . In order to quantify the wrap-around effect of each PSF model, we then compute the PSF with different window W and compare it with the h_{ref} with the window W_{ref} . Let us denote this newly computed PSF: h_W . The wrap-around effect in h_W in relative to h_{ref} is calculated in terms of MRE between h_W and h_{ref} within the smaller window of W and W_{ref} . No wrap-around effect is expected in h_W for $W > W_{\text{ref}}$. However, as the window is bigger, the energy is spread over a larger grid. The difference between h and h_{ref} is not expected to be zero but is expected to converge to a constant for all $W > W_{\text{ref}}$.

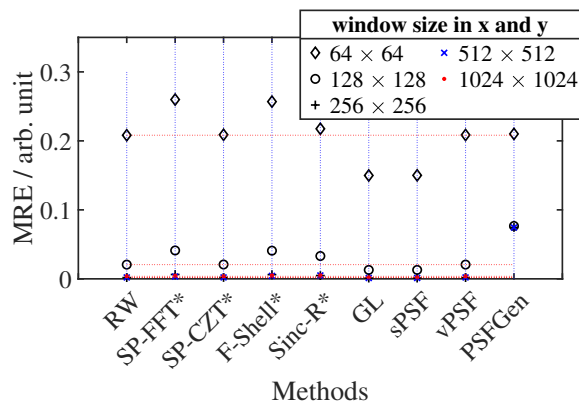


Figure 4.11: Quantification of the wrap-around effect in different window size in x and y . The red dashed horizontal lines are references that represent the lines where the MREs from the RW are calculated at a given window size.

The W_{ref} was calculated to be 326×326 in x and y . We compute different window size in power of 2: 64×64 , 128×128 , 256×256 , 512×512 , and 1024×1024 . The z -range is 64 and the rest of the parameters are the same as described previously in the introduction of Section 4.3. The PSFGen runs out of memory for the last large grid so a quantification of the MRE for this grid was not possible for this method. We observe from Fig. 4.11 that the MRE of the scalar state-of-the-art GL and sPSF PSFs fall far below the red dashed lines from the RW. The methods for computing those PSFs, the vPSF, PSFGen, and RW do not employ any FT operator. The MRE of the SP-CZT* falls on the same line as RW and vPSF in all different windows. The Sinc-R* presents an MRE slightly above the red lines while SP-FFT* and F-Shell* fall at about 0.05 above the red lines. This means the wrap-around effect in the SP-CZT* has been completely suppressed while there is still some that remains in the SP-FFT* and F-Shell* and possibly in the Sinc-R*. The MRE errors converge to a constant as expected for window bigger than the reference window 326×326 .

4.3.5 Speed of the various algorithms

The estimation of the speed of the various algorithms in this section was done under Windows 10 64-bit, Intel(R) Core(TM) i5-3570S CPU @ 3.10GHz, 8,0GB RAM, Intel

HD Graphics. The profiles of the computation time per voxel for each technique at four different window sizes are displayed in Fig. 4.12.

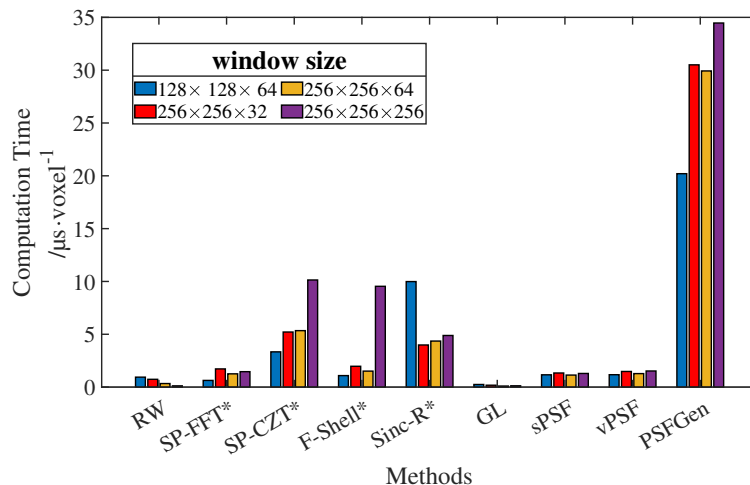


Figure 4.12: Computational time of each technique per voxel in μs .

The RW model evaluate the three integrals in (2.2.26) numerically by exploiting a cylindrical coordinate system for the integration. This numerical integration is computationally advantageous since only the field in the centred radial axis versus the axial position z is calculated. RW therefore employs a radial symmetry in its computation, and has the disadvantage that non-spherical aberrations cannot easily be represented. The accuracy of the RW model is a function of the steps of integration. The 3D SP-FFT* PSF and SP-CZT* PSF are computed slice by slice in z . Using a code profiler under Matlab, we concluded that about 70% of the computational time of the SP-FFT* technique is dominated by the FFT operation. The algorithm complexity of each 2D slice in the SP-FFT* is given by $O(N_x N_y \log(N_x N_y))$. The computational time per voxel therefore remains relatively the same. Larger calculation grid however will require more time to compute.

On the other hand, reflecting on Eq. (3.4.3), the CZT operation requires 3 FFTs to compute. In the SP-CZT* method, a new and bigger window is calculated such that the field at higher depth would not have wrap-around effect issues from the FFT operation. The running time depends on the lateral size and z -depth. This explains the relative higher computational time per voxel in a SP-CZT* compared to SP-FFT*. The Fourier shell method (F-Shell*) computationally depends on the interpolation of the coefficients of k_z at different sub-pixels. By analysing the algorithm with code profiler under MATLAB, this interpolation process takes up about 70% of the total computation cost. If the z -range becomes significantly larger, a large number of coefficients also needs to be interpolated. The computation time therefore mainly depends on the number of iteration and the kernel size. Those coefficients are stored on

the disk of the computer and can be accessed easily without any heavy computation, reducing the computation time of a second run to up to $20\times$.

In the computation of the Sinc-R* PSF, the Fourier wrap around in the calculation of wave propagation is avoided by calculating directly the 3D spectrum of propagating wave to be half of a 3D shell which is derived from the 3D FFT of a propagating sinc wave and projected on the 3D McCutchen pupil which correspond to the in-focus field. Each of the three components of the electric field is on a 3D shell, forming a 4D field. The projection of the 3D sinc shell onto the 3D McCutchen pupil is in 4D. To return the field in the image plane, this 4D field in the pupil plane is 3D Fourier transformed. The only artefact that may still be present in the calculation is from the edge of the grid during this 3D FFT. This can be avoided by damping the edge or extending the window by 25%. The difference in the computation with or without this 25% extension is not significant. It is advisable to consider it in the computation as more information can be preserved by it. In the SincR method, the z -range also needs to be highly sampled leading to an heavy computation, which is not required for all the other propagation methods.

The state-of-the-art GL method discussed here is implemented using Bessel series approximation of the GL method [34] over a single xz slice. A radial asymmetry in the PSF is assumed and a piece-wise linear interpolation is used to compute the whole 3D volume PSF. The model computational time and accuracy are inversely dependent. Both depend on the number of basis in the Bessel series and the sampling number. The computation time of the PSF corresponds to the default number of basis which is equal to 100 Bessel functions and number of coefficient parameters equal to 1000. These make the GL PSF calculation the fastest method.

ScalarPSF and VectorPSF compute the numerical integration of the electric field in the image plane using Simpson's rule [37]. The methods are relatively fast and the computational time per voxel seems to be independent of the z -range. Lastly, the software PSFGen is the most expensive in time and in memory among the PSF models, which we compare to.

4.3.6 Summary and outlook

To summarize, the SP-CZT* method satisfies the most the missing cone problem condition in wide-field microscopy and has enabled the suppression of the Fourier wrap-around effect. These advantages can however come at a high cost in time if a higher depth is required. The state-of-the-art vPSF can still be a faster alternative and has more similarity to the RW-GS than SP-CZT* but it violates more the missing cone condition, which is a physical condition that must be satisfied. F-Shell* and SP-FFT* are affordable methods in times and memory. They are good methods if a computation at higher depth is not required. Sinc-R* is efficient and moderate in balancing the pros

and cons of the PSF in terms of accuracy versus computation time. It is only suitable for calculating a volume PSF.

The scalar GL PSF is the fastest method but is the least accurate among the methods. The techniques used in its computation are attractive to speed up PSF calculation. It however needs to be adapted to account for the vector features of light for it to be usable in representing the PSF of a high NA system.

Although the PSFGen has been widely used in the literature, we observe from this investigation that all the vector PSF models have surpassed this method in different ways.

The state-of-the-art PSFs, RW, sPSF, and vPSF, also use radial symmetry in the computation. This means that they cannot account for non-symmetric aberration. The newly developed methods, SP-FFT*, SP-CZT*, F-Shell* and Sinc-R*, can still be optimized to be faster if radial asymmetry is not required in the computation.

Chapter 5

Phase Retrieval of High NA Point Spread Function Data

Aberrations are common and unavoidable during image acquisition. A suitable phase retrieval algorithm is required to retrieve and correct for aberration in experimental PSF reconstructed on a smaller grid. Here, we describe a newly adapted algorithm for such purposes and demonstrate the efficiency of the algorithm for retrieving phase aberration from simulated PSF data with high NA system.

5.1 Introduction

Aberrations are mostly unavoidable during image acquisition and their cause and amplitude are often unknown. As discussed in Section 3.6.2, any given optical system has a set of parameters for which it was designed for. Any deviation of the values of the constant parameters from the design parameters induces aberrations. Most experimental activities are conducted without the exact knowledge of the experimental parameters such as the thickness, the flatness of the sample and the refractive indexes (RI) of each sample layer and immersion medium. These parameters are also sensitive to the environment under which the experiment is conducted such as the room temperature. The common approach to correct for the induced aberration is to retrieve the phase from the measured PSF and estimate the aberration from the retrieved phase.

Gerchberg and Saxton developed a powerful algorithm for phase retrieval [83]. This algorithm uses the knowledge that imaging can well be described in both real and Fourier space. It consists of going back and forth between both spaces until the phase converges. The Gerchberg-Saxton algorithm however requires the intensity distribution in both spaces, real and Fourier space, to be known [83].

Hanser and al. modified the Gerchberg-Saxton algorithm to account for this lack of knowledge of the intensity distribution in Fourier plane by considering the data from

a focal plane stack. The modified Gerchberg-Saxton algorithm has been proven to be efficient for light microscopy data [84]. This method is however still not suitable for our application. The algorithm presented by Hanser et al. does not account for the small grid on which the measured data is presented and from which the phase is to be retrieved. The reason is explained as follows. An experimental PSF, h_{exp} , is reconstructed by averaging over several beads over a grid $N_x \times N_y \times N_z$ such that only a single bead is contained in the grid. In this way, the signal-to-noise ratio is increased by the square root of the number of conducted measurements. The reconstructed data do no longer need to be pre-processed to reduce the present noise. However, the grid is small for going iteratively back and forth between real and Fourier spaces. A severe wrap-around effect may be induced. As a consequence, zero-padding h_{exp} to obtain a new size $N'_x \times N'_y \times N_z$ is necessary such that the propagation of a field at higher depth z_{max} will still be contained in the grid without wrap-around. We calculate this grid using the following expression:

$$N'_x = 2 \times 2 \times \left(\frac{z_{\text{max}} \frac{k_x|_{\text{max}}}{k_z|_{\text{max}}} + 1.3d_{x|_{\text{lim}}}}{p_x} \right), \quad (5.1.1)$$

with $d_{x|_{\text{lim}}}$ being the resolution limit, p_x the pixel size and 1.3 is an heuristic factor. The first factor 2 in the expression of N'_x is considered to double the half window and the second factor 2 is to sample the frequency space two times higher. The variables z_{max} , p_x and $d_{x|_{\text{lim}}}$ have the same units and N'_x is expressed in pixels. The same amount of padding is done along y -axis.

The zero-padding corresponds to a convolution of the measured PSF with a sinc function in Fourier space and needs to be handled with care. In effect, *here we present a different approach to solve the phase retrieval problem.* The process is presented in Algorithm 7. We modified the method developed by Hanser et al. to fit our problem and approach the vectorial features of high NA microscopic data using the mathematical formulation of the field in the pupil plane described in Algorithm 1. *The algorithm is tested on simulated data of PSF recorded with high NA system and a tilted coverslip in the forward model.*

5.2 Phase retrieval algorithm

An intensity measurement is conducted to record the volume PSF intensity. The convergence of the technique is monitored using the sum of squares error between the estimate of the PSF and the measured PSF.

We denote h'_{exp} as the resulting zero-padded measured PSF. It is initially normalized such that the total integrated intensity is equal to the length of its z -range. This is to facilitate the tracking of energy conservation in both space, real and Fourier spaces. In

experimental work, the property of widefield images which corresponds to the missing cone problem may not be reflected in the recorded images (see Section 3.9), due to a fluctuating brightness and background that may occur during the measurement. For this reason, the experimental PSF is scaled such that the integrated intensity along the optical axis remains the same.

From this point onward, the grid for the phase retrieval is equal to $N'_x \times N'_y \times N_z$. To initialize the phase retrieval, we set the initial guess of the phase Φ to retrieve to be zero. The effective NA, NA_{eff} , is given by the minimum between the known refractive indices and the NA set by the manufacturer: $NA_{\text{eff}} = \min\{NA, n_s, n_i, n_i^*, n_g, n_g^*\}$. This is true as any field within the region $]NA_{\text{eff}}, NA]$ are non-propagating waves leading to total internal reflection. The 3D field distribution in the pupil plane delimited by NA_{eff} is calculated using Eq. 3.3.2 by setting each of the transmission coefficients T_p and T_s to 1, applying the correct aplanatic factor for energy conservation and choosing the correct polarization. If unknown, the polarization is set to be circular by default as this corresponds to the resulting polarization of dipoles oriented in all directions (see Appendix C). The pupil plane is propagated over the z -range corresponding to the measured PSF and Fourier transformed to obtain the corresponding field in the image plane. As only information in real space within the smaller grid $N_x \times N_y \times N_z$ is known, a real space constraint is enforced in the resulting complex amplitude field within this region only. Outside this region, the field is kept as it is to conserve the energy at each z -plane. The real space constraint consists of keeping the phase of the field and changing the amplitude to be the square root of the measured PSF. Then, we return to Fourier space and back propagate the field to obtain the corresponding refocused field. Any extra phase which corresponds to the phase of the initial polarized field in the pupil plane is discarded by multiplying the back propagated field in the pupil plane by the complex conjugate of the initial pupil field.

Summing over the number of z -slices and the three different components of the pupil plane, we obtain a new estimate of the phase Φ_k at the k -th iteration. This corresponds to the argument of the summed pupil plane distribution. The sum of squares error between the estimated PSF and the measured PSF is evaluated at each iteration. This process is repeated until convergence or until the error is less than a pre-defined threshold. The desired phase corresponds to the phase from the pupil distribution at convergence. It is important to note that this retrieved phase does not only represent the phase of the field within the region of interest $N_x \times N_y \times N_z$ but also contains information about the field outside this region.

In this study, we are particularly dealing with PSFs which represents the image of beads whose sizes are smaller than the diffraction limit. Once the size of the bead is bigger than the diffraction limit, we have to account for the convolution of the bead shape with the PSF. This effect is not covered here but can be easily implemented using the approach of Hanser in [84].

Algorithm 7 Phase retrieval**Input:** $N, \epsilon, h_{\text{exp}}, p_z, p_y, p_x, z, \Phi_0, NA, \lambda_{\text{em}}, \tau_d, \tau_r$

- 1: N : number of iterations
- 2: ϵ : threshold error
- 3: h_{exp} : intensity measurement of volume PSF of size $N_x \times N_y \times N_z$
- 4: $[p_z, p_y, p_x]$: voxel size with the same unit as λ_{em}
- 5: z : z -range of propagation of length N_z
- 6: τ_d : regroups the RI in the design conditions $\{n_g^*, n_i^*\}$
- 7: τ_r : regroups the RI in the non-design conditions $\{n_s, n_g, n_i\}$
- 8: Φ_0 : initial guess of the phase to retrieve

Output: $\Phi = \arg\{P_q''\}$

- 9: $[N'_x, N'_y] \leftarrow$ desired grid calculated using Eq. 5.1.1
- 10: $h'_{\text{exp}} \leftarrow$ zero-pad of h_{exp} to a size $N'_x \times N'_y \times N_z$
- 11: $NA_{\text{eff}} \leftarrow \min\{NA, n_s, n_i, n_i^*, n_g, n_g^*\}$
- 12: $\vec{E}_k(k_x, k_y, k_z) \leftarrow$ field on the pupil plane calculated with $NA_{\text{eff}}, \lambda_{\text{em}}, \tau_d, \tau_r$, and each component of 2D size equal to $N'_x \times N'_y$
- 13: **for** $q = 0 : 1 : N - 1$ **do**
- 14: $\vec{P}_q = \vec{E}_k \cdot e^{i\Phi_{q-1}}$
- 15: $\vec{h}_{\text{amp},q} \leftarrow \text{FFT}^{-1}(\vec{P}_q \cdot e^{-ik_z z})$ \triangleright Field propagation
- 16: $h_q \leftarrow |\vec{h}_{\text{amp},q}|^2$
- 17: $\vec{h}'_{\text{amp},q} \leftarrow \vec{h}_{\text{amp},q} \times \sqrt{h'_{\text{exp}}/h_q}$ \triangleright Real space constraint only within the smaller grid $N_x \times N_y \times N_z$
- 18: $\text{error} \leftarrow \sum_{xyz} (h_q - h'_{\text{exp}})^2$ \triangleright MSE within the smaller grid $N_x \times N_y \times N_z$
- 19: **if** $\text{error} > \epsilon$ **then**
- 20: $\vec{P}'_q \leftarrow \text{FFT}(\vec{h}'_{\text{amp},q}) \cdot e^{ik_z z}$ \triangleright Back propagation
- 21: $P''_q \leftarrow \sum_{N_k} \sum_{N_z} \vec{P}'_q \cdot \vec{E}_k^*$, N_k being the three components of \vec{E}_k \triangleright Summation
- 22: $\Phi_q \leftarrow \arg\{P''_q\}$ \triangleright Retrieved phase
- 23: **else**
- 24: **break**
- 25: **end if**
- 26: **end for**

5.3 Phase retrieval algorithm for a high NA PSF data

We evaluate the phase recovery algorithm on simulated data. Such analysis is necessary to estimate and predict the precision under which the phase retrieval in the experimental validation in Chap. 6 is conducted.

5.3.1 Forward model

We calculate the forward PSF model using the properties of an objective lens Plan-Apochromat Oil HI DIC Corr M27 100x/1.57 [Zeiss: 420792-9771-000]. This objective lens truly represents a high NA system. The emitter is assumed to be embedded in ProLong Gold of RI equal to $n_s = 1.46$ and is placed at $30 \mu\text{m}$ from the surface of the coverslip. The emission wavelength is set to be equal to 525 nm . The coverslip and immersion medium are assumed to meet the design condition and are of respective RI $n_g = 1.518$ and $n_i = 1.66$. We choose a grid of size equal to $512 \times 512 \times 90$ pixels to avoid as much as Fourier wrap-around as possible. Due to the focal shift induced by the RI mismatch, hence the spherical aberration, the forward PSF might go out of the allowed z -range of the grid. An additional defocus aberration of Zernike order [2 0] is added to shift the PSF axially to correct for the focal shift. The corresponding focal shift associated with the (t_s, n_s) values is calculated to be -358.27 pixels using Eq. (4.2.1). The peak value of the defocus aberration, Z_2^0 , or Zernike coefficient that needs to be considered is calculated to be $C_2^0 = 3.8546$. This coefficient is calculated using the formulation of Mahajan in Eq. (1-3d) of [85]:

$$C_2^0 = -\frac{\text{FS}}{8F^2} \text{ with } F = \frac{r_G - \text{FS}}{2r_p} \text{ being the focal ratio,} \quad (5.3.1)$$

and $r_G = n_i r_p / \text{NA}$ being the radius of curvature of the Gaussian sphere, r_p the pupil radius, and FS, denoting the focal shift, represents the longitudinal defocus. To add more level of complexity into the system, we add a coma aberration Z_3^1 of order [3 1] and peak value equal to π .

The voxel size is $40.625 \times 40.625 \times 65 \text{ nm}^3$. We choose the ‘‘SP-FFT’’ method described in Algorithm 1 to simulate the forward PSF. The polarization state is assumed to be circular. The resulting PSF is cropped to a lateral size of 64×64 . The exact position of the focal position is difficult to guess from the experimental PSF data. We therefore axially shift again the cropped forward model such that the maximal intensity is at the centre position of the grid. This is to imitate the practice we have adopted for experimental PSF before we retrieve the phase. At this point, the forward PSF is subsampled twice in z to reduce the computation cost. We denote h_0 the resulting forward PSF. Its size is reduced to $64 \times 64 \times 31$ and its voxel size is $40.625 \times 40.625 \times 130 \text{ nm}^3$. The phase of the electric field associated with h_0 is displayed in Fig. 5.1 with title Φ of h_0 . The PSF h_0 is scaled such that the maximum number of photons is 1000. This value is chosen arbitrary to imitate an experimental event.

5.3.2 Backward models

We test the Algorithm 7 with two different grids: 1) same size as the forward model h_0 : $64 \times 64 \times 31$, and 2) a zero-padded grid of size $512 \times 512 \times 31$. As a first guess of the phase, we provide to the algorithm a phase distribution with spherical aberration generated from $(t_s, n_s) = (5 \mu\text{m}, 1.46)$ and defocus aberration associated to the focal shift under these two parameters. In those two investigations, we assume a noise-free image. We run the phase retrieval with 200 iterations. The phase retrieved using the lateral grid 64×64 and 512×512 are displayed in Fig. 5.1 with the title Φ of $h_{(64)}$ and Φ of $h_{(512)}$ respectively. The PSFs with these respective phases are denoted by $h_{(64)}$ and $h_{(512)}$. To observe the efficiency of the algorithm in the presence of noise, we add a Poisson noise to the forward model h_0 . This noisy model is denoted by h_0^{noisy} . We retrieve the phase from h_0^{noisy} using the lateral grid of size 512×512 and the resulting PSF with the retrieved phase is displayed in Fig. 5.1 under the name $h_{(512)}^{\text{noisy}}$.

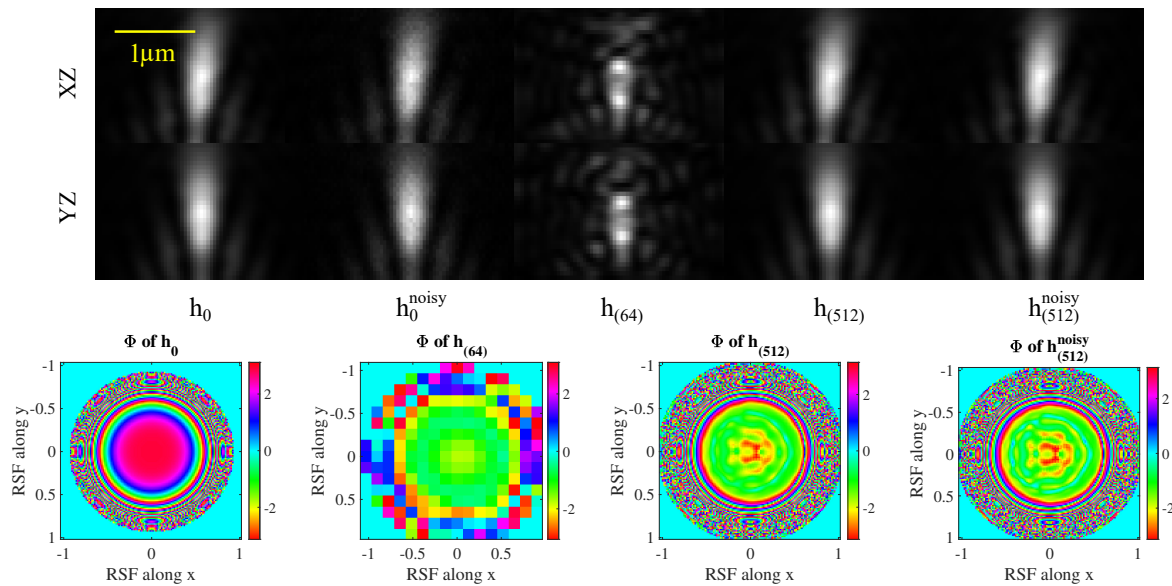


Figure 5.1: Test of the accuracy of the phase retrieval algorithm using simulated data. First row: xz -profiles sections of the forward model h_0 with coma, defocus and spherical aberrations, the forward model with Poisson noise, the PSF $h_{(64)}$ with the phase reconstructed from h_0 using a lateral grid of 64×64 , the PSF $h_{(512)}$ with the phase reconstructed from h_0 using a lateral grid of 512×512 , and the PSF $h_{(512)}^{\text{noisy}}$ with the phase reconstructed from the noisy h_0^{noisy} using a lateral grid of 512×512 . Second row: yz -profiles sections. Third row: Phase aberrations of the electric fields which correspond to $h_0, h_{(64)}, h_{(512)}$, and $h_{(512)}^{\text{noisy}}$ respectively (from left to right).

The NCC between the ground truth h_0 and $h_{(64)}$ is equal to 0.8127 while the NCC between $h_{(512)}$ with h_0 equals to 0.9997. In the presence of Poisson noise in the forward model, the NCC between $h_{(512)}^{\text{noisy}}$ with h_0 is reduced by 0.32% to 0.9965. The Algorithm 7 is therefore capable of retrieving the phase from a PSF with smaller grid with a NCC to ground truth of at most 0.9997 or 0.9965 in presence of noise.

Chapter 6

Experimental Validation

A conclusive experimental validation of the Point Spread Function (PSF) models under different imaging condition is conducted in this chapter. The experimental ground truth is obtained by averaging the images of several beads. The normalized cross correlation between the experimental reconstructed PSF and simulation is chosen as a metric to demonstrate the ability of each of our PSF models to represent real experiments. The PSFs models are also validated in their efficiency, ability, and accuracy for image reconstruction.

6.1 Experimental validation workflow pipeline

To conduct *an effective experimental validation of our PSFs models*, an workflow pipeline needs to be well established. The ground truth PSF, denoted by Exp-PSF, of the validation is formed by averaging over the images of several beads with physical size smaller than the diffraction limit of the optical system. Each different setting of image acquisition and parameters correspond to a ground truth.

At each stage of the experimental validation, an error may be induced. Firstly, an error may occur in the acquisition of the experimental PSF itself, yielding to a wrong assumption of a supposed to be “ground truth”. If the sample is not prepared with care, some fluorescent or dirt background may add up to the signals during the imaging. The imaging parameters, such as refractive index or/and emission wavelength, may also be estimated wrongly due to its dependence to the condition of the working environment.

Secondly, the PSF is modelled under a given imaging condition invariant. This has been discussed as the Abbe sine condition (see Section 2.1.2) yielding to the adoption of an aplanatic correction in the calculation (see Section 2.1.3). This is a physical condition that the system needs to satisfy and is taken into consideration in the PSF calculation. An error in the quantification and assumption of this aplanatic factor leads to a major error in the investigation of the validity of the PSF.

Thirdly, the quality of the Exp-PSF construction, hence the error, depends on the localization precision of each bead and the number of beads that are averaged. The localization precision is function of the number of photons emitted by the bead emitter while the number of beads influence the amount of noise in the reconstruction. Averaging over several beads reduces the noise present in the measured PSFs. The averaging can however suppress some non-symmetrical aberration yielding to a wrong estimation of the aberration in the imaging system. It is important to choose measured PSF data which is least affected by field-dependent aberration as averaging over beads in the presence of these types of aberration yield a large error in the assumption of the ground truth Exp-PSF itself.

Fourthly, since the exact values of the constants imaging parameters such as refractive index and sample thickness are unknowns or can be estimated wrongly, the aberration contained in an Exp-PSF is retrieved computationally. The retrieved phase is introduced in the simulated PSF models to enable a meaningful and realistic comparison of the experimental and simulated data. An error in the phase retrieval algorithm is therefore a plausible error that may also occur during the process of experimental validation.

In summary, the accuracy of a simulated PSF data to represent the true PSF of a given optical system is valid under the conditions that are previously mentioned. The total and final error includes the error in the simulated PSF data itself, and the errors in the assumptions of the ground truth, measured Exp-PSF.

Lastly, *the simulated PSFs are used for deconvolving experimental images of spherical beads with known diameter and C. Elegans embryo to test their efficiency, ability, and accuracy for image reconstruction.* This section concludes the experimental validation of the PSF.

The workflow of the experimental validation of the PSF is therefore summarized in six different stages:

- Stage 1:** Sample preparation and image acquisition
- Stage 2:** Validation of the imaging condition invariant
- Stage 3:** Image processing and Exp-PSF construction
- Stage 4:** Phase estimation from Exp-PSF
- Stage 5:** Comparison of Exp-PSF with simulated PSFs
- Stage 6:** PSFs for image reconstruction

6.2 Materials and method for PSF measurement

6.2.1 Fluorescent emitter

Three parameters of a fluorescent emitter need to be considered when choosing the most suitable emitter for PSF measurement:

- The brightness plays a role in the localization precision of the particles. The localization precision is a function of the number of emitted photons [86].
- The photostability determines the bleaching and blinking properties of the emitters. A photostable emission is required for an effective measurement [1].
- The size of the particle is related to the resolution of the imaging. Particles with size smaller than the resolution limit should be used. If the particle size is bigger than the diffraction limit, the obtained image does no longer represent the PSF of the system, but rather the convolution of the PSF with the particle emission distribution [3, 14].

The fluorescent emitter used in this project satisfies those three conditions and can be used as subresolution fluorescent source for measuring the PSF. It consists of 0.1 μm TetraSpeckTM [ThermoFisher: T7279] and 0.2 μm FluoSpheres Carboxylate-Modified [ThermoFisher: F-8811] microspheres. TetraSpeck microspheres are composed of four fluorescent dyes with well-separated excitation/emission peaks $\lambda_{\text{ex}}/\lambda_{\text{em}}$: 360/430 nm (Blue), 505/515 nm (Green), 560/580 nm (Orange), 660/680 nm (Dark Red) while FluoSpheres are with one channel 505/515 nm only.

6.2.2 Sample preparation

6.2.2.1 FluoSphere bead sample

To prepare this sample, a Zeiss cover glass of high performance with a thickness of 0.17 mm \pm 0.005 mm is used [Carl Zeiss: 474030-9000-000]. The coverslip is left in Poly-L-Lysine for about 10 min to enhance the electrostatic interactions between the coverslip and carboxylate beads. The coverslip is afterward washed with deionized water and dried off. A solution of beads with the desired concentration is placed on the coverslip and air dried. A small amount of ProLong Gold mounting media is placed on top of the sample and left to cure. The refractive index (RI) of the ProLong Gold was measured to be 1.46 at room temperature. The samples and images were prepared and taken by Maximilian Senftleben from the group of Prof. Dr. Sara Abrahamsson, Baskin School of Engineering, University of California, USA (SaraLab).

6.2.2.2 TetraSpeck bead sample

The preparation of the sample and acquisition of the images from the TetraSpeck bead solution were achieved within our research group, group of Prof. Dr. Rainer Heintzmann, Friedrich Schiller University Jena, Germany (HeintzmannLab) and the Central Analytical Facilities, Physiology laboratory, Stellenbosch University, South Africa. Several measurement were carried out to obtain the best result with the least experimental error.

To prepare the TetraSpeck bead solution, a #1.5 coverslip and microscope slides are firstly deep cleaned to remove any impurities and film of grease that may degrade the quality of the sample and induce error in the measurements. The adopted cleaning procedure is with sodium hydroxide base and it is described in Appendix D. Next, we prepare a 10^5 dilution of TetraSpeck bead solution (see Appendix D.0.2). The solution is vortexed for a few minutes to avoid any clusters. $15\ \mu\text{L}$ of the solution is spin-coated onto the coverslip. The sample is let to set for about 10 min to fully dry. Next, we place a small drop of Dako mounting medium onto a microscope slide. Then, we place the coverslip at an angle 45° , sample facing the surface of the microscope slide, and let it drop slowly on the mounting medium by allowing the medium to spread evenly over the bead. The top surface of the coverslip is lightly pressed to remove any trapped air. We seal the edge with thin layer of colourless nail polish. The Dako mounting medium is colorless and suitable for fluorescent samples and for in vitro diagnostic use [Agilent: Code S3023]. Its RI is measured to be equal to 1.3744 in liquid state at room temperature equal to 18.3° , and humidity 48%. A calibrated Abbe refractometer [PCE: ABBE-REF1] is used to measure the RI at the working temperature. The sensitivity error of the measurement is 0.002. The Dako dries within several minutes, but we let it set for about 2 h before use to ensure the sample and the nail polish completely solidify. Another alternative to prepare the sample is to spin-coat the mounting medium on top of the spin-coated bead. This method is quick and enables us to obtain a relatively flat surface with less possibility of having bubbles. However, a special care needs to be taken. The reason is explained as follows. Although the sample surface is relatively flat, it may not be placed at the center of the coverslip. When placing the sample onto a microscope slide a tilt in the coverslip may therefore be induced due to the position and the thickness of the sample. This could yield to non-spherical aberrations. The sample may be reused twice or three times depending on the laser power applied on it and the sample conservation.

6.3 Factor for energy conservation

Before comparing the simulated PSFs models with an Exp-PSF, we firstly need to investigate the validity of the energy conservation factor related to the aplanatic factor discussed in Section 2.1.3.

To achieve this, we set up a system which enables the measurement of the back focal plane (BFP) of the system. A fluorescent plane and uniform sample is required. In this experiment, we use a thin slice of a chroma slide [Chroma Technology Corporation: autofluorescent plastic slide, part No 92001]. We slice a chroma slide to 70 nm thick layer using a microtome. This thickness falls below the axial resolution ($800\ \text{nm}$) and is the thinnest thickness that we could get without damaging the sample.

The BFP is re-imaged with a system composed of a converging lens of 50 mm focal length coupled with a Basler camera [acA4024-29um] placed at the position of the eyepiece at the observation tube of the microscope [Zeiss Axio Observer, Objective Plan-Apochromat $63\times/1.4$ Oil DIC M27] (see Fig. 6.1). The Basler camera is placed at the focal position after the lens. An x-cite lamp is used as illumination light source. The theoretical magnification of the pupil plane re-imaging system is unknown due to the missing detailed information of each optical component inside the microscope observation unit. It is estimated to be the ratio of the measured over the theoretical pupil radius, and is equal to 0.446. Using the knowledge of the objective lens and the pupil plane re-imaging system, the pupil is calculated to be 4.816 mm in diameter, which is represented by 1160 pixels on the detector. The measured BFP, on the other hand, is found to be with pixel size of $4.158\ \mu\text{m}$.

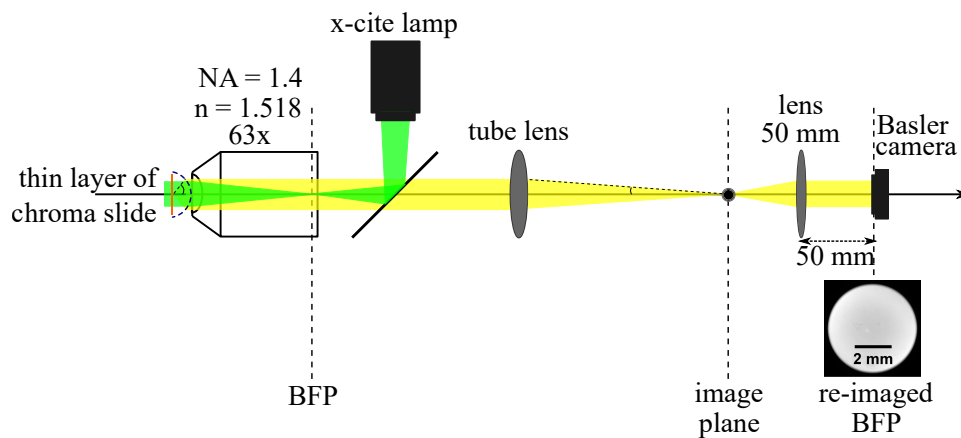


Figure 6.1: Back focal plane re-imaging system

Our model does not account for the effect of any form of supercritical angle fluorescence (SAF). This affects the pupil plane distribution and can completely change the expected measured PSF if not corrected appropriately. Any SAF taking place during the measurement has to be avoided. This is ensured by firstly avoiding any possible back reflection that may reflect SAF into the system. To ensure this, we embed the thin layer of chroma slide in the same oil as our immersion oil with refractive index of 1.518. The BFP re-imaging system is covered with long tube to avoid any background light coming in the Basler camera. The optics is ensured to be properly aligned such that the objective lens only collects fluorescence emission within the critical angle. We calculate the field in the BFP at emission wavelength equal to 580 nm using Algorithm 1, step 1 to 3, accounting for different values of η parameter such that $AF_{amp} = \sqrt{\cos^\eta(\theta)}$. The computation is done such that the pupil size matches the size in the experiment. We also compute a BFP model taking into account the transmission coefficient (TC) of the different interfaces in the object plane. The exact RI of the chroma sample is unknown at the working temperature during the image acquisition, but is known to be less than the refractive index of oil and is said to be about

1.45 at room temperature [87]. The RI mismatch in the sample and the immersion medium influences and reduces the transmission coefficient (see Eq. (2.2.28)), hence the drop in intensity in the BFP at larger angular aperture θ . We therefore assume a lower value of the RI of the sample, equal to $n_s = 1.4$, in our simulation to observe the effect.

The radial mean profile of each of the BFPs intensities, normalized by the intensity at 0 angle of incidence, are displayed in Fig. 6.2f.

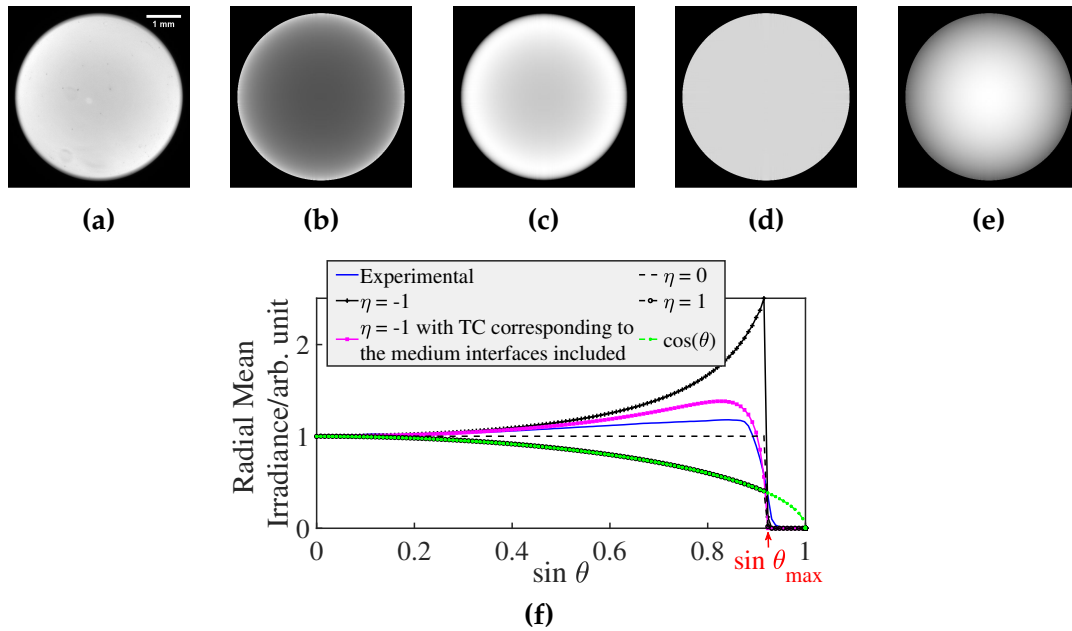


Figure 6.2: Measurement of the BFP for validating the energy conservation factor. (a) A cropped image of the measured BFP intensity from the measurement of a 70 nm thin layer of fluorescent chroma slide. The corresponding theoretical BFP with different factor $\sqrt{\cos^\eta(\theta)}$: (b) $\eta = -1$, (c) $\eta = -1$ and consideration of the transmission coefficients (TC) from a stratified medium composed of a sample of RI $n_s = 1.4$ placed at the surface of the coverslip of RI $n_g = 1.518$ and thickness $t_g = 0.17$ mm, oil immersion of RI $n_i = 1.518$ and thickness t_i assumed to be the same as the working distance of the system equal to 0.15 mm. (d) $\eta = 0$ and (e) $\eta = 1$. (f) Radial mean of the normalized BFP intensities.

The radial profiles of each of the BFP models are plotted in Fig. 6.2f. It is observed from this figure and Fig. 6.2b that the curve of the BFP which corresponds to an emission PSF with $\eta = -1$, i.e. the intensity scaled by $\cos^{-1}(\theta)$, is rising with the elevation angle θ . The intensity profile which corresponds to the experimental BFP is also rising with θ , but not as much as the theoretical emission BFP. By observing the profiles of the intensity in the BFP where we consider the TC of the medium interfaces in the calculation in addition to the η value being -1 (see Fig. 6.2c), we observed a significant drop in intensity in comparison to what we observe in Fig. 6.2b. At larger angles, the intensities of those three data are denser. This demonstrates the aplanatism effect. High angular amplitudes in the BFP get enhanced rather than suppressed.

The still discrepancy between Fig. 6.2c and the experimental BFP in Fig. 6.2f can be explained by the photoselection of preferably in-plane transition-dipoles which leads to a less pronounced emission along E_z components and thus less pronounced higher angles. The experiments should be repeated with a thin volume of freely rotating dipoles with a rotational correlation time far below the fluorescence lifetime. A further effect could be due to unfavourable reflection coefficients at higher angles effectively dimming the light at high angles. It is also worth mentioning that the spectrum of fluorescence emission from the thin slab of fluorescent plastic is a band rather than a single wavelength [1]. Based on the result from this experiment and those observations, we conclude the validity of the aplanatic factor $\sqrt{\cos^{-1}(\theta)}$.

6.4 PSFs under different imaging conditions

To now experimentally validate our PSF models, we consider different image acquisition conditions. Firstly, the resolution is proportional to the emission wavelength and inversely proportional to the NA . Hence, varying one of those two parameters would suffice. We compare Exp-PSFs acquired at different high NA systems with corresponding simulated PSF data (Section 6.4.1). Secondly, the amplitude of the spherical aberration in a given system is function of the refractive index and the thickness of the medium. As seen in the previous chapter (see Chap. 4), the PSF is much more sensitive to the refractive index mismatch. However getting a precise knowledge of the refractive index of each medium is not straightforward due to the image acquisition environment. In addition, the exact thickness of the sample medium is unknown and needs to be determined experimentally. In effect, we chose to alter the optical path difference of the fluorescence emission by varying a known and precise value parameter which is the coverslip correction collar setting on the objective. This is to reduce the errors in the experimental validation. This process enables us to examine the effect of increasing and decreasing spherical aberrations onto the PSF. This second measurement is done with the same NA .

As we do not have a direct access to the fields in the pupil plane nor the amplitude PSFs of the state-of-the-art PSFs, we only compare the PSFs that are developed under this project to present a fair comparison. An exception is made for the RW model. We have knowledge of the corresponding amplitude PSF, but not to the pupil plane. We therefore inverse FFT the RW model to go to the pupil plane. This practice may induce Fourier wrap-around error that is originally not in the RW PSF model.

6.4.1 High Numerical Aperture Imaging

Three different high NA imaging systems with objective lenses (OL) of $NA = 1.3$ [Olympus: UPLSAPO60XS2], 1.4 [Zeiss: Plan-Apochromat 420782-9900-799], and 1.57

[Zeiss: Plan-Apochromat 420792-9771-000] from SaraLab and HeintzmannLab are used. The OL are used with commercial Zeiss Axio Observer 7 microscope stand, and a Hamamatsu Orca Flash 4.0 v3 camera with a $6.5\ \mu\text{m}$ pixel size. A Zeiss Optovar of a magnification equal to 1.6 is used for the systems with $NA = 1.3$ and 1.4. The Olympus objective is used with a Zeiss tube lens of focal length equal to 165 mm instead of being coupled with an Olympus tube lens of focal length equal to 180 mm. This induces a factor of 165/180 in the total magnification. The pixel size in x and y of the recorded PSF is therefore calculated to be $6.5/M\ \mu\text{m}$, M being the total lateral magnification. The optical system is assumed to meet the design condition, except for the properties of the sample.

The Exp-PSF is constructed by averaging over the images of several FluoSpheres beads. The phase aberration present in the Exp-PSF is retrieved using Algorithm 7 described in Section 5. We use as a first guess parameter of the phase aberration the spherical aberration from the sample of RI equal to 1.46 and thickness equal to $1\ \mu\text{m}$. As discussed in Section 4.2.1.3 and 5.3, this aberration induces a focal shift (FS) in the PSF. We therefore add a defocus aberration with Zernike coefficient C_2^0 into our first guess to compensate for this shift. This way, the signal of the generated PSF will be contained within the working z -range. The formulas given in Eq. (4.2.1) and Eq. 5.3.1 are used to calculate the focal shift and peak defocus aberration respectively. The Exp-PSF from the system with $NA = 1.4$ appears to contain more coma aberration. We therefore add a coma aberration of radial and azimuthal order [3 1] and coefficient $C_3^1 = 1$ into the first guess of the phase which corresponds to this system. The guess of the phase aberration helps the algorithm to quickly converge. The effective NA for the phase recovery is given by $NA_{\text{eff}} = \min\{NA, n_i, n_s, n_g, n_i^*, n_g^*\}$.

The image parameters (NA and n_i), the information about the constructed Exp-PSF (pixel size, pixel pitch, number of averaged beads N_{beads}° , exposure time ET for the image acquisition), and guess parameters for the phase aberration (n_s, t_s, C_2^0 and C_3^1) are summarized in Table 6.1.

Table 6.1: Parameters corresponding to the data acquired with high NA imaging

System		Information about Exp-PSF				Guess parameters				
NA	n_i	Size/pix	Pixel size/ nm^3	N_{beads}°	ET/ms	n_s	$t_s/\mu\text{m}$	$t_g^*/\mu\text{m}$	C_2^0	C_3^1
1.3	1.4	[80 80 31]	[73.86 73.86 204]	42	80	1.46	1	161.5	-4.675	0
1.4	1.518	[50 50 33]	[64.48 64.48 65]	9	100	1.46	1	170	2.2642	1
1.57	1.66	[80 80 28]	[65 65 195]	11	150	1.46	1	136	2.2116	0

The retrieved phase from each Exp-PSF is added into the theoretical RW, SP-PSF*, SP-CZT*, F-Shell* and Sinc-R* calculated withing a grid of 512×512 in x and y and at a single emission wavelength 525 nm. The theoretical PSFs are afterwards cropped to match the size of the Exp-PSF given in Table 6.1. Each PSF is normalized by the integrated intensity. The MRE and NCC between aberrant simulated PSFs and the corresponding Exp-PSF are calculated. The results are displayed in Fig. 6.3 alongside

with the initial guess of the phase and the retrieved phase which corresponds to each system (first row: $NA = 1.3$, second row: $NA = 1.4$, and third row: $NA = 1.57$). We also compare the MRE and NCC of the simulated aberrant PSF formed by the light emission within the spectrum band $[498, 551]$ using Eq. (4.2.2) with the Exp-PSF. The same principle and same dataset which correspond to the emission band described in Section 4.2.3 are used for calculating these incoherent effective PSF.

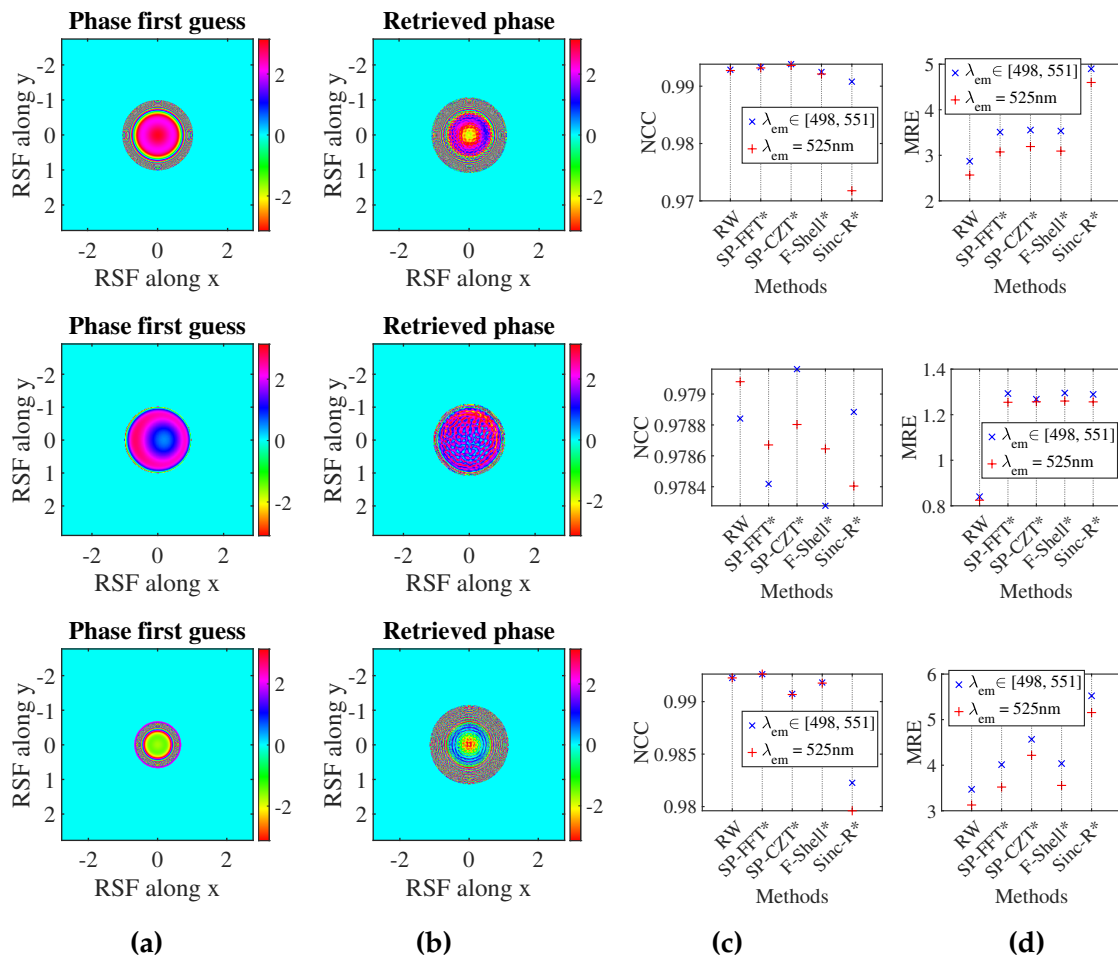


Figure 6.3: Phases of Exp-PSFs recorded with high NA objectives, and NCC and MRE between measured and simulated PSF data. (a) First guess and (b) retrieved phase. (c) NCC, and (d) MRE between Exp-PSF and simulated aberrant PSFs with the retrieved phase in (b). (RSF stands for relative spatial frequency, which is normalized by the lateral cut-off frequency.) First row: $NA = 1.3$, Second row: $NA = 1.4$, Third row: $NA = 1.57$.

The xy -profiles of aberrant PSFs at three different z -planes (top, middle and bottom) and the yz -profiles at $x = 0$ are displayed in Fig. 6.4, 6.5, and 6.6 for $NA = 1.3, 1.4$, and 1.57 respectively. The radial profiles of the intensity at $Z_2 = 0$ and the axial profiles of the intensity are displayed within these figures. The intensities for these latter displays profiles are normalized by the intensity at the zero position in xyz to ease the observation of their differences. We also display the intensity of the PSFs from a

spectrum band as previously described with the PSFs from a single center emission wavelength 525 nm.

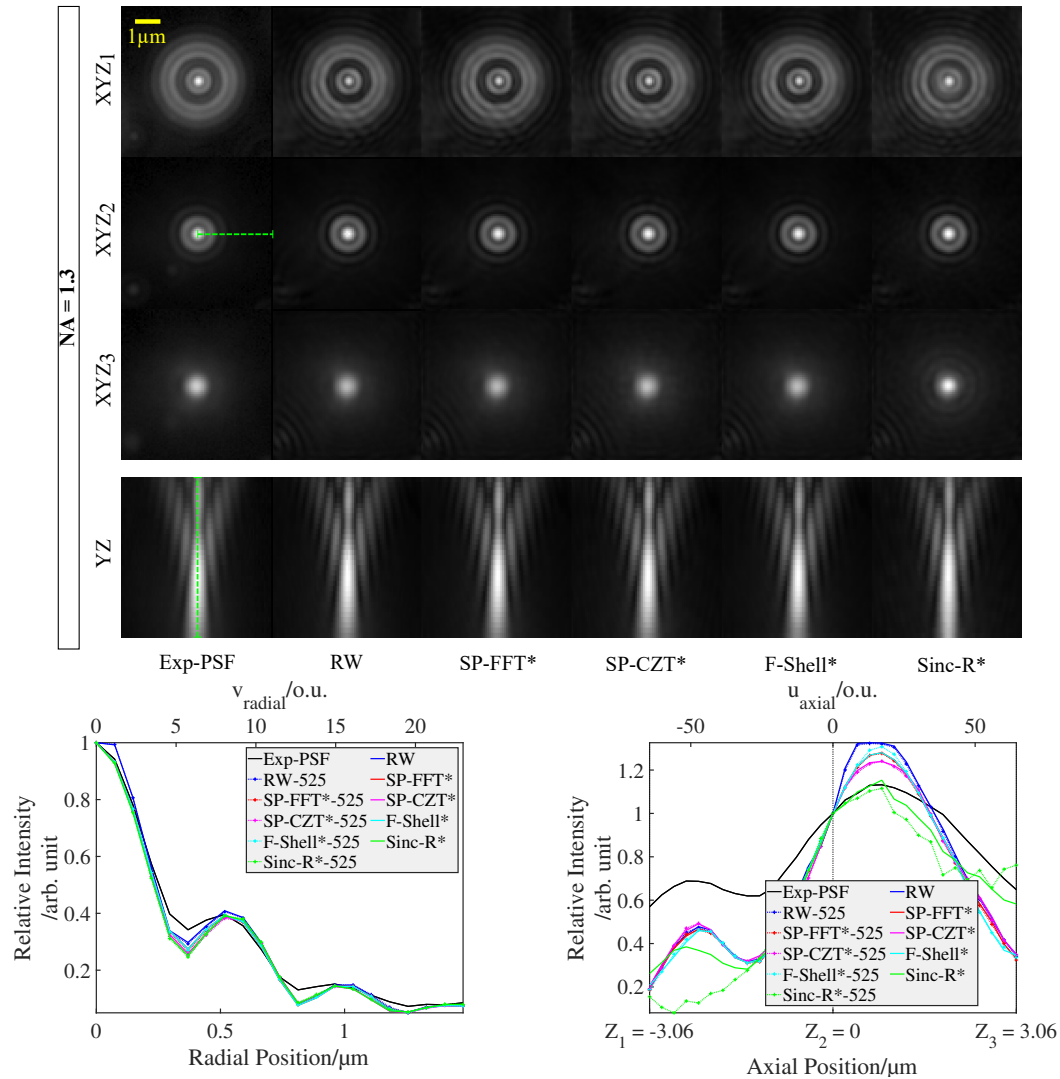


Figure 6.4: Display at $\gamma = 0.5$ of the xy -profiles sections at three different z -plane and yz -profiles at $x = 0$ of high NA Exp-PSF, $NA = 1.3$, and the corresponding simulated aberrant PSFs calculated from different methods: RW, SP-FFT*, SP-CZT*, F-Shell*, and Sinc-R*. ‘PSF’-525 represents the profile of the specific ‘PSF’ at a single wavelength 525 nm. The legend without 525 on its name represents the corresponding PSF derived from the incoherent sum of PSFs within a spectrum band. The relative intensity profiles along the green lines for each of the PSFs at Z_2 and along the axial axis are respectively are displayed at the bottom.

Contrary to the values of the MRE, the NCC values with the PSFs at a single emission wavelength and the NCC values with the PSFs resulting from an emission band are approximately equal (see Fig. Fig. 6.3c). This difference in MRE is due to the incoherent summation and lack of knowledge of the emission spectrum of the sample and the transmission coefficients of the filters. While the NCC tracks the similarity in the shape of the results, the MRE displays the relative errors in intensity. The intensity profiles of the simulated PSFs are also slightly off from the measured Exp-PSF (see

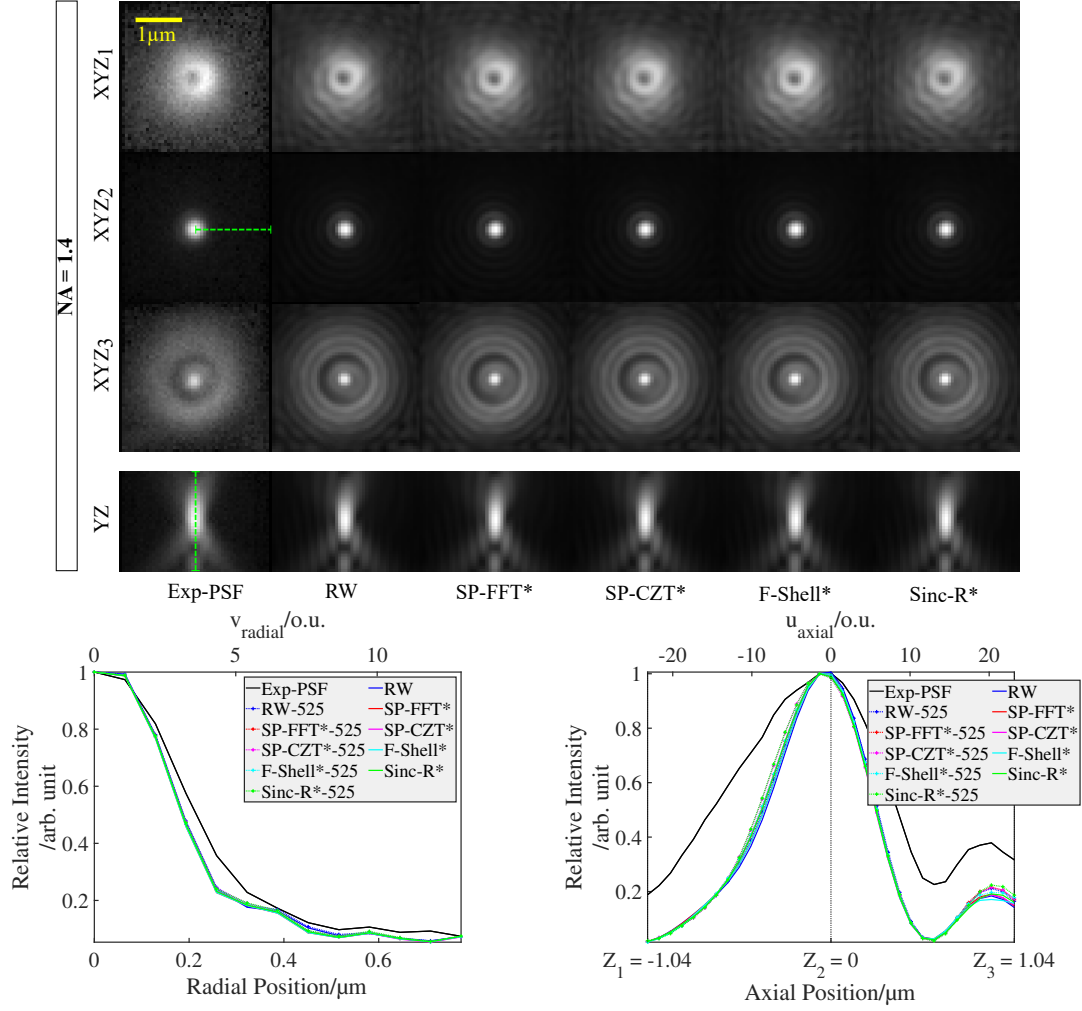


Figure 6.5: Display at $\gamma = 0.5$ of the xy -profiles sections at three different z -planes and yz -profiles at $x = 0$ of high NA Exp-PSF, $NA = 1.4$ and the corresponding simulated aberrant PSFs calculated from different methods. The legend of the figure follows the same trend as in Fig. 6.4.

Fig. 6.4, 6.6 and 6.5) in terms of the amplitudes. However, we observe a consistent trend in the variation of the intensity with spatial position.

The NCC values from $NA = 1.4$ is lower compared to the NCC from $NA = 1.3$ and 1.57 . We believe the reason this is because the Exp-PSF for $NA = 1.4$ contains more noise than the the Exp-PSF for $NA = 1.3$ and 1.57 (see Fig. 6.5). As a result, the MRE is lower for this dataset but the finer features that can be detected and quantified by the NCC values are less similar with the Exp-PSF.

The SP-FFT* has more advantage compared to the other methods as the phase retrieval algorithm is based on this method. However for $NA = 1.3$ and 1.4 , the SP-CZT* has still shown to perform better than the rest of the methods. The F-Shell* displays a very high similarity to the SP-FFT*. The Sinc-R* method is found to be the least accurate among the techniques discussed here. We understand this as due to a possible non-uniformity of the field in the sinc shell.

Overall, we observe that each computation method yields a PSF which is similar to

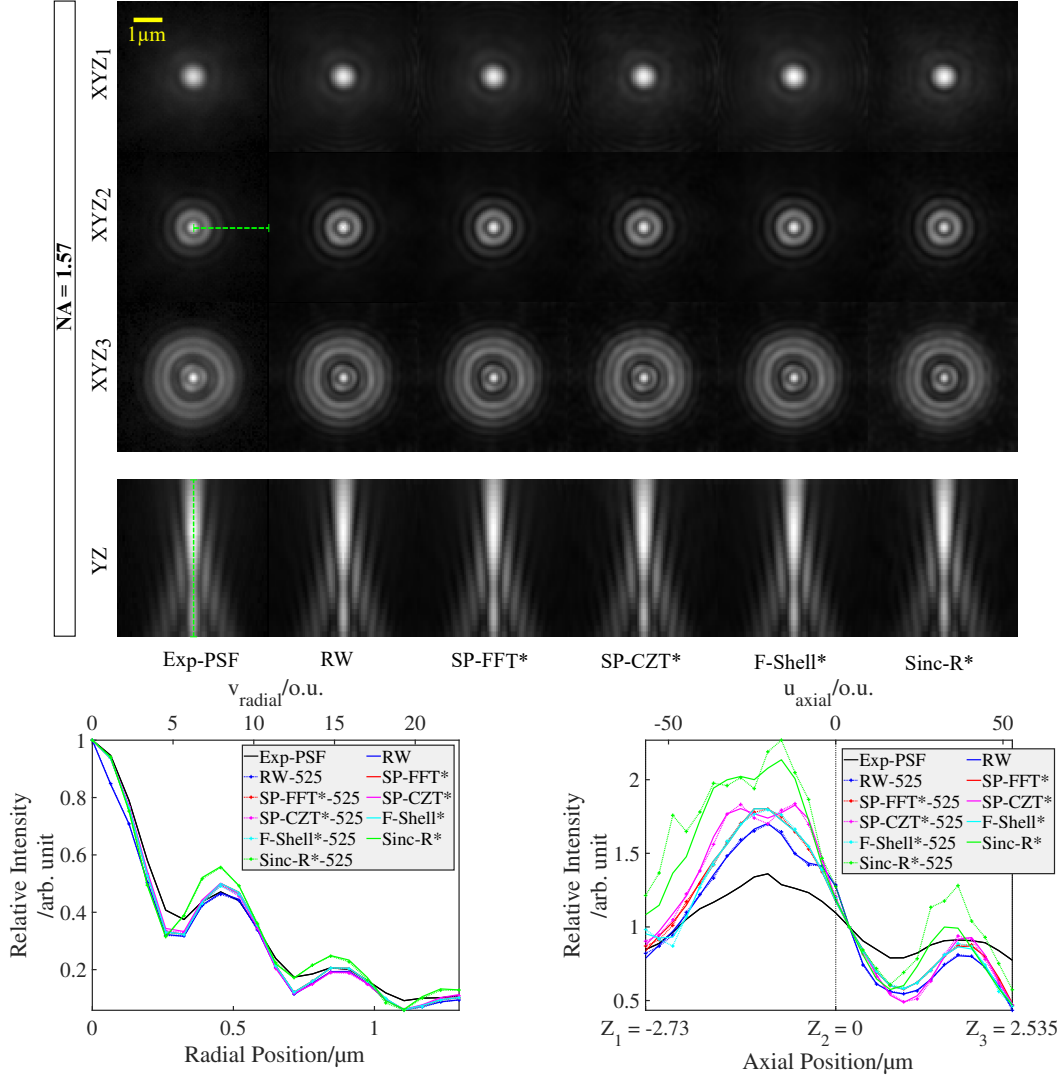


Figure 6.6: Display at $\gamma = 0.5$ of the xy -profiles sections at three different z -plane and yz -profiles at $x = 0$ of high NA Exp-PSF, $NA = 1.57$, and the corresponding simulated aberrant PSFs calculated from different methods. The legend of the figure follows the same trend as in Fig. 6.4.

the Exp-PSF at a NCC bigger than 0.97 (see Fig. 6.3c). This accuracy is similar to the NCC between a non-aberrant simulated PSF and an aberrant PSF calculated with a bead emitting at a $t_s = 5\lambda_0$ distance from the coverslip, $\lambda_0 = \lambda_{em}/n_i$ and $n_s = 1.46$. The Strehl ratio of this simulated aberrant PSF is equal to 0.78 and is close to the conventional Strehl ratio 0.8 of a system to represent an ideal system [88].

6.4.2 The effect of spherical aberration

In this second investigation, we introduce a spherical aberration into the system by changing the coverslip collar, t_{col} , setting of the system. The coverslip thickness used throughout the experiment remains the same. In our simulation, this corresponds to a change in value of the coverslip thickness in the design condition, t_g^* . The coverslip thickness, t_g^* , that the system is designed to correct for is linearly dependent on the

setting of the correction collar, t_{col} , by the relation:

$$t_g^* = 2t_{g|0.17}^* - t_{\text{col}}, \quad (6.4.1)$$

with $t_{g|0.17}^* = 0.17$ mm being the standard coverslip thickness in a design condition. Our imaging system consists of an EVOS M5000 with an air PLAN S-APO 40 \times objective lens of $NA = 0.95$, and working distance of 0.18 mm [EVOSTM Olympus: AMEP4754]. The pixel size in x and y is equal to 126 nm. The values of t_g^* and the step size, p_z in z , at different t_{col} setting at which the PSF data were acquired, are summarized in Table 6.2. The exposure time of each measurement is set to be 80 ms. The data was acquired from the Physiology laboratory, Stellenbosch University.

Table 6.2: Thickness of the coverslip in design condition, t_g^* , and the step size in z at t_{col}

t_{col}/mm	:	0.19	0.18	0.17	0.16	0.15
t_g^*/mm	:	0.15	0.16	0.17	0.18	0.19
p_z/nm	:	120	120	130	130	130

The TetrasSpeck bead sample is used for this measurement (see Section 6.2.2 for sample preparation). The phase aberration from the data at $t_{g|0.17}^*$ is retrieved using Algorithm 7 and added to the simulated data at different values of t_g^* .

The grid of the Exp-PSF at $t_{g|0.17}^*$ is of size equal to $64 \times 64 \times 50$ and is zero-padded laterally to $512 \times 512 \times 50$ for the phase estimation process. We have as a first guess parameters for the phase: $n_s = 1.3744$, $t_s = 31$ μm , and peak of defocus aberration $C_2^0 = -6.6116$ to compensate for the focal shift induced by the spherical aberration. The phase retrieval process is run over 100 iterations to lead to the best NCC value between Exp-PSF and the simulated aberrant PSF at $t_{g|0.17}^*$ equal to 0.9654.

The PSFs at different values of t_g^* ranging from 0.15 mm to 0.19 mm as described earlier are simulated. The retrieved phase from the Exp-PSF at $t_{g|0.17}^*$ is added in the pupil plane during the computation of each of the PSFs. The resulting aberrant PSFs from different methods at different values of t_g^* are displayed in Fig. 6.7.

We calculate the NCC values within the same z -range as the Exp-PSF. The NCC result between the theoretical PSFs at different values of t_g^* and the corresponding Exp-PSFs is given in Fig. 6.8f along side with relative intensity profiles of the theoretical PSFs and Exp-PSF along the axial axis in Fig. 6.8.

By quantifying the values of the resulting NCC, we found that although the NCC are very close for the RW, SP-FFT*, SP-CZT*, and F-Shell* methods, the SP-CZT* is found to be superior to the rest of the methods. The NCCs for these four methods range from 0.8564 to 0.9656. The Sinc-R* is been shown to have the least similarity with the Exp-PSF with a maximum value of NCC equal to 0.9341 and minimum of 0.8564.

By investigating the profiles of the intensity in the PSFs with varying values of t_g^* in Fig. 6.8a, 6.8b, 6.8c, 6.8d and 6.8e, we observe that the theoretical PSFs acquire similar trend as the Exp-PSF at different accuracy level.

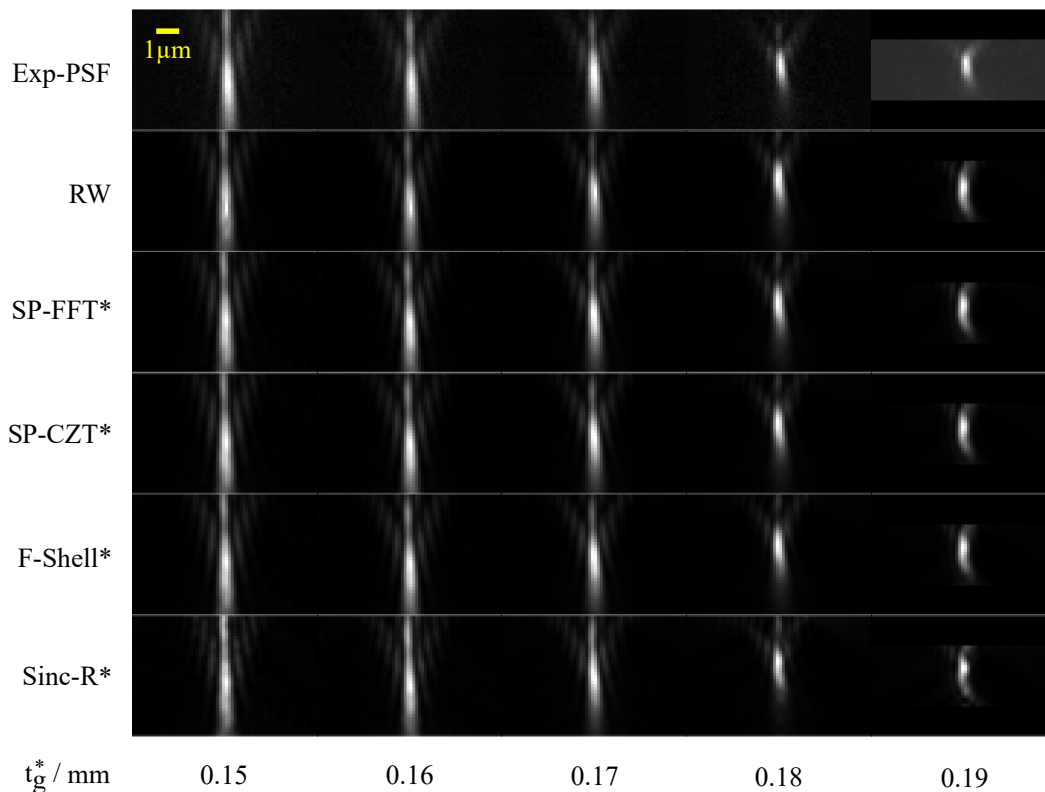


Figure 6.7: Display of the yz -profiles of the Exp-PSF, and the corresponding simulated aberrant PSFs calculated from different methods: RW, SP-FFT*, SP-CZT*, F-Shell*, and Sinc-R* from $NA = 0.95$ at different values of t_g^* .

6.5 PSFs for image reconstruction

6.5.1 Test images

Two sets of dataset are used to demonstrate the efficiency of the PSFs models for image reconstruction. The first dataset consists of the images of InSpeck green fluorescent bead of diameter $2.5\ \mu\text{m}$ imaged with a widefield microscope, Olympus Cell R, $63\times/1.4$ oil objective lens. This dataset is chosen as its feature enables an easy quantitative demonstration of a deconvolution technique performance with a given PSF model. Assuming that the deconvolution algorithm is appropriately optimized, if a given PSF does not yield to a good reconstruction of the bead, the probability that the PSF may not be suitable for reconstructing a more complex and finer object is high. The images of the beads were acquired at an emission wavelength equal to $530\ \text{nm}$. The voxel size of the images is $64.5 \times 64.5 \times 160\ \text{nm}^3$ and grid is $256 \times 256 \times 256$ voxels. The second dataset contains a more complex images of *C. Elegans* embryo with three different channels: DAPI ($\lambda_{\text{em}} = 477\ \text{nm}$), FITC ($\lambda_{\text{em}} = 542\ \text{nm}$), and CY3 ($\lambda_{\text{em}} = 654\ \text{nm}$) acquired from an Olympus Cell R microscope with an UPlanSApo $100\times/1.4$ oil objective lens. The voxel size is $64.5 \times 64.5 \times 200\ \text{nm}^3$ and the grid is cropped to a size of $256 \times 256 \times 256$ voxels. The two dataset are experimental data that are freely available online [89]. Each of them came with a simulated theoretical

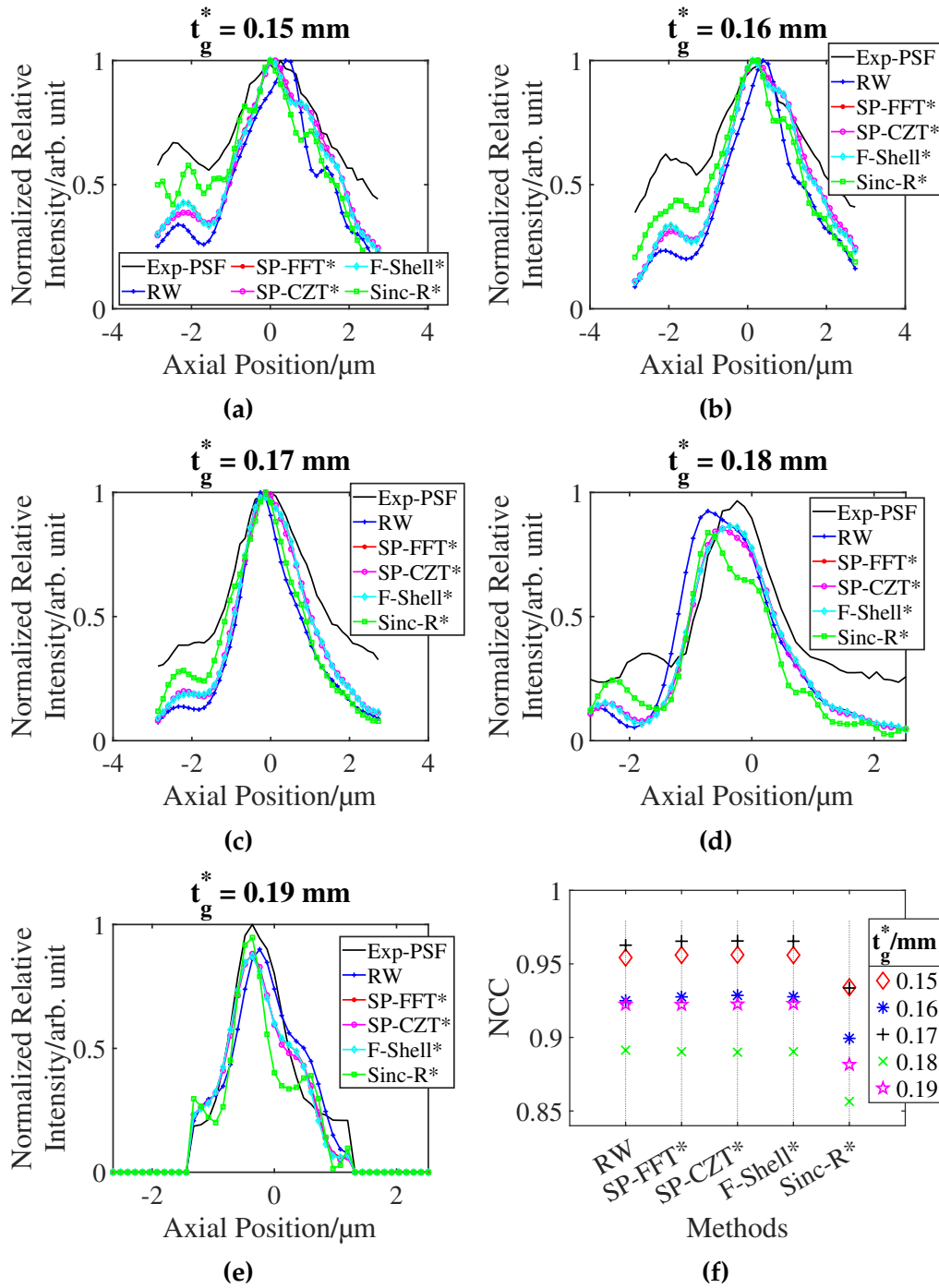


Figure 6.8: Relative intensity profiles of the theoretical PSFs and Exp-PSF along the axial axis at different t_g^* : (a) 0.15 mm, (b) 0.16 mm, (c) 0.17 mm, (d) 0.18 mm, and (e) 0.19 mm. (f) NCC between Exp-PSF and the aberrant simulated PSFs data.

PSF that we denote by PSF-DATA in this document.

6.5.2 Materials and methods

Two deconvolution process is done for each of the two dataset. The first process consists of deconvolving the data with their respective PSF-DATA and non-aberrant simulated PSFs. In the second process, we estimate the spherical aberration in the data and proceed to the deconvolution with aberrant simulated PSFs. In both cases, the goal is to quantify qualitatively and quantitatively how good each PSF is for a reconstruction of a simple as well as a complex feature in a data.

The deconvolution technique method is described in Section 2.5. The two data, spherical bead and *C. Elegans* embryo, are deconvolved using the Good's roughness penalty with an optimized regularization parameter, an assumption of a Poisson likelihood function in the cost function, and a square positivity constraint.

The most dominant noise in fluorescence microscopy data has been shown to follow a Poisson distribution [1, 75]. The Good's roughness penalty smoothens low intensity values, which usually correspond to light background, and has negligible effect on high intensity values, which correspond to real signals from the object to estimate. This attribute of the Good's roughness penalty makes it well suited for reconstructing fluorescence microscopy data [60]. A square positivity constraint is applied to avoid reconstructing negative values of the intensity.

We choose the limited memory Broyden-Fletcher-Goldfarb-Shanno algorithm (L-BFGS) as a minimization algorithm for its efficiency in large scale optimization [90]. This method minimizes the cost function iteratively using a limited amount of computer memory by storing a given number, smaller than the total number of iterations, of differences between two consecutive iterates (estimate of the bead object) and differences between the derivative of the corresponding cost values. The approximation of the Hessian matrix in the L-BFGS algorithm is updated using this information. The negative value of inverse Hessian matrix and the gradient of the cost function guides the line search of the best estimate of the object [90].

The deconvolution parameters for the first deconvolution process with non-aberrant PSFs are optimized by devolving the data using their respective PSF-DATA. The non-aberrant PSFs developed in this project, distinguished by * in their names (SP-FFT*, SP-CZT*, F-Shell*, Sinc-R*), as well as the state-of-the-art RW, GL, sPSF, vPSF and PSFGen are used and compared. Each of the three channels are deconvolved separately for the case of the *C. Elegans* embryo and the three deconvolved channels are combined afterwards. In the second deconvolution process, we estimate the amplitude of the spherical aberration in each of the data such that the resulting devolved image bead is symmetric about the plane in the focal plane. We do the optimization using the SP-FFT* aberrant PSF by measuring the symmetry in the xz and yz cross sections in the spherical bead of $2.5\ \mu\text{m}$ in diameter and by observing different spots

in the same sections for the *C. Elegans* embryo dataset. The phase aberration is added onto the PSFs and deconvolution with aberrant PSFs are compared. The resulting parameters for the two process and two dataset are summarized in Table 6.3.

Table 6.3: Deconvolution parameters for the spherical bead and the *C. Elegans* embryo

PSFs	Spherical bead				<i>C. Elegans</i> embryo			
	N_{iter}°	γ	n_s	$t_s/\mu\text{m}$	N_{iter}°	γ	n_s	$t_s/\mu\text{m}$
Non-aberrants	200	5×10^{-5}	1.46	0	75	5×10^{-5}	1.46	0
Aberrants	75	0	1.46	6.5	75	5×10^{-5}	1.46	20

with N_{iter}° being the number of iterations, γ the regularization parameter, n_s and t_s are the estimate optimized RI and thickness of the sample. Only the aberrant PSFs in our toolbox are used for the second investigation for the similar reason described in Section 6.4. The external software packages do not support the addition of the desired phase aberration. The GL method calculates an incorrect optical path difference (OPD) while the sPSF and vPSF are computationally expensive if an aberration due to refractive index mismatch is considered in the models.

6.5.3 Results

6.5.3.1 Visual inspection of the deconvolved bead data

The results from the image reconstruction of the spherical bead are displayed in Fig. 6.9. We observe that the the reconstructed data from PSF-DATA looks more elongated along z compared to the rest of PSFs, newly developed and state-of-the-art (see Fig. 6.9d). Its xz profile appears more symmetrical about the focal plane than the rest of the deconvolved data. This can be well seen by displaying the axial profile of the image of the recovered bead (see Fig. 6.10b).

The result with PSF-DATA does not seem realistic. A negative spherical aberration is present in the image of the bead (see Fig. 6.9b), yet in the resulting deconvolved image (see Fig. 6.9d), the asymmetry seems to be slightly resolved without the PSF-DATA containing any negative spherical aberration information. In Fig. 6.10b, we also observe that the axial intensity profile goes out of the bead size band. This is a clear indication of the error that is present in the PSF-DATA. We do not possess any additional information about the PSF-DATA to support this result.

From the see Fig. 6.9f to Fig. 6.9v, the reconstructed beads are observed to display asymmetry in xz . We found this to be more realistic given the image to deconvolve in Fig. 6.9b. The reconstructed beads from the scalar PSFs are however smaller than all the other reconstructed beads (see Fig. 6.9p and 6.9r). From the axial and radial profiles, it is clearly seen that the reconstruction with the scalar PSFs yields to a bead with a size smaller than its theoretical size (see Fig. 6.10b). This is physically not correct as it means that the bead gets compressed along the axial axis.

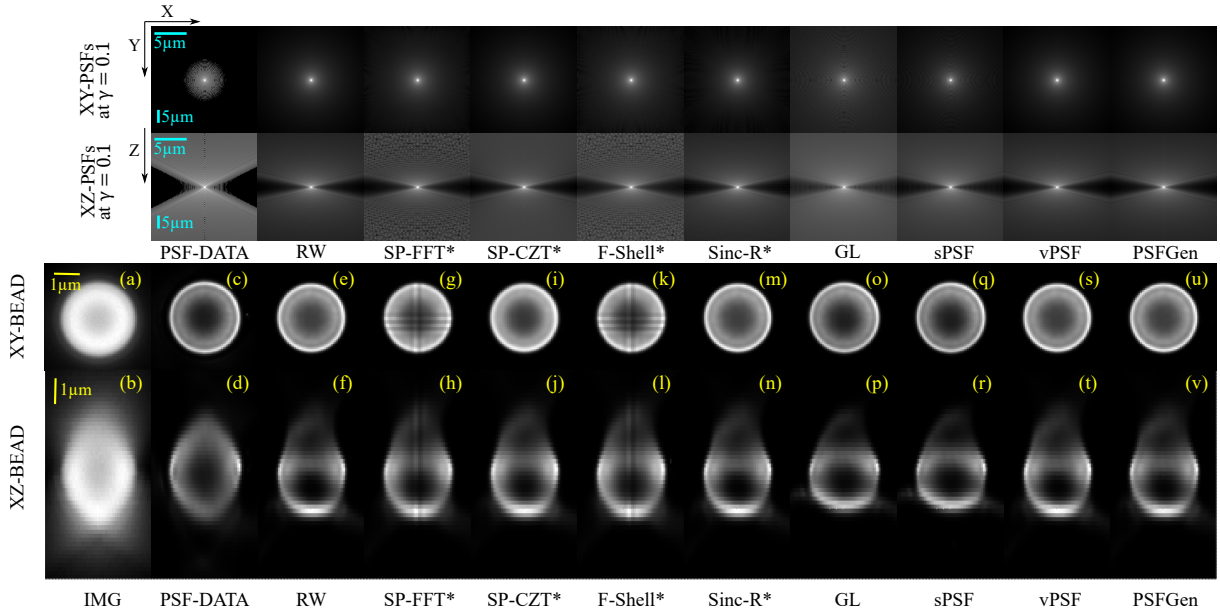


Figure 6.9: Results from the deconvolution of the image of a spherical bead of diameter $2.5 \mu\text{m}$ at 200 iterations. First row: xy -profile of the in-focus PSF displayed at percentile stretch of DipPimage. Second row: xz -profile of the PSF at $y = 0$ displayed at percentile stretch of DipPimage. Third row: xy -profile of the raw image of the bead and the deconvolved bead. Fourth row: xz -profile of the image of the bead and the deconvolved bead. The PSFs used for each respective column: PSF-DATA (theoretical PSF data which comes in the dataset), RW, SP-FFT*, SP-CZT*, F-Shell*, Sinc-R*, GL [34], sPSF and vPSF [37], PSFGen at best accuracy [33].

In Fig. 6.10a, we observe less ringing effect for the SP-FFT*, SP-CZT*, and F-Shell* methods. Around the zero radial position, the artefacts in the SP-FFT* and F-Shell* are observed to be significant. An edge artefact and Fourier-wrap around effects, that can be mistaken as important information in the object, are also observed in the SP-FFT* and F-Shell* methods (see Fig. 6.9g, 6.9h, 6.9k, and 6.9l).

Using the aberrant PSFs in our toolbox accounting for the phase aberration derived from the sample constant parameters given in Table 6.3, the spherical bead is reconstructed in all three spatial directions (see Fig. 6.13) after only 75 iterations and without any need for a regularization. The symmetry in the relative axial profiles intensities has fairly been resolved (see Fig. 6.10d).

A contrast improvement is also observed (see Fig. 6.10c). The contrast improvement is quantified by calculating the steepness of the curve from the maximum intensity to the center position of the images relative to the steepness in the initial image IMG (Fig. 6.11a and 6.11b). The result is given in Table 6.4.

Table 6.4: Contrast improvement measured by the steepness calculated between the maximal intensity and the intensity at the center of the image relative to the steepness in the initial image (IMG)

IMG	RW	SP-FFT*	SP-CZT*	F-Shell*	Sinc-R*
1	80	150	162	152	78

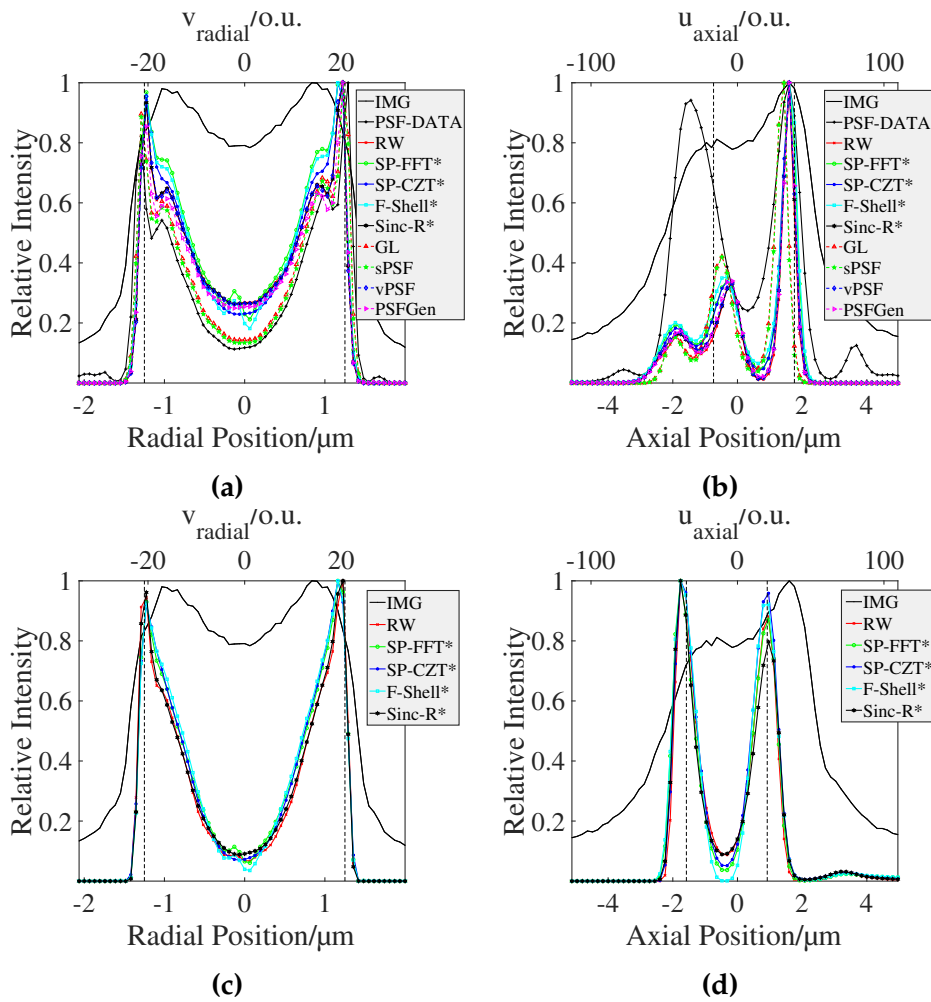


Figure 6.10: Relative radial (a) and axial (b) intensity profiles of the recovered bead from non-aberrant PSFs: PSF-Data, RW, SP-FFT*, SP-CZT*, F-Shell*, Sinc-R*, GL, sPSF, vPSF, and PSFGen. The theoretical bead’s size is indicated by the region within the two vertical dashed black lines in each figure. Relative radial (c) and axial (d) profiles of deconvolved data with the aberrant PSFs: RW, SP-FFT*, SP-CZT*, F-Shell*, and Sinc-R*. IMG: image of the spherical bead of diameter $2.5\ \mu\text{m}$.

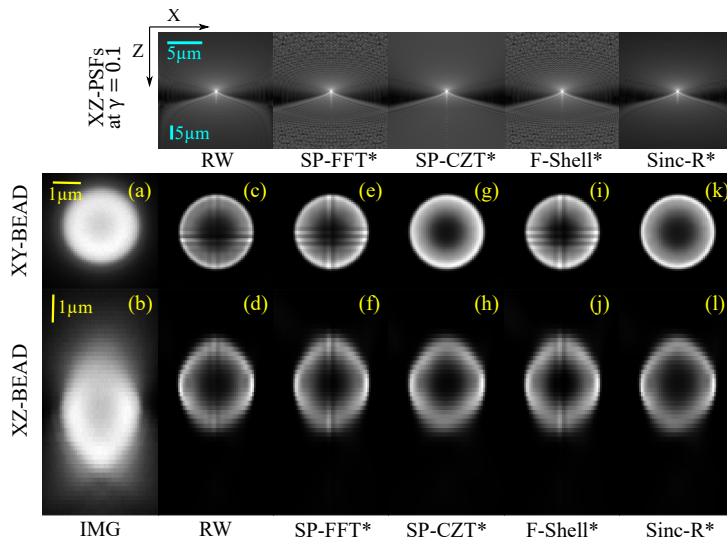


Figure 6.11: Results of the deconvolution of a spherical bead of $2.5\ \mu\text{m}$ in diameter with aberrant PSFs with sample constant parameters $n_s = 1.46$ and $t_s = 6.5\ \mu\text{m}$ at 75 iterations.

All the methods, RW, SP-FFT*, SP-CZT*, F-Shell* and Sinc-R*, have shown a contrast improvement more than 78 times better than the initial image IMG, SP-CZT* being the best and Sinc-R* being the worse with an improvement of 162 and 78 times respectively. The improvement by the SP-FFT* and F-Shell* are similar. The artefacts and Fourier wrap around effect on the reconstructed images from these two methods can still be observed (see profiles in Fig. 6.10c and 6.10d). The contrast improvement with the RW method is similar to the Sinc-R* method. Since we do not have a direct access to the pupil plane of the RW when adding the phase, an additional operation using a Fourier transform to go from real to Fourier space is required. This process may explain the low contrast improvement in the RW method.

Overall, we conclude that the our PSF models have performed well for image reconstruction of an object with a simple shape. In the next section, we inspect a more complex object to compare the efficiency of each model for image reconstruction.

6.5.3.2 Visual inspection of the deconvolved *C. Elegans* embryo data

In Fig. 6.12, we display the result from the deconvolution using the PSF-DATA and the non-aberrant external state-of-the-art vPSF [37]. This later PSF is chosen for its feature to show a high similarity to the newly developed methods in this project (see Section 4.3). The xz -profiles in Fig. 6.12d and 6.12f show the severe spherical aberrations that are still present in the deconvolved data and not corrected by the PSFs.

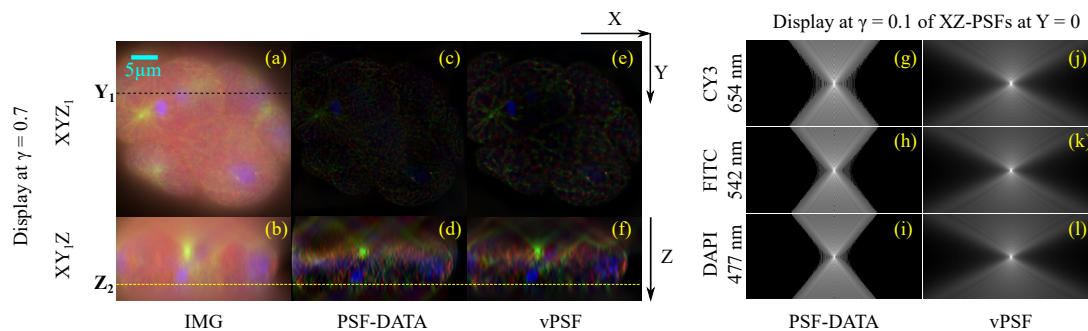


Figure 6.12: Results from the deconvolution of the *C. Elegans* embryo (a, b) with its corresponding three channels PSF-DATA (g, h, i) and the non-aberrant state-of-the-art vPSF (j, k, l) at the 75th iteration. (c, d) xy -profile at $Z_1 = 64$ pixel and xz -profile at $Y_1 = 151$ pixel of the deconvolved data with PSF-DATA respectively. (e, f) xy -profile at $Z_1 = 64$ pixel and xz -profile at $Y_1 = 151$ pixel of the deconvolved data with vPSF respectively.

Taking into consideration the phase aberration from the sample constant parameters given in Table 6.3, the results from the deconvolution using the aberrant PSFs, RW, SP-FFT*, SP-CZT*, F-Shell*, Sinc-R*, are displayed in Fig. 6.13. We observe that the spherical aberration is fairly corrected (indicated by the cyan arrow in Fig. 6.13b). A discontinuity is observed in the xz -intensity profile for the case of RW, SP-FFT*, F-Shell*, and Sinc-R* (indicated by the red arrow in Fig. 6.13). The discontinuity is due to the edge artefact and non-uniformity of the integrated intensity along the axial

axis. It is much significant for the case of F-Shell* and Sinc-R* (see Fig. 6.13j and 6.13m) while not observed in the result of SP-CZT* (see Fig. 6.13h). This therefore corresponds to the violation of the missing cone discussed in Section 4 where the Sinc-R* was shown to be the least among the techniques discussed in this section to satisfy (see Fig. 4.8a). This effect can be corrected if the PSF is sampled correctly and the missing cone is satisfied accurately, such is the case of the SP-CZT*. The SP-CZT* has proven to be the most accurate among the methods. Comparing the xy -profiles in Fig. 6.13 with the xy -profiles in Fig. 6.12, we also observe a better reconstruction of the small beads in the red channels. The contrast has also been improved. Due to the lack of ground truth of the object, this conclusion and observation are simply done qualitatively by eyes and not quantified.

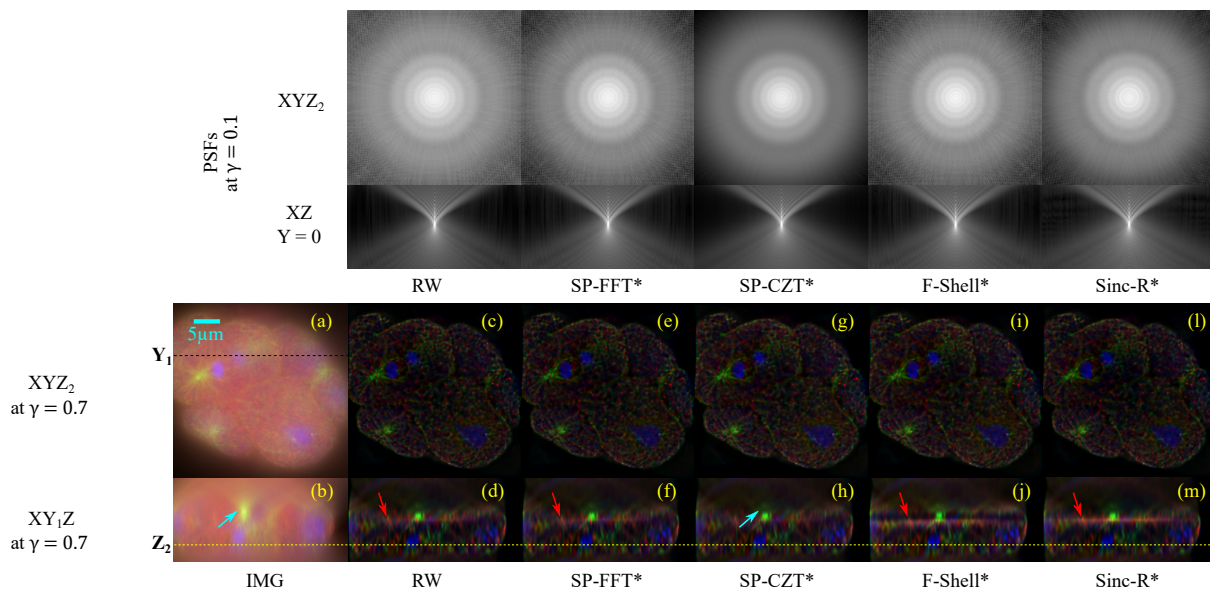


Figure 6.13: Results from the deconvolution of the images of *C. Elegans* embryo using aberrant PSFs RW, SP-FFT*, SP-CZT*, F-Shell*, and Sinc-R* with sample constant parameters $n_s = 1.56$ and $t_s = 20 \mu\text{m}$ at the 75th iterations. The xy and xz -profiles at $\gamma = 0.1$ of the respective PSFs are displayed in the first and second row. (a-b) xy and xz -slices of the image (denoted by IMG) to deconvolve. (c-d) deconvolved images using aberrant RW PSF. (e-f) with SP-FFT*. (g-h) with SP-CZT*. (i-j) with F-Shell*. (l-m) with Sinc-R*.

Chapter 7

Conclusion

Throughout the thesis, we tried to respond in a concise and chronological way to the central questions in high resolution imaging: “how to improve the image quality of an optical system?”. Our contribution and response to this goal consist of presenting and developing accurate and realistic estimate of the response, the point spread function (PSF), of the optical system. Past findings in the field are discussed with their pros and cons. Information about the novel methods that we develop under this thesis is given in detail. The focus on this work concentrated on wide-field microscopy, but the models can easily be extended to most of the advanced techniques in the field of fluorescence microscopy. The newly developed methods of PSF computing are used for image reconstruction, “deconvolution”, to improve the resolution of microscopic data obtained by a conventional microscope.

Four methods (SP-FFT, SP-CZT, F-Shell, and Sinc-R) for computing the PSFs using FFT are discussed, two of which (F-Shell and Sinc-R) are completely new. The two first methods, SP-FFT and SP-CZT, are not new in the literature but we have made progress in improving their computations and efficiency in this thesis. These four PSF models account for the vector features of the electric field. They represent the response of high NA optical imaging accurately with a NCC value higher than 0.97. The four models are also found to satisfy better the physical condition property of a wide-field imaging, the missing cone problem, compared to the existing PSFs in the state-of-the-art.

The limitation of each method and the ways around them are discussed. One limitation that may still occur in their computation is the Fourier wrap around problem, especially in the computation of a volume PSF with a high sample depth. This wrap-around can still be more significant for the case of SP-FFT and F-Shell at higher depth. This problem is resolved at a high computation cost using the CZT-based approach. The methods however have been demonstrated to be fast enough and memory efficient for their features in comparison to the state-of-the-art. As opposed to the state-of-the-art PSFs discussed in this thesis, our methods do not use any radial symmetry. They can support any type of aberration, spherical and non-spherical. They

can still be optimized to the same computation speed as the fast methods in the state-of-the-art if radial asymmetry is not important and radial symmetry is exploited. The Sinc-R method has been shown to be the least accurate among the four methods. The method can compute a volume PSF but not a slice. Its pros however is such that it does not suffer from the wrap-around problem.

Our models can also calculate the PSF from a tilted stratified medium. This feature of the PSF is new in the literature to the best of our knowledge. The finding has however not yet been validated experimentally. We aim to achieve this experimental validation in the near future.

The PSF models have demonstrated a high efficiency to reconstruct two objects: a spherical bead of 2.5 μm diameter and *C. elegans* embryo. The contrast improvement in the bead is found to be up to 162 times for the SP-CZT method. In the deconvolution of the *C. elegans*, which is a complex dataset recorded at three different channels, the efficiency and particularity of each PSF model to reconstruct finer object and the correction of the aberration was convincingly demonstrated.

A newly adapted phase retrieval algorithm that is suitable for noisy and strongly aberrated experimental wide-field PSF data was also presented in this thesis. The particularity of this algorithm is such that the experimental data from which the phase is to retrieve is with a small lateral number of pixels, roughly the size of the image of the bead at the given axial depth. The algorithm is proven to be efficient for such purposes theoretically and experimentally.

Two manuscripts are in preparation from this thesis. The theory of computing the novel PSF models are discussed in the first manuscript while the second manuscript details the experimental validation of the models. The toolbox containing the MATLAB codes will also be released and published openly with the first manuscript to a wider evaluation of the findings from this thesis and to help the community who may need it to advance their research.

Appendices

Appendix A

Detailed computation of the optical path difference

A.1 Optical path difference

We show the detailed steps for calculating the OPD in Chap. 5 Section 3.6.2 in this appendix. Some of the computation was done under the software Mathematica.

Let $\mathcal{R}_0 = \{O_0, x, y, z\}$ be the orthonormal coordinate system under which the electric field is calculated with O_0 being the center of the axis and z -axis represents the optical axis. The coverslip is firstly elevated by an angle α about the x -axis and is rotated azimuthally in counterclockwise about the vector normal to the coverslip plane by an angle β afterwards. A new orthonormal coordinate system $\mathcal{R}_1 = \{O_0, u, v, n\}$ is introduced to facilitate the computation of the OPD in the system such that \vec{n} is normal to the inclined coverslip (See Fig. A.1).

The vectors $\vec{u}, \vec{v}, \vec{n}$ are respectively defined by:

$$\vec{u} = \begin{pmatrix} \cos \beta \\ \sin \beta \\ 0 \end{pmatrix}; \vec{v} = \begin{pmatrix} -\sin \beta \cos \alpha \\ \cos \beta \cos \alpha \\ \sin \alpha \end{pmatrix} \text{ and } \vec{n} = \begin{pmatrix} \sin \beta \sin \alpha \\ -\cos \beta \sin \alpha \\ \cos \alpha \end{pmatrix} \quad (\text{A.1.1})$$

The rotation matrix which enables us to represent any vector defined in \mathcal{R}_1 in \mathcal{R}_0 is as follows:

$$M^{1|0} = \begin{pmatrix} \cos \beta & -\sin \beta \cos \alpha & \sin \beta \sin \alpha \\ \sin \beta & \cos \beta \cos \alpha & -\cos \beta \sin \alpha \\ 0 & \sin \alpha & \cos \alpha \end{pmatrix} \quad (\text{A.1.2})$$

The rotation matrix $M^{0|1}$ from \mathcal{R}_0 to \mathcal{R}_1 is the transpose of $M^{1|0}$.

The OPD is given by:

$$\text{OPD} = [O_s A_1 B_1 C_1] - [OBCH], \quad (\text{A.1.3})$$

where $[OBCH]$ represents the path that the light travels from the sample placed at the surface of the coverslip to the lens system under design conditions. O indicates

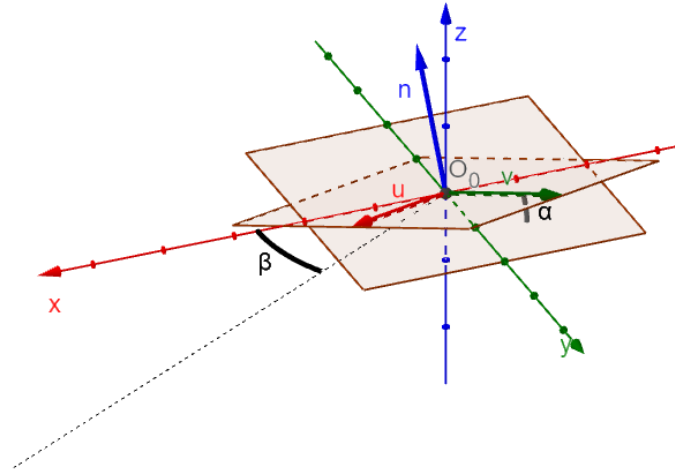


Figure A.1: Orthonormal coordinate system

the position of the emitter in design condition. In this case, the points A and B belong to the immersion medium and coverslip interface (plane $\kappa_{\text{im-cs}}^0$ in Fig. 3.10) and OA represents the thickness of the coverslip in design condition. If the system does not meet the condition under which the system was designed for, the same parallel ray \overrightarrow{CD} in the lens region will focus at a different position G as indicated in Fig. 3.10. Assuming the emitter is placed along the optical axis at the point O_s at the same depth as G from the coverslip-sample interface $\kappa_{\text{cs-s}}$ and under the system same arbitrary non-design condition. The emitted light follows the path indicated by the vectors passing by the points O_s, A_1, B_1, C_1 . The optical path $[O_s A_1 B_1 C_1 D_1]$ is parallel to $GFED$ and CD is parallel to $C_1 D_1$ (see Fig. 3.10). The point O_g is the intersection of the optical axis with the interface $\kappa_{\text{cs-s}}^1$ in Fig. 3.10, and O_i is the intersection of the optical axis with the immersion medium - coverslip $\kappa_{\text{im-cs}}^1$ interface. The immersion medium and front surface of the lens is set to be at the origin O_0 of the \mathcal{R}_0 axis to facilitate the computation.

The thicknesses of the coverslip and the specimen are t_g and t_s respectively. The star symbol is to indicate that the value of the thickness of the coverslip, t_g^* , is in design condition. At the lens and immersion medium plane interface $\kappa_{\text{l-im}}$, the beam arrives at a different radial position C_1 under the arbitrary condition illustrated here.

A.1.1 Design condition

The black arrows in Fig. 3.10 indicate the path travelled by light when the system meets the design condition. The incident ray \vec{OB} is incident on the planar interface $\kappa_{\text{im-cs}}^0$ and is deviated about the vector normal to the interface, which is parallel to the z -axis, into ray \vec{BC} due to the refractive index mismatch between the coverslip and the immersion medium. The ray \vec{BC} is on its turn deviated to get the vector \vec{CD} which is inclined by an angle θ about the z -axis. Those vectors form a plane of incidence, named ζ_0 which is perpendicular to the interfaces and placed at an angle ϕ from the x -axis. The optical path in the design condition is given by:

$$[OBCH] = n_g^* OB + n_i^* BC + nCH, \quad (\text{A.1.4})$$

$$= \frac{n_g^* t_g^*}{\cos \theta_g^*} + \frac{n_i^* t_i^*}{\cos \theta_i^*} + nCH \quad (\text{A.1.5})$$

where n_g^* , n_i^* and n_l are the refractive index of the coverslip, immersion medium and lens respectively. The parameter t_i^* represents the working distance of the objective lens. The angle θ_g^* and θ_i^* are elevation angles of the vectors \vec{OB} and \vec{BC} respectively. They can be calculated using Snell's law:

$$n_l \sin \theta = n_i^* \sin \theta_i^* = n_g^* \sin \theta_g^*. \quad (\text{A.1.6})$$

The position of the point C in space is of importance to calculate the segment CH . It is given by:

$$C = \begin{pmatrix} t_g^* \cos \phi \tan \theta_g^* + t_i^* \cos \phi \tan \theta_i^* \\ t_g^* \sin \phi \tan \theta_g^* + t_i^* \sin \phi \tan \theta_i^* \\ 0 \end{pmatrix} \quad (\text{A.1.7})$$

A.1.2 Non-design condition

The optical path in non-design condition on the other hand is expressed as follows:

$$[O_s A_1 B_1 C_1] = n_s O_s A_1 + n_g A_1 + n_i B_1 C_1, \quad (\text{A.1.8})$$

$$= \frac{n_s t_s}{\cos \gamma_s} + \frac{n_g t_g}{\cos \gamma_g} + \frac{n_i t_i'}{\cos \theta_i'}, \quad (\text{A.1.9})$$

where $t_i' = t_i - \Delta t_i$ is to be determined, n_s is the refractive index of the sample, γ_g and γ_s are the incident angle with respect to the normal vector \vec{n} on the coverslip - sample interface $\kappa_{\text{cs-s}}$ and sample surface respectively. The constant parameters t_s and t_g are the thickness of the sample and the coverslip respectively and t_i is the thickness of the immersion medium at the center of the xy -axis such that:

$$t_i = n_i \left(\frac{\Delta z}{n_i} - \frac{t_g}{n_g} - \frac{t_s}{n_s} + \frac{t_g^*}{n_g^*} + \frac{t_i^*}{n_i^*} \right), \quad (\text{A.1.10})$$

with Δz being the shift along the axial axis from the focal plane due to defocusing. The variable Δt_i is a change in the thickness of the immersion medium due to the tilt parameters α and β .

To calculate the thickness t'_i , the position of B_1 is required. The expression of t'_i is equal to the absolute value of the z -coordinate of the point B_1 along the optical axis in \mathcal{R}_0 . The position C_1 at which the ray arrives at the $\kappa_{\text{im-cs}}^1$ interface in a non-design condition enables the computation of the segment CH . To determine the position of the points B_1 and C_1 , we define a new coordinate system formed by the three unit vectors: \vec{u}' , \vec{v}' and \vec{n} . Let ζ_1 be the plane of incidence of the inclined coverslip. The plane ζ_1 is formed by the vector \vec{n} normal to the plane $\kappa_{\text{im-cs}}^1$ and the vector \vec{EC} . The vector \vec{EC} has as unit vector $\hat{u}_{\vec{EC}}^0$ defined in \mathcal{R}_0 and $\hat{u}_{\vec{EC}}^1$ defined in \mathcal{R}_1 . The two planes of incidence ζ_0 and ζ_1 intersect on the vector \vec{EC} (see Fig. A.2).

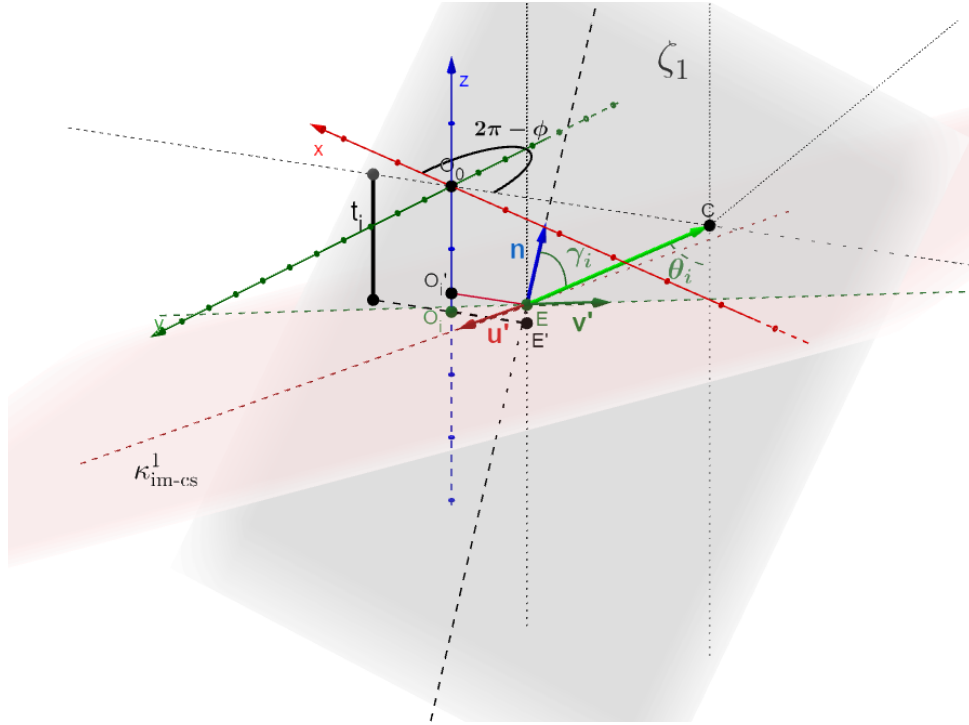


Figure A.2: Diagram illustrating the new coordinate system $\{\vec{u}', \vec{v}', \vec{n}\}$ for calculating the immersion medium thickness in non-design condition and the positions of B_1 and C_1 .

The vector \vec{n} was previously computed in (A.1.1). The vector \vec{u}' is normal to the plane of incidence ζ_1 and the vector \vec{v}' completes the new basis such that:

$$\vec{v}' = \frac{\vec{V}}{\|\vec{V}\|} \text{ with } \vec{V} = \hat{u}_{\vec{EC}}^0 - \cos \gamma_i \vec{n}, \quad (\text{A.1.11})$$

and, $\|\vec{V}\| = \sqrt{1 + \cos^2 \gamma_i - 2 \cos \gamma_i (\cos \alpha \cos \theta_i + \sin \alpha \sin \theta_i \sin(\beta - \phi))}$.

We have

$$\overrightarrow{O_0 B_1} = \overrightarrow{GE} + \overrightarrow{O_0 O_s}, \quad (\text{A.1.12})$$

with $\overrightarrow{GE} = -(t_s + t_g)\vec{n} - (t_s \tan \gamma_s + t_g \tan \gamma_g)\vec{v}'$. The refracted angles satisfy Snell's law:

$$n_i \sin \theta_i = n_l \sin \theta \quad n_i \sin \gamma_i = n_g \sin \gamma_g = n_s \sin \gamma_s, \quad (\text{A.1.13})$$

The angle γ_i can easily be calculated by expressing its unit vector \hat{u}_{EC}^0 in the reference \mathcal{R}_1 : $\hat{u}_{EC}^1 = M^{01}\hat{u}_{EC}^0$. Since \mathcal{R}_0 and \mathcal{R}_1 are both two orthonormal coordinate systems, the third component of \hat{u}_{EC}^1 only contains the cosine of the elevation angle which corresponds to γ_i . We have:

$$\cos \gamma_i = \cos \alpha \cos \theta_i + \sin \alpha \sin \theta_i \sin(\beta - \phi). \quad (\text{A.1.14})$$

The position of C_1 is given by:

$$\overrightarrow{O_0C_1} = \overrightarrow{GE} + \overrightarrow{B_1C_1} + \overrightarrow{O_0O_s} \quad (\text{A.1.15})$$

$$= \overrightarrow{GE} + \frac{t'_i}{\cos \theta_i} \hat{u}_{EC}^0 + \overrightarrow{O_0O_s}, \quad (\text{A.1.16})$$

with $t'_i = -z_{B_1}$ being the immersion medium thickness at point B_1 which is equal to the negative z -coordinate of the point B_1 :

$$t'_i = t_i + f_g + f_s, \quad (\text{A.1.17})$$

with

$$f_j = t_j(1 - \cos \alpha) + \frac{t_j \tan \gamma_j}{\|\vec{V}\|} (-\cos \theta_i + \cos \alpha \cos \gamma_i). \quad (\text{A.1.18})$$

A.1.3 Optical path difference

The last component of the OPD to be calculated is the segment CH . Both points C and C_1 belong to the same plane κ_{im} at $z = 0$ and the diagram A.3 is used for this computation.

Using the diagram in Fig. A.3, we have:

$$CC_b = CC_a + C_a C_b, \quad (\text{A.1.19})$$

$$CC_a = \frac{x_{C_1} \tan \phi - y_C}{\sin \phi}, \quad (\text{A.1.20})$$

$$CC_b = C_a C_1 \sin \phi, \quad (\text{A.1.21})$$

$$C_a C_1 = (y_{C_1} - y_C) - (x_{C_1} - x_C) \tan \phi. \quad (\text{A.1.22})$$

Using the four equations above, we get

$$CC_b = \frac{x_{C_1} \tan \phi - y_C}{\sin \phi} + (y_{C_1} - x_{C_1} \tan \phi) \sin \phi \quad (\text{A.1.23})$$

$$CH = CC_b \sin \theta \quad (\text{A.1.24})$$

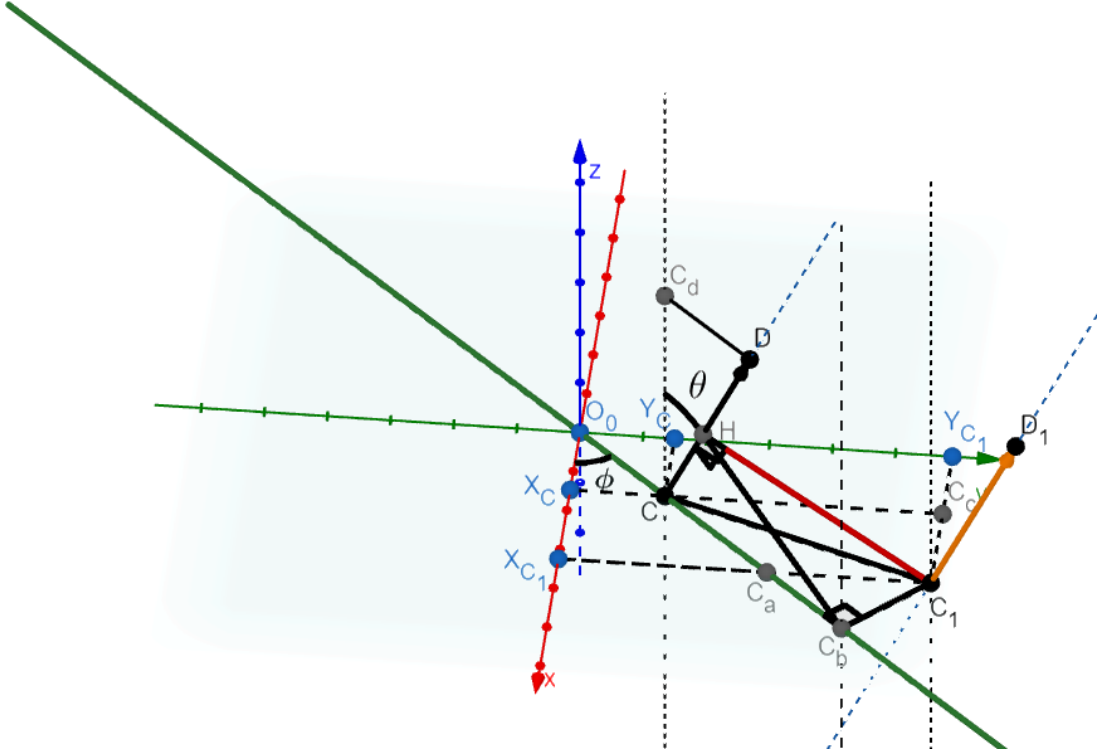


Figure A.3: Determination of the segment CH . The points C and C_1 have coordinates $(x_C, y_C, 0)$ and $(x_{C_1}, y_{C_1}, 0)$ respectively. The line (O_0C) is a line formed by the point C with the axis origin O_0 and is at an azimuthal angle ϕ from the x -axis. The point C_a is the intersection of (O_0C) with the line formed by $(X_{C_1}C_1)$ and the point C_b is the intersection of the perpendicular line of (O_0C) passing by C_1 with (O_0C) . The point C_d is the projection of D onto the line parallel to the z -axis passing by C . The angle formed by D, C and C_d is equal to θ and so the angle formed by C_b, C and H is also θ . The line (CD) and (C_1D_1) are parallel.

By replacing the x and y component of C and C_1 using Eq. (A.1.7) and Eq. (A.1.16), with the help of the software Mathematica, we have:

$$CC_b = t_g^* \tan \theta_g^* + t_i^* \tan \theta_i^* + t_i \tan \theta_i + CC_{b|t_g} + CC_{b|t_s} \quad (\text{A.1.25})$$

such that

$$CC_{b|t_j} = t_j [\sin \alpha \sin(\beta - \phi) + (1 - \cos \alpha) \tan \theta_i] + \frac{t_j \tan \gamma_j \cos \gamma_j}{\|\vec{V}\|} [\sin \alpha \sin(\phi - \beta) + \cos \alpha \tan \theta_i], \quad (\text{A.1.26})$$

where $j = g$ corresponds to coverslip and $j = i$ to the immersion medium in the non-design condition.

Using Eq. (A.1.3), (A.1.5), (A.1.9), the Snell's law for design and real condition in Eq. (A.1.6) and (A.1.13) respectively and replacing the expression of CC_b in the expression

of CH using Eq. (A.1.26), we have:

$$\text{OPD} = \frac{n_i t_i}{\cos \theta_i} - n_i t_i \sin \theta_i \tan \theta_i \quad (\text{A.1.27})$$

$$+ \frac{n_g t_g}{\cos \gamma_g} - n_i \sin \theta_i CC_{b|t_g} + \frac{n_i f_g}{\cos \theta_i} \quad (\text{A.1.28})$$

$$+ \frac{n_s t_s}{\cos \gamma_s} - n_i \sin \theta_i CC_{b|t_s} + \frac{n_i f_s}{\cos \theta_i} \quad (\text{A.1.29})$$

$$- \left(\frac{n_i^* t_i^*}{\cos \theta_i^*} - n_i^* t_i^* \sin \theta_i^* \tan \theta_i^* \right) \quad (\text{A.1.30})$$

$$- \left(\frac{n_g^* t_g^*}{\cos \theta_g^*} - n_g^* t_g^* \sin \theta_g^* \tan \theta_g^* \right) \quad (\text{A.1.31})$$

Replacing the immersion medium thickness t_i by its expression in Eq. (A.1.10) and regrouping the terms which commonly have the same thickness parameters, we obtain:

$$\text{OPD} = n_i \Delta z \cos \theta_i + \text{OPD}_g + \text{OPD}_s - \text{OPD}_g^* - \text{OPD}_i^*, \quad (\text{A.1.32})$$

such that,

$$\text{OPD}_j^* = \left(\frac{n_j^* t_j^*}{\cos \theta_j^*} - n_j^* t_j^* \sin \theta_j^* \tan \theta_j^* \right) - \frac{n_i^2}{n_j^*} t_j^* \cos \theta_i^* \quad (\text{A.1.33})$$

$$= n_j^* t_j^* \left[\cos \theta_j^* - \left(\frac{n_i}{n_j^*} \right)^2 \cos \theta_i \right], \quad (\text{A.1.34})$$

$$\text{OPD}_j = \frac{n_j t_j}{\cos \gamma_j} - n_i \sin \theta_i CC_{b|t_j} + \frac{n_i f_j}{\cos \theta_i} - \frac{n_i^2}{n_j} t_j \cos \theta_i. \quad (\text{A.1.35})$$

The expression of OPD_j can be simplified by replacing $\|\vec{V}\|$, $CC_{b|t_j}$ and f_j by their expressions in Eq. (A.1.11), (A.1.26) and (A.1.18) respectively. Given the expression of $\cos \gamma_i$ in Eq. (A.1.14), $\|\vec{V}\| = \sin \gamma_i$ and we have:

$$\begin{aligned} \text{OPD}_j &= \frac{n_j t_j}{\cos \gamma_j} \\ &\quad - n_i \sin \theta_i t_j [\sin \alpha \sin(\beta - \phi) + (1 - \cos \alpha) \tan \theta_i] \\ &\quad - n_i \sin \theta_i \frac{t_j \tan \gamma_j}{\sin \gamma_i} [\cos \gamma_i (\sin \alpha \sin(\phi - \beta) + \cos \alpha \tan \theta_i)] \\ &\quad + \frac{n_i}{\cos \theta_i} t_j (1 - \cos \alpha) + \frac{n_i}{\cos \theta_i} \frac{t_j \tan \gamma_j}{\sin \gamma_i} (-\cos \theta_i + \cos \alpha \cos \gamma_i) \\ &\quad - \frac{n_i^2}{n_j} t_j \cos \theta_i. \end{aligned} \quad (\text{A.1.36})$$

$$\begin{aligned}
\text{OPD}_j &= \frac{n_j t_j}{\cos \gamma_j} \\
&\quad - n_i t_j [\cos \gamma_i - \cos \theta_i] \\
&\quad + n_i t_j \frac{\tan \gamma_j}{\sin \gamma_i} \cos^2 \gamma_i \\
&\quad - n_i t_j \frac{\tan \gamma_j}{\sin \gamma_i} \\
&\quad - \frac{n_i^2}{n_j} t_j \cos \theta_i.
\end{aligned} \tag{A.1.37}$$

Further simplification using the equality $\tan \gamma_j = \frac{n_i \sin \gamma_i}{n_j \cos \gamma_j}$ reduces the expression of OPD_j to:

$$\text{OPD}_j = n_j t_j \left[\cos \gamma_j + \frac{n_i}{n_j} \left(-\cos \gamma_i + \left(1 - \frac{n_i}{n_j} \right) \cos \theta_i \right) \right] \tag{A.1.38}$$

By replacing $\cos \gamma_i$ by its expression in Eq. (A.1.14) and using the normalized radial coordinate $\rho = \frac{\sin \theta_i}{\eta}$ with η being the sine of the maximum angular aperture, we have:

$$\text{OPD}_j = n_j t_j \left[\cos \gamma_j + \frac{n_i}{n_j} \left\{ \left(1 - \frac{n_i}{n_j} - \cos \alpha \right) \cos \theta_i + \eta \sin \alpha \left(Z_1^1 \sin \beta - Z_1^{-1} \cos \beta \right) \right\} \right], \tag{A.1.39}$$

where Z_1^{-1} and Z_1^1 are the Zernike polynomials of order 1 which corresponds to the tilt about x and y axis respectively (see Appendix A.2.1). If the elevation tilt angle α of the coverslip is 0, $\gamma_j = \theta_j$ and Eq. (A.1.39) reduces to:

$$\text{OPD}_j = n_j t_j \left[\cos \theta_j - \left(\frac{n_i}{n_j} \right)^2 \cos \theta_i \right], \tag{A.1.40}$$

with $n_j \sin \theta_j = n_i \sin \theta_i$ satisfying Snell's law.

The general expressions of $\text{OPD}_{j|j=g,s}$ and $\text{OPD}_{j|j=g,i}^*$ in cosine terms are given and summarized as follow:

$$\text{OPD}_j^* = n_j^* t_j^* \left[\cos \theta_j^* - \left(\frac{n_i}{n_j^*} \right)^2 \cos \theta_i \right], \tag{A.1.41}$$

$$\text{OPD}_j = n_j t_j \left[\cos \gamma_j + \frac{n_i}{n_j} \left(-\cos \gamma_i + \left(1 - \frac{n_i}{n_j} \right) \cos \theta_i \right) \right]. \tag{A.1.42}$$

The angle γ_j equals to θ_j when the tilted angle is zero and the expression of OPD_j in Eq. A.1.42 simplifies to become similar as of A.1.41. Eq. A.1.41 and A.1.42 can be linearized by decomposing their cosine terms into Zernike polynomials. This decomposition is the focus of the rest of this Appendix.

A.2 Decomposition of the phase aberration into Zernike polynomials

A.2.1 Linear representation of aberrations

Optical aberrations can be decomposed into a set of orthogonal polynomials. The most common basis that has been used to represent optical aberrations is the set of Zernike polynomials formed by continuous and orthogonal polynomials over a unit circle [56]. The limitation of Zernike polynomials lies on their orthogonality over the whole circular pupil only. They are no longer orthogonal for a noncircular pupil [56]. Zernike polynomials are mathematically represented as follows:

$$Z_n^m(\rho, \phi) = \begin{cases} R_n^m(\rho) \cos(|m|\phi) & \text{if } m \geq 0, \\ R_n^m(\rho) \sin(|m|\phi) & \text{otherwise,} \end{cases} \quad (\text{A.2.1})$$

where $\rho \in [0, 1]$ is the normalized radial coordinate, $|m|$ the absolute value of m and ϕ is the azimuthal angle measured clockwise from the x -axis in any computation of the Zernike polynomial in this thesis. The radial function R_n^m is defined as follows:

$$R_n^m(\rho) = \sum_{l=0}^{(n-|m|)/2} \frac{(-1)^l (n-l)!}{l! [\frac{n+m}{2} - l]! [\frac{n-m}{2} - l]!} \rho^{n-2l}. \quad (\text{A.2.2})$$

The orthogonality of the Zernike polynomials is given by:

$$\int_0^{2\pi} \int_0^1 Z_n^m(\rho, \phi) Z_{n'}^{m'}(\rho, \phi) \rho d\rho d\phi = \frac{\pi \epsilon_m}{2n+2} \delta_{nn'} \delta_{mm'}, \quad \epsilon_m = \begin{cases} 2 & \text{if } m = 0 \\ 1 & \text{otherwise,} \end{cases} \quad (\text{A.2.3})$$

with $\delta_{nn'} = 1$ if $n = n'$ and 0 otherwise [56].

The phase map can be represented as a linear superposition of a sequence of Zernike polynomials:

$$W(\rho, \phi) = \sum_{n,m} C_n^m Z_n^m(\rho, \phi), \quad (\text{A.2.4})$$

with C_n^m defines the amplitude or coefficient of the given Zernike polynomial with the same radial and azimuthal orders. This decomposition has its importance in identifying and correcting for the most dominant aberration contained in a recorded data.

A.2.2 Decomposing $\cos \theta_j$ into Zernike polynomials

Let $G : \mathbb{R} \rightarrow \mathbb{R}$ be the function defined by $G(\theta_j) = \cos \theta_j$. Introducing a normalized radial coordinate $\rho = \frac{\sin \theta_i}{\eta}$, η being the sine of the maximum angular aperture and using the Snell's law at the interface:

$$n_j \sin \theta_j = n_i \sin \theta_i, \quad (\text{A.2.5})$$

we have

$$\cos \theta_j = \sqrt{1 - \left(\frac{n_i}{n_j}\right)^2 \sin^2 \theta_j} \quad (\text{A.2.6})$$

$$= \frac{n_i}{n_j} \eta \sqrt{\left(\frac{n_j}{n_i \eta}\right)^2 - \rho^2}. \quad (\text{A.2.7})$$

Firstly, let us define an arbitrary function $\Psi(\rho, \phi)$ with normalized radial coordinate ρ and azimuthal angle coordinate ϕ . The function Ψ can be represented into a combination of Zernike polynomials Z_n^{mp} of radial order n and azimuthal order m ; $n \geq m \geq 0, (n, m) \in \mathbb{N}^2$:

$$\Psi(\rho, \phi) = \sum_{n,m} A_n^m Z_n^{mp}(\rho, \phi). \quad (\text{A.2.8})$$

The parameter p is indicative of the parity of Z over ϕ . It raises Z_n^m into power of 1 if Z is even and -1 if Z is odd. To find the Zernike coefficients A_n^m , the orthogonality properties of the Zernike polynomials are used and we obtain:

$$A_n^m = \frac{2(n+1)}{\pi \varepsilon_m} \int_0^{2\pi} \int_0^1 \Psi(\rho, \phi) Z_n^{mp} \rho d\rho d\phi, \quad (\text{A.2.9})$$

with $\varepsilon_m = \begin{cases} 2 & \text{if } m = 0 \\ 1 & \text{otherwise} \end{cases}$ is called Newmann's factor.

Since G does not contain any azimuthal dependence, it can be fitted into circular Zernike polynomials of kind zero and order n , $Z_n^0(\rho) = R_n^0(\rho)$. The method used here to find the Zernike coefficients A_n^0 which correspond to G is similar of the one developed by Török et al. [26]. We have:

$$G(\rho) = \sum_{n=0}^{\infty} A_n^0 R_n^0(\rho), n = 2l \text{ and } l \in \mathbb{N} \quad (\text{A.2.10})$$

Using the general formulation in (A.2.9), the Zernike coefficients are given by

$$A_n^0 = \frac{n+1}{\pi} \int_0^1 G(\rho) R_n^0(\rho) \rho d\rho \quad (\text{A.2.11})$$

Introducing a change of variable $x = 2\rho^2 - 1, \rho^2 = \frac{x+1}{2}; dx = 4\rho d\rho$

If $\rho = 0, x = -1$ and $\rho = 1, x = 1$.

The expression of g becomes as follows in terms of x :

$$G(x) = \frac{n_i}{n_j \sqrt{2}} \eta \sqrt{2 \left(\frac{n_j}{n_i \eta}\right)^2 - 1 - x} \quad (\text{A.2.12})$$

Setting $l = n/2, l \in \mathbb{N}$ i.e. $n = 2l$ in Eq. ((A.2.11)), we have

$$A_{2l}^0 = \frac{2l+1}{\pi} \int_0^1 G(\rho) R_{2l}^0(\rho) \rho d\rho. \quad (\text{A.2.13})$$

Using the expression of the Legendre polynomials P_l of the first kind and order l defined in Eq. (34) of [26],

$$R_{2l}^0(\rho) = P_l(2\rho^2 - 1), \quad (\text{A.2.14})$$

With change of variables $\rho = \sqrt{\frac{1+x}{2}}$:

$$R_{2l}^0\left(\sqrt{\frac{1+x}{2}}\right) = P_l(x) \quad (\text{A.2.15})$$

We obtain:

$$A_{2l}^0 = \frac{2l+1}{4\pi} \int_{-1}^1 G(x) P_l(x) dx; \quad (\text{A.2.16})$$

Substituting the expression of G in function of x in Eq. (A.2.12) into Eq. (A.2.16), we have the expression of the Zernike coefficients which corresponds to the $\cos\theta_j$ in medium j :

$$A_{2l|j}^0 = \frac{2l+1}{4\pi\sqrt{2}} \left(\frac{n_i}{n_j}\right) \eta \int_{-1}^1 \sqrt{2\left(\frac{n_j}{n_i\eta}\right)^2 - 1 - x} P_l(x) dx, \quad (\text{A.2.17})$$

$$= \frac{2l+1}{4\pi\sqrt{2}} \left(\frac{n_i}{n_j}\right) \eta K_l \left[2\left(\frac{n_j}{n_i\eta}\right)^2 - 1\right], l \in \mathbb{N} \quad (\text{A.2.18})$$

Török et al. solved analytically the above integral in Eq. (A.2.17) [26]. The expression of K_l which was defined in Eq. (45) of [26] can be reformulated as:

$$K_l[X] = -\frac{\sqrt{2}}{(2l-1)(2l+1)} D^{1/2-l} \left[1 - \frac{2l-1}{2l+3} D^{-2}\right], \quad (\text{A.2.19})$$

with $D = X + \sqrt{X^2 - 1}$.

A.2.3 Decomposing $\cos\gamma_j$ into Zernike polynomials

Let $G : \mathbb{R} \rightarrow \mathbb{R}$ be the function defined by $G(\gamma_j) = \cos\gamma_j$. According to Snell's law, we have at the interface of media i and j :

$$n_j \sin\gamma_j = n_i \sin\gamma_i. \quad (\text{A.2.20})$$

So,

$$G(\gamma_j) = \sqrt{1 - \left(\frac{n_i}{n_j}\right)^2 (1 - \cos^2\gamma_i)}. \quad (\text{A.2.21})$$

Let us define $F(\gamma_i) = \cos^2\gamma_i$. Replacing the expression of $\cos\gamma_i$ by Eq. (A.1.14) and using the previously defined normalized radial coordinate ρ , we have the expression of F in function of ρ and ϕ :

$$F(\rho, \phi) = (1 - \eta^2\rho^2) \cos^2\alpha + 2\cos\alpha \sqrt{1 - \eta^2\rho^2} \eta\rho \sin(\beta - \phi) + \eta^2\rho^2 \sin^2(\beta - \phi). \quad (\text{A.2.22})$$

Expanding this expression, we obtain:

$$F(\rho, \phi) = -\frac{\eta^2}{2} \left\{ \cos(2\alpha) F_1(\rho) \right. \quad (\text{A.2.23})$$

$$\quad - 4 \cos \alpha \sin \beta F_2(\rho, \phi) \quad (\text{A.2.24})$$

$$\quad + 4 \cos \alpha \cos \beta F_3(\rho, \phi) \quad (\text{A.2.25})$$

$$\quad + \sin(2\beta) F_4(\rho, \phi) \quad (\text{A.2.26})$$

$$\quad \left. + \cos(2\beta) F_5(\rho, \phi) \right\} \quad (\text{A.2.27})$$

Using the same decomposition technique of the square root as in Section A.2.2, the expression of $F_1, F_2, F_3, F_4,$ and F_5 are as follows in terms of the corresponding Zernike polynomials:

$$F_1(\rho) = \rho^2 = \frac{1}{2} \left(Z_2^0(\rho) + 1 \right) \quad (\text{A.2.28})$$

$$F_2(\rho, \phi) = \sqrt{\frac{1}{\eta^2} - \rho^2} \rho \cos \phi = \left(\sum_{n=0}^{\infty} B_n^0 R_n^0(\rho) \right) Z_1^1(\rho, \phi) \quad (\text{A.2.29})$$

$$F_3(\rho, \phi) = \sqrt{\frac{1}{\eta^2} - \rho^2} \rho \sin \phi = \left(\sum_{n=0}^{\infty} B_n^0 R_n^0(\rho) \right) Z_1^{-1}(\rho, \phi) \quad (\text{A.2.30})$$

$$F_4(\rho, \phi) = \rho^2 \sin(2\phi) = Z_2^{-2}(\rho, \phi) \quad (\text{A.2.31})$$

$$F_5(\rho, \phi) = \rho^2 \cos(2\phi) = Z_2^2(\rho, \phi) \quad (\text{A.2.32})$$

$$(\text{A.2.33})$$

where the expression of the Zernike coefficients B_n^0 in Eq. (A.2.29) and (A.2.29) is similar as of the expression of A_n^0 in Eq. (A.2.18):

$$B_n^0 = \frac{n+1}{4\pi\sqrt{2}} K_{n/2} \left[\frac{2}{\eta^2} - 1 \right], n = 2l \text{ is even, } l \in \mathbb{N} \quad (\text{A.2.34})$$

A.2.4 Linear expression of the OPD in terms of the Zernike polynomials

Using the findings in Appendix A.2.2 and A.2.3 for the decomposition of $\cos \theta_j$ and $\cos \gamma_j$ respectively, we found the following:

$$\cos \theta_i = \sum_{n=0}^N B_n^0 R_n^0(\rho) \quad (\text{A.2.35})$$

$$\cos \theta_{j|j \neq i} = \sum_{n=0}^N A_{n|j}^0(n_i, n_j) R_n^0(\rho) \quad (\text{A.2.36})$$

$$\cos \gamma_i = \cos \alpha \sum_{n=0}^N B_n^0 R_n^0(\rho) + \eta \sin \alpha \left(Z_1^1(\rho, \phi) \sin \beta - Z_1^{-1}(\rho, \phi) \cos \beta \right) \quad (\text{A.2.37})$$

$$\cos \gamma_{j|j \neq i} = (1 - n_{ij}^2) \quad (\text{A.2.38})$$

$$- \frac{n_{ij}^2 \eta^2}{2} \left[\frac{\cos(2\alpha)}{2} (Z_2^0(\rho) + 1) \right] \quad (\text{A.2.39})$$

$$- 4 \cos \alpha \sin \beta \left(\sum_{n=0}^N B_n^0 R_n^0(\rho) \right) Z_1^1(\rho, \phi) \quad (\text{A.2.40})$$

$$+ 4 \cos \alpha \cos \beta \left(\sum_{n=0}^N B_n^0 R_n^0(\rho) \right) Z_1^{-1}(\rho, \phi) \quad (\text{A.2.41})$$

$$+ \sin(2\beta) Z_2^{-2}(\rho, \phi) \quad (\text{A.2.42})$$

$$+ \cos(2\beta) Z_2^2(\rho, \phi) \Big]^{1/2}, \quad (\text{A.2.43})$$

with η being the sine of the maximum angular aperture, ρ the normalized radial coordinate, $n_{ij} = n_i/n_j$, N is the finite number of the sequence of Zernike polynomials and $A_{n|j}^0$ is the Zernike coefficients of radial order n which corresponds to the medium j (see Eq. A.2.18). The Zernike coefficient B_n^0 is a particular case of $A_{n|j}^0$ which is independent of the refractive index *i.e.* $B_n^0 = A_{n|i}^0$.

By investigating the decomposition of the cosines terms above, we observe that a tilt in the coverslip with varying refractive index system breaks the radial symmetry in the wavefront. The terms $R_n^0(\rho) Z_1^1(\rho, \phi)$ and $R_n^0(\rho) Z_1^{-1}(\rho, \phi)$ in Eq. (A.2.40) and (A.2.41) can be proven to be proportional to a Zernike polynomial of a radial order $n' = n + 1, n = 2q$ and $q \in \mathbb{N}$ and azimuthal order 1 and -1 respectively.

By replacing the cosine terms in Eq. (A.1.41) and (A.1.42) with their corresponding Zernike decomposition, the expression of the OPD in Eq. (A.1.32) throughout the sample (s), coverslip (g) and immersion (i) medium can be simplified and linearized as follows:

$$\text{OPD} = \sum_{j=s,g,i^*} n_j t_j \left\{ C_0^0 + C_2^2 Z_2^2 + C_2^{-2} Z_2^{-2} + \sum_{n=0}^N C_n^0 Z_n^0 + \sum_{n'=1}^{N+1} C_{n'}^1 Z_{n'}^1 + \sum_{n'=1}^{N+1} C_{n'}^{-1} Z_{n'}^{-1} \right\} \quad (\text{A.2.44})$$

Appendix B

Visualisation of the effects of aberrations on PSFs

In this appendix, detailed figures from the analysis of simulated aberrant PSFs in comparison to the reference non-aberrant PSFs are shown. Aberrant PSFs are simulated with a set of varying variables $[n_s/n_i, t_s, \alpha]$. The parameters of the coverslip (t_g, n_g) are fixed in all the simulations described here. The details of the captions of the figures are given below.

Fig. B.1: the result from the comparison of an aberrant PSF at t_s ranging from $1\lambda_0$ to $9\lambda_0$ with the reference non-aberrant PSF is shown. Row (a): Wavefront error σ_W in wave unit (λ_0). Row (b): MRE. Row (c): NCC. Row (d): Strehl ratio S . First column: Wavefront error σ_W , S , MRE and NCC between the reference non-aberrant PSF and the aberrant PSF at varying n_s/n_i and α and fixed value of sample thickness $t_s = 1\lambda_0$ and $h_1 = h(n_s = n_i, t_s = 1\lambda_0, \alpha = 0)$. Second to fourth column: Difference in the wavefront error σ_W , MRE, NCC and S from $h(n_s/n_i, t_s = 1\lambda_0, \alpha)$ with the non-aberrant reference PSF and the σ_W , MRE, NCC and S from $h(n_s/n_i, t_s > 1\lambda_0, \alpha)$ with the non-aberrant reference PSF, h being the aberrant PSF.

Fig. B.2: Comparison of an aberrant PSF at t_s ranging from $50\lambda_0$ to $250\lambda_0$ with the reference non-aberrant PSF. Row (a): Wavefront error σ_W in wave unit (λ_0). Row (b): MRE. Row (c): NCC. Row (d): Strehl ratio. First column: $t_s = 50\lambda_0$. Second column: $t_s = 100\lambda_0$. Third column: $t_s = 150\lambda_0$. Fourth column: $t_s = 200\lambda_0$. Fifth column: $t_s = 250\lambda_0$.

Fig. B.3: Zernike coefficients C_n^m in wave unit λ_0 obtained with varying n_s/n_i at fixed values of t_s and α (first row), α at fixed values of n_s/n_i and t_s (second row) and different sample depth $t_s \in [50 : 50 : 250]\lambda_0$ (third row).

Fig. B.4: the Zernike coefficients C_n^m which corresponds to Fig. B.3 and having values greater than 0.075 are displayed. These figures have binary values such that 0 (white) corresponds to $C_n^m \geq 0.075$ and -1 (black) correspond to $C_n^m < 0.075$.

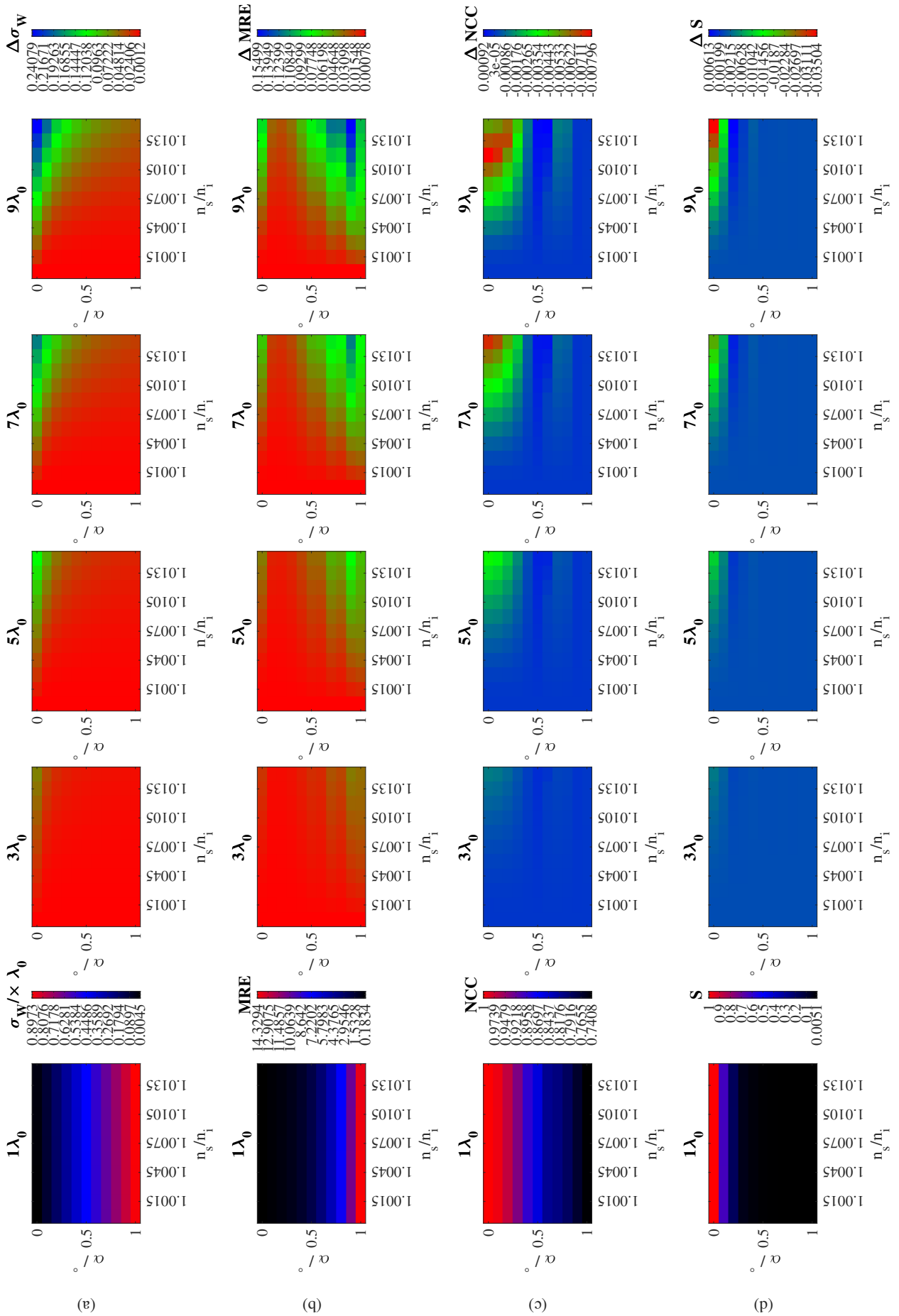


Figure B.1: Wavefront error σ_W in wave unit λ_0 , MRE, NCC and Strehl ratio S of an aberrant PSF at varying sample thickness t_s ranging from $1\lambda_0$ to $9\lambda_0$ in comparison with the reference non-aberrant reference PSF

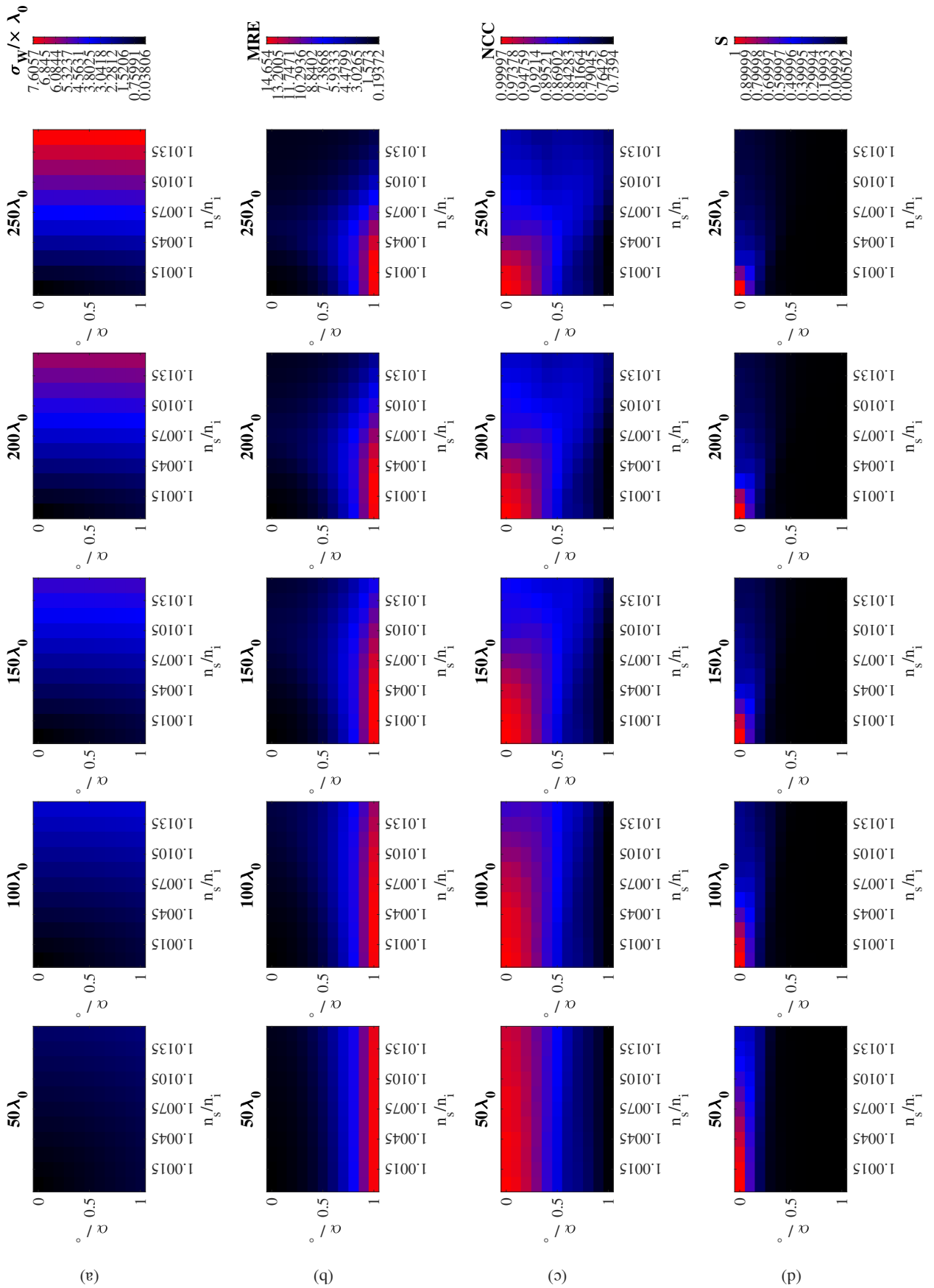
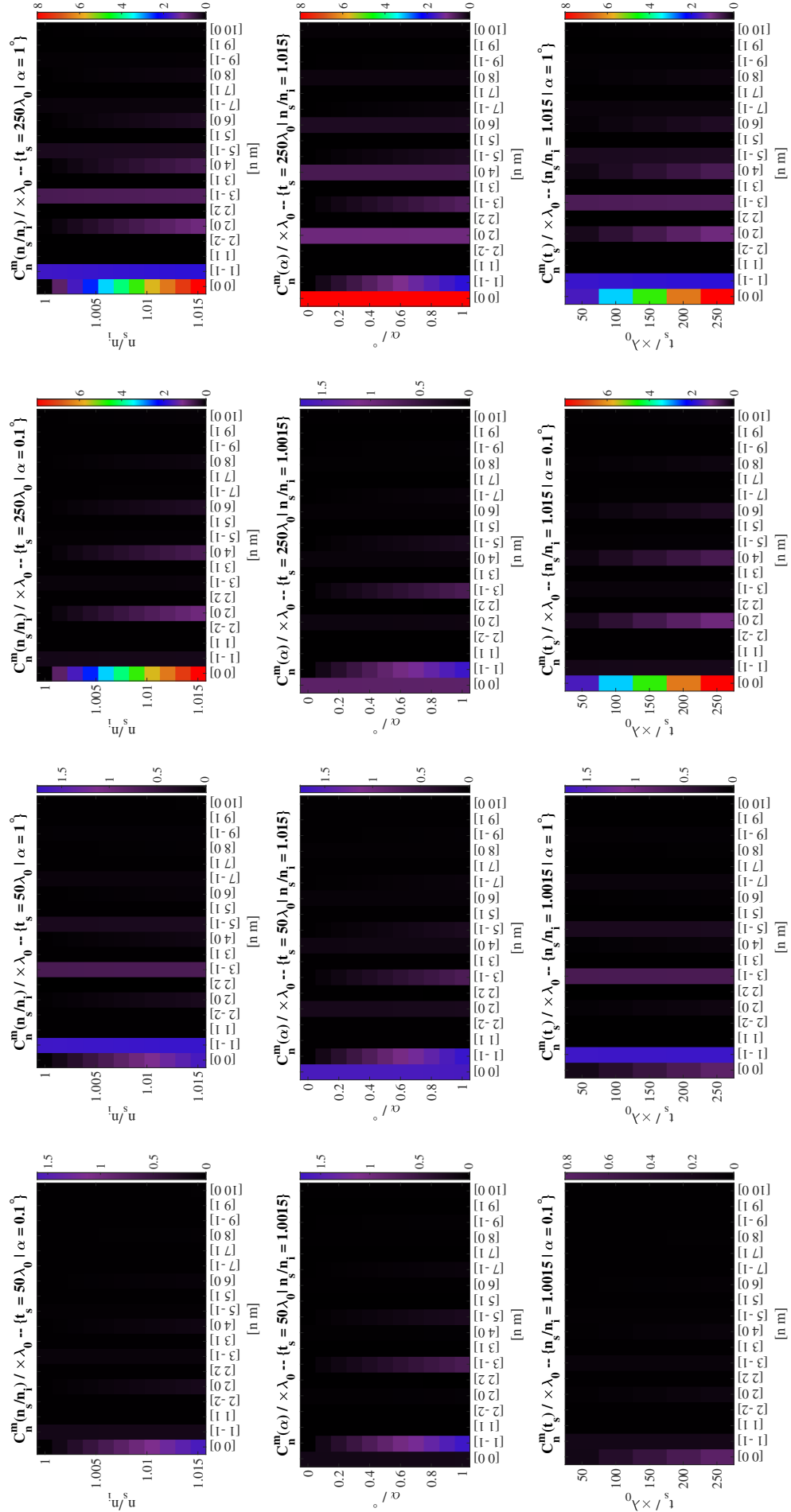


Figure B.2: Wavefront error σ_W in wave unit λ_0 , MRE, NCC and Strehl ratio S of an aberrant PSF at varying sample thickness t_s ranging from $50\lambda_0$ to $250\lambda_0$ in comparison with the reference non-aberrant reference PSF


 Figure B.3: Zernike coefficients C_n^m at different n_s/n_i , α and t_s

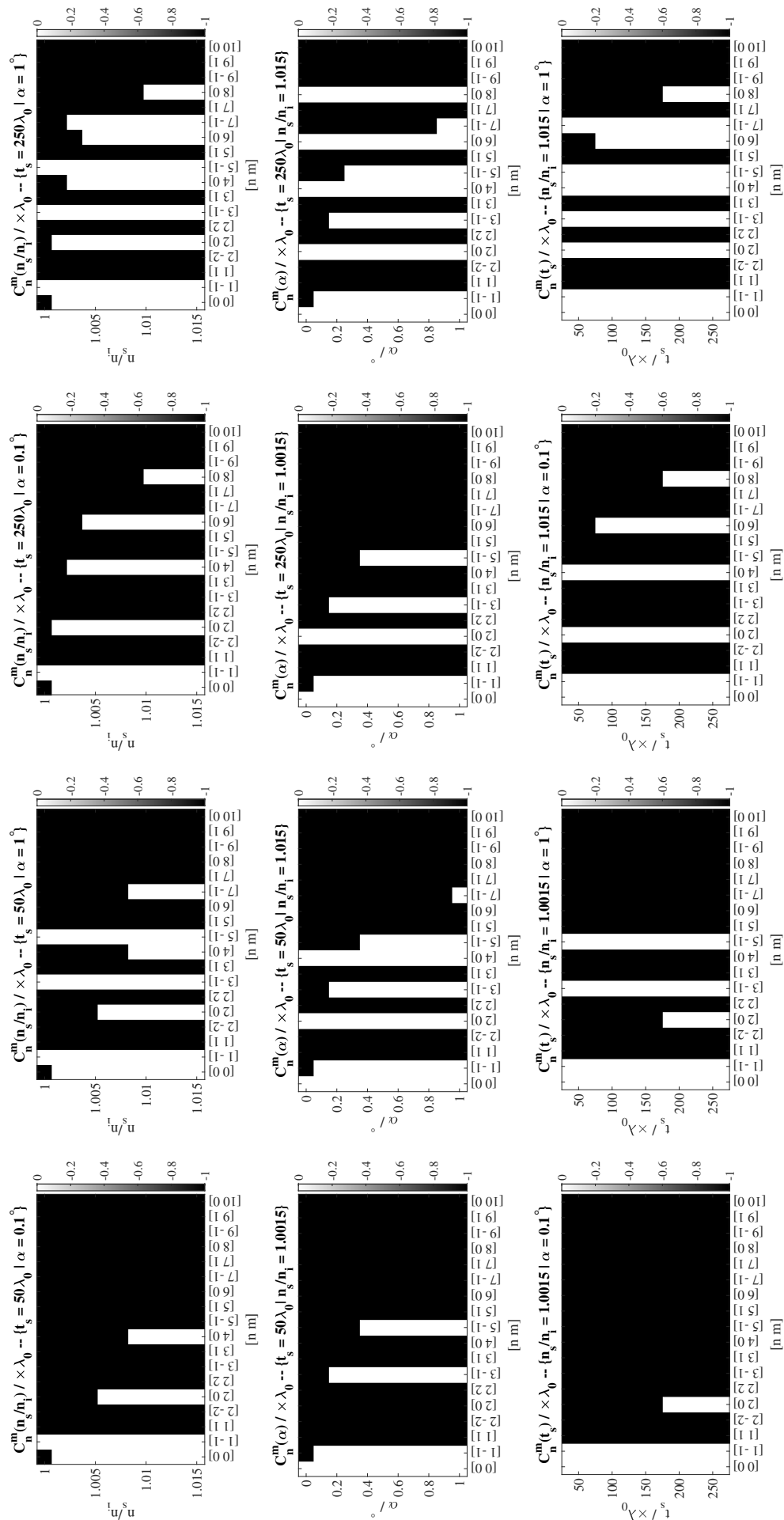


Figure B.4: Binary images which corresponds to Fig. fig:ZCoeff all higher depth representing the Zernike coefficients $C_n^m \geq 0.075\lambda_0$

Appendix C

Averaging over the dipole orientations

In this Appendix, the PSF obtained from the averaging over all possible dipole orientations is shown to be proportional to the PSF from a circular polarized light. We denote \vec{h}_x and \vec{h}_y the three-dimensional field amplitude distribution in the image plane that are derived from x and y -polarized incident light respectively. Given the linearity of the Maxwell equations, the vector wave equation can be decoupled. Propagating two linearly perpendicular polarized light and combining the propagated fields is equivalent to propagating a circularly polarized light. Mathematically, $\vec{h}_{\text{circ}}(x, y, z) = \frac{\sqrt{2}}{2} (\vec{h}_x(x, y, z) + i\vec{h}_y(x, y, z))$. The PSF intensity from a circularly polarized light is therefore given by:

$$h_{\text{circ}}(x, y, z) = \frac{1}{2} (h_{xx}^2 + h_{xy}^2 + h_{xz}^2 + h_{yx}^2 + h_{yy}^2 + h_{yz}^2), \quad (\text{C.0.1})$$

such that (h_{xx}, h_{xy}, h_{xz}) and (h_{yx}, h_{yy}, h_{yz}) are the respective components of \vec{h}_x and \vec{h}_y . On the other hand, the dipole orientation is given by:

$$\vec{\mu}(\theta_{\text{dip}}, \phi_{\text{dip}}) = \begin{pmatrix} \sin \theta_{\text{dip}} \cos \phi_{\text{dip}} \\ \sin \theta_{\text{dip}} \sin \phi_{\text{dip}} \\ \cos \theta_{\text{dip}} \end{pmatrix} \quad (\text{C.0.2})$$

with θ_{dip} and ϕ_{dip} being the elevation and azimuthal angles of $\vec{\mu}$ respectively. The expression of the dipole emission PSF described in Algorithm 6 can be expanded to:

$$h_{\text{dip}} = \frac{1}{2} \left([h_{xx} \sin \theta_{\text{dip}} \cos \phi_{\text{dip}} + h_{xy} \sin \theta_{\text{dip}} \sin \phi_{\text{dip}} + h_{xz} \cos \theta_{\text{dip}}]^2 \right. \quad (\text{C.0.3})$$

$$\left. [h_{yx} \sin \theta_{\text{dip}} \cos \phi_{\text{dip}} + h_{yy} \sin \theta_{\text{dip}} \sin \phi_{\text{dip}} + h_{yz} \cos \theta_{\text{dip}}]^2 \right) \quad (\text{C.0.4})$$

The integration of h_{dip} over all the possible dipole orientations equals to $(4\pi/3)h_{\text{circ}}$ *i.e.*

$$\int_0^{2\pi} \int_0^\pi h_{\text{dip}} \sin \theta_{\text{dip}} d\theta_{\text{dip}} d\phi_{\text{dip}} = (4\pi/3)h_{\text{circ}}. \quad (\text{C.0.5})$$

The possible orientations formed a volume sphere. This implies that the average of dipoles PSF over all the possible dipole orientations, h_{av} , given in Eq. (3.7.2) is equal to h_{circ} .

Appendix D

Sample preparation protocol

Cleaning procedure

It is important to wear gloves and laboratory coats when handling chemical products. To clean a coverslip or/and a microscope slide, the reagents and equipment stated in Section D.0.1 are needed and the steps mentioned in Section D.0.2 are followed.

D.0.1 Materials

- Hydroxide of potassium (KOH) solid
- Distilled water
- Coverslips and coverslip rack
- Alcohol (> 70%)
- Glass beaker
- Waste disposal for KOH and alcohol
- Storage container with cover

D.0.2 Method

1. Prepare 2N solution of KOH by dissolving 8.6 g of KOH pellets in 80 mL of distilled water.
2. Place the coverslips on a rack and submerge it in the KOH solution for 2 h. A laboratory glassware such as a glass beaker can be used for this purpose. An alternative for this step consists of sonicating the solution for 20 min at temperature equal to 30°.
3. Rinse the coverslips with a lot of distilled water by replacing the liquid which submerges it at least three times.
4. The coverslips are ready to use and they can be stored in room temperature by submerging them in alcohol solution of at least 70%. The container needs to be covered on top to avoid any dust coming in and the alcohol to evaporate.

5. Before use, remove the coverslip from the alcohol and let it dry in air or burn it with propane for about 1 s.

Bead solution

D.0.3 Materials

- 0.1 μm TetraSpeck microspheres with beads density equal to $d_0 = 1.8 \times 10^{11}$ particles/mL
- Distilled water
- 2 mL eppendorf centrifuge tubes
- Micropipette and pipette tips

D.0.4 Method

1. Vortex the concentrated beads solution to uniformly suspend it.
2. Take a 2 mL eppendorf centrifuge tube and dilute 5 μL of bead solution to 500 μL with distilled water for a 5 : 500 or 10^2 dilution. We denote this solution S_1 and it contains $N_1 = \frac{5 \mu\text{L} \times d_0}{V_0} = 9 \times 10^8$ particles, with $V_0 = 0.5 \times 10^3 \mu\text{L}$ being the volume of the initial solution in Step 1.
3. Vortex S_1 for 5 min to break the beads and avoid clusters.
4. Take another 2 mL eppendorf centrifuge tube and dilute 1 μL of bead solution S_1 to 10³ μL with distilled water for a 1 : 1000 or 10^3 dilution and a total 10^5 dilution. We denote this solution S_2 . It contains $N_2 = \frac{1 \mu\text{L} \times N_1}{V_1} = 1.8 \times 10^6$ particles, with $V_1 = 500 \mu\text{L}$ being the volume of the solution S_1 .
5. Vortex S_2 for 5 min to break the beads and avoid clusters.
6. The beads solution is ready to use. Store it in the dark at temperature 2° and always vortex for 5 min before use.

Using the same calculation as in Step 2 and 4, a 15 mL solution from S_2 contains about 27×10^3 particles. Given the surface area of a coverslip ($200 \mu\text{m} \times 200 \mu\text{m}$), the estimate average maximum number of beads that we obtain per surface area ($1 \mu\text{m}^2$) is less than or equal to 1 (0.675 beads per unit area to be exact) which is acceptable as the solution will be concentrated at the center of the coverslip first and many of the beads split out from the coverslip during spin-coating. It is advisable to use a total dilution of 10^6 if the sample is dried coat onto the coverslip instead of spin-coated.

Appendix E

Image quality metrics

Wavefront error: σ_W

The wavefront error quantifies the spread of the deviation of the optical imaging from the design condition. It is statistically defined as the standard deviation of the OPD over the pupil area:

$$\sigma_W = \left(\frac{1}{\pi r_p^2} \int_{\text{pupil}} [\text{OPD}(\rho, \phi; \tau_d, \tau_r) - \overline{\text{OPD}}]^2 \rho d\rho d\phi \right)^{1/2}, \quad (\text{E.0.1})$$

with r_p is the pupil radius, τ_d and τ_r represent the set of parameters in design and non-design condition respectively and $\overline{\text{OPD}}$ being the average OPD over the pupil area.

Strehl ratio: S

Strehl ratio is defined as the ratio of the intensity of the aberration-free PSF at its centre position with the intensity PSF at the same position when it gets aberrated [85]. As the maximum wave interference occurs at the centre of the PSF, this ratio is used to quantify the amount of aberration as well as a way to balance the present aberration. The empirical expression of the Strehl ratio, denoted by S , is given as follows [85]:

$$S = \frac{I(0)|_{\Phi \neq 0}}{I(0)|_{\Phi = 0}} \approx \exp \left[- (2\pi\sigma'_W)^2 \right], \quad (\text{E.0.2})$$

with $\sigma'_W = \sigma_W/\lambda_0$ is the wavefront error scaled by the wavelength given in unit of full phase, $I(0)$ being the image intensity at the center position in focal plane and Φ the wave aberration. A Strehl ratio bigger or equal to 0.8 is conventionally assumed to correspond to an ideal diffracted limited system [85, 88]. In other words, the aberration present at this Strehl ratio can be tolerated. This value corresponds to $\sigma'_W \approx 0.075$ (Std of phase aberration) and departure distance equal to a $\lambda_0/4$ of

the actual sphere from the Gaussian reference sphere (Rayleigh's quarter wave rule). The S metric will enable to determine the tolerable values of the tilt and imaging parameters and also the corresponding tolerance in terms of NCC.

Mean Relative Error: MRE and Mean Square Error: MSE

$$\text{MRE}(f, g) = \frac{\sum_j [g(j) - f(j)]}{\sum_j |g(j)|} \quad \text{Mean relative error,} \quad (\text{E.0.3})$$

$$\text{MSE}(f, g) = \frac{\sum_j |g(j) - f(j)|^2}{\sum_j j} \quad \text{Mean Square Error,} \quad (\text{E.0.4})$$

with f being the estimate of the gold standard or ground truth data g and j the spatial position.

Normalized Cross Correlation: NCC

The NCC at a given lag position l is defined as follows:

$$\text{NCC}_l(f, g) = \frac{\sum_j \{ [f(j) - \bar{f}_l][g(j-l) - g(j)] \}}{\sqrt{\sum_j [f(j) - \bar{f}_l]^2 \sum_j [g(j-l) - g(j)]^2}}, \quad (\text{E.0.5})$$

with f being the estimate of the gold standard or ground truth data g and \bar{f}_l is the mean value of f at the same range as g . The numerator of Eq. (E.0.5) can be computed easily using the formulation of cross-correlation with Fourier transform. It is proportional to the convolution of f with the flipped version of g . This corresponds to:

$$\text{NCC}_l^{\text{num}}(f, g) = \mathcal{F}^{-1} \{ \mathcal{F} \{ f \} \cdot \mathcal{F}^* \{ g \} \} - \bar{f}_l \sum_j [g(j-l) - g(j)], \quad (\text{E.0.6})$$

whereas the denominator is a normalization factor that can be computed using a running sum [91]. An algorithm has been implemented on MATLAB under the function named `normxcorr3` [92] to compute Eq. (E.0.5) efficiently. Eq. (E.0.5) can be applied to a 2D as well as a 3D data. $\text{NCC}_l(f, g)$ refers to the NCC of the two data f and g at a lag shift l . A shift of $l = 0$ means the two data are on top of each other. A value of NCC equal to 0 means zero-correlation, -1 anticorrelation and 1 is maximum correlation. If detecting any possible shift between the measured or estimate and reference data f and g respectively is not of interest, NCC is more advantageous over MRE.

List of References

- [1] Ulrich Kubitscheck. *Fluorescence microscopy: from principles to biological applications*. John Wiley & Sons, 2017.
- [2] Jerome Mertz. *Introduction to optical microscopy*. Cambridge University Press, 2019.
- [3] Wolfgang Singer, Michael Totzeck, and Herbert Gross. *Handbook of optical systems, volume 2: Physical image formation*. John Wiley & Sons, 2006.
- [4] Yasuhiro Hirano, Atsushi Matsuda, and Yasushi Hiraoka. Recent advancements in structured-illumination microscopy toward live-cell imaging. *Microscopy*, 64(4):237–249, 2015.
- [5] Peter J Shaw. Comparison of widefield/deconvolution and confocal microscopy for three-dimensional imaging. In *Handbook of biological confocal microscopy*, pages 453–467. Springer, 2006.
- [6] Stefan W Hell and Jan Wichmann. Breaking the diffraction resolution limit by stimulated emission: stimulated-emission-depletion fluorescence microscopy. *Optics letters*, 19(11):780–782, 1994.
- [7] Michael J Rust, Mark Bates, and Xiaowei Zhuang. Stochastic optical reconstruction microscopy (STORM) provides sub-diffraction-limit image resolution. *Nature methods*, 3(10):793, 2006.
- [8] Yu Chen et al. Review of advanced imaging techniques. *Journal of pathology informatics*, 3(1):22, 2012.
- [9] Jennifer A Thorley, Jeremy Pike, and Joshua Z Rappoport. Super-resolution microscopy: a comparison of commercially available options. In *Fluorescence microscopy*, pages 199–212. Elsevier, 2014.
- [10] Harold Hopkins. The frequency response of a defocused optical system. *Proceedings of the Royal Society of London. Series A. Mathematical and Physical Sciences*, 231(1184):91–103, 1955.
- [11] Colin Sheppard and Min Gu. Approximation to the three-dimensional optical transfer function. *JOSA A*, 8(4):692–694, 1991.

- [12] Arnold Sommerfeld. *Optics: lectures on theoretical physics*, volume 4. Academic Press, 1954.
- [13] Jakob J Stamnes. *Waves in Focal Regions: Propagation, Diffraction and Focusing of Light, Sound and Water Waves*, 1st. 1986.
- [14] Joseph W Goodman. *Introduction to Fourier optics*. 2nd. McGraw-Hill, 1996.
- [15] Robert L Lucke. Rayleigh-Sommerfield diffraction vs Fresnel-Kirchhoff, Fourier propagation and Poisson's spot. Technical report, Naval Research Lab Washington DC, 2004.
- [16] Yaakov M Engelberg and Shlomo Ruschin. Fast method for physical optics propagation of high-numerical-aperture beams. *JOSA A*, 21(11):2135–2145, 2004.
- [17] Per A Stokseth. Properties of a defocused optical system. *JOSA*, 59(10):1314–1321, 1969.
- [18] Yasushi Hiraoka, John W Sedat, and David A Agard. Determination of three-dimensional imaging properties of a light microscope system. Partial confocal behavior in epifluorescence microscopy. *Biophysical journal*, 57(2):325–333, 1990.
- [19] Sarah Frisken Gibson and Frederick Lanni. Diffraction by a circular aperture as a model for three-dimensional optical microscopy. *JOSA A*, 6(9):1357–1367, 1989.
- [20] Max Born and Emil Wolf. *Principles of Optics*, 3rd. Ed. J. Wiley & Sons. New York, NY, 1965.
- [21] Norbert Streibl. Three-dimensional imaging by a microscope. *JOSA A*, 2(2):121–127, 1985.
- [22] Sarah Frisken Gibson and Frederick Lanni. Experimental test of an analytical model of aberration in an oil-immersion objective lens used in three-dimensional light microscopy. *JOSA A*, 8(10):1601–1613, 1991.
- [23] Emil Wolf. Electromagnetic diffraction in optical systems-I. An integral representation of the image field. *Proceedings of the Royal Society of London. Series A. Mathematical and Physical Sciences*, 253(1274):349–357, 1959.
- [24] Bernard Richards and Emil Wolf. Electromagnetic diffraction in optical systems, II. Structure of the image field in an aplanatic system. *Proceedings of the Royal Society of London. Series A. Mathematical and Physical Sciences*, 253(1274):358–379, 1959.
- [25] Peter Török et al. Electromagnetic diffraction of light focused through a planar interface between materials of mismatched refractive indices: an integral representation. *JOSA A*, 12(2):325–332, 1995.
- [26] P Török, P Varga, and G Nemeth. Analytical solution of the diffraction integrals and interpretation of wave-front distortion when light is focused through a planar interface between materials of mismatched refractive indices. *JOSA A*, 12(12):2660–2671, 1995.
- [27] P Török and P Varga. Electromagnetic diffraction of light focused through a stratified medium. *Applied optics*, 36(11):2305–2312, 1997.

- [28] Colin Sheppard and Peter Török. An electromagnetic theory of imaging in fluorescence microscopy, and imaging in polarization fluorescence microscopy. *Bioimaging*, 5(4):205–218, 1997.
- [29] Rishi Kant. An analytical solution of vector diffraction for focusing optical systems. *Journal of Modern Optics*, 40(2):337–347, 1993.
- [30] Colin Sheppard and Peter Török. Efficient calculation of electromagnetic diffraction in optical systems using a multipole expansion. *Journal of Modern Optics*, 44(4):803–818, 1997.
- [31] Matthew R Foreman and Peter Török. Computational methods in vectorial imaging. *Journal of Modern Optics*, 58(5-6):339–364, 2011.
- [32] Denis K Samuylov et al. Modelling point spread function in fluorescence microscopy with a sparse combination of gaussian mixture: Trade-off between accuracy and efficiency. *arXiv preprint arXiv:1809.01579*, 2018.
- [33] Hagai Kirshner et al. 3-D PSF fitting for fluorescence microscopy: implementation and localization application. *Journal of microscopy*, 249(1):13–25, 2013.
- [34] Jizhou Li, Feng Xue, and Thierry Blu. Fast and accurate three-dimensional point spread function computation for fluorescence microscopy. *JOSA A*, 34(6):1029–1034, 2017.
- [35] Daniel Sage et al. Deconvolutionlab2: An open-source software for deconvolution microscopy. *Methods*, 115:28–41, 2017.
- [36] Min Guo et al. Rapid image deconvolution and multiview fusion for optical microscopy. *Nature biotechnology*, 38(11):1337–1346, 2020.
- [37] François Aguet et al. Super-resolution orientation estimation and localization of fluorescent dipoles using 3-D steerable filters. *Optics express*, 17(8):6829–6848, 2009.
- [38] Fernando Caprile, Luciano A Masullo, and Fernando D Stefani. Pyfocus—a python package for vectorial calculations of focused optical fields under realistic conditions. application to toroidal foci. *Computer Physics Communications*, 275:108315, 2022.
- [39] Stefan Hell et al. Aberrations in confocal fluorescence microscopy induced by mismatches in refractive index. *Journal of microscopy*, 169(3):391–405, 1993.
- [40] Colin Sheppard and Peter Török. Effects of specimen refractive index on confocal imaging. *Journal of microscopy*, 185(3):366–374, 1997.
- [41] Olivier Haeberlé. Focusing of light through a stratified medium: a practical approach for computing microscope point spread functions. Part I: Conventional microscopy. *Optics communications*, 216(1-3):55–63, 2003.
- [42] Sreya Ghosh and Chrysanthe Preza. Fluorescence microscopy point spread function model accounting for aberrations due to refractive index variability within a specimen. *Journal of biomedical optics*, 20(7):075003, 2015.

- [43] Yanlei Hu, Zhongyu Wang, Xuewen Wang, Shengyun Ji, Chenchu Zhang, Jiawen Li, Wulin Zhu, Dong Wu, and Jiaru Chu. Efficient full-path optical calculation of scalar and vector diffraction using the bluestein method. *Light: Science & Applications*, 9(1):119, 2020.
- [44] Marcel Leutenegger et al. Fast focus field calculations. *Optics express*, 14(23):11277–11291, 2006.
- [45] Kyoji Matsushima, Hagen Schimmel, and Frank Wyrowski. Fast calculation method for optical diffraction on tilted planes by use of the angular spectrum of plane waves. *JOSA A*, 20(9):1755–1762, 2003.
- [46] Eva Wegel. Basic Fluorescence Microscopy and Sample Preparation. https://download.s.micron.ox.ac.uk/lectures/micron_course_2013/Lecture_04_BasicFluoMicro.pdf. [Online; accessed 05-June-2023].
- [47] William Meinel, Jean-Christophe Olivo-Marin, and Elsa D Angelini. Denoising of microscopy images: a review of the state-of-the-art, and a new sparsity-based method. *IEEE Transactions on Image Processing*, 27(8):3842–3856, 2018.
- [48] Ce Liu et al. Noise estimation from a single image. In *2006 IEEE Computer Society Conference on Computer Vision and Pattern Recognition (CVPR'06)*, volume 1, pages 901–908. IEEE, 2006.
- [49] Colin Sheppard and Min Gu. Imaging by a high aperture optical system. *Journal of Modern Optics*, 40(8):1631–1651, 1993.
- [50] Daniel Malacara-Hernández and Zacarías Malacara-Hernández. *Handbook of optical design*. CRC Press, 2017.
- [51] Herbert Gross, Fritz Blechinger, and Bertram Achtner. *Handbook of optical systems, volume 4: Survey of Optical Instruments*. John Wiley & Sons, 2008.
- [52] Yueqian Zhang and Herbert Gross. Systematic design of microscope objectives. Part I: System review and analysis. *Advanced Optical Technologies*, 8(5):313–347, 2019.
- [53] Bernard Roelof Andries Nijboer. The diffraction theory of optical aberrations: Part I: General discussion of the geometrical aberrations. *Physica*, 10(8):679–692, 1943.
- [54] Herbert Gross, Hannfried Zügge, Martin Peschka, and Fritz Blechinger. *Handbook of optical systems, volume 3: Aberration Theory and Correction of Optical Systems*. John Wiley & Sons, 2007.
- [55] Bernard Roelof Andries Nijboer. The diffraction theory of optical aberrations: Part II: Diffraction pattern in the presence of small aberrations. *Physica*, 13(10):605–620, 1947.
- [56] Vasudevan Lakshminarayanan and Andre Fleck. Zernike polynomials: a guide. *Journal of Modern Optics*, 58(7):545–561, 2011.

- [57] Stephen M Anthony et al. Imaging effectiveness calculator for non-design microscope samples. *Applied Optics*, 58(22):6027–6037, 2019.
- [58] Andrei Nikolaevich Tikhonov. On the solution of ill-posed problems and the method of regularization. In *Doklady akademii nauk*, volume 151, pages 501–504. Russian Academy of Sciences, 1963.
- [59] Peter J Verveer and Thomas M Jovin. Image restoration based on Good’s roughness penalty with application to fluorescence microscopy. *JOSA A*, 15(5):1077–1083, 1998.
- [60] Peter J Verveer, Mark J Gemkow, and Thomas M Jovin. A comparison of image restoration approaches applied to three-dimensional confocal and wide-field fluorescence microscopy. *Journal of microscopy*, 193(1):50–61, 1999.
- [61] Rainer Heintzmann. Estimating missing information by maximum likelihood deconvolution. *Micron*, 38(2):136–144, 2007.
- [62] IJ Good and Ray A Gaskins. Nonparametric roughness penalties for probability densities. *Biometrika*, 58(2):255–277, 1971.
- [63] Ferréol Soulez et al. Blind deconvolution of 3D data in wide field fluorescence microscopy. In *2012 9th IEEE International Symposium on Biomedical Imaging (ISBI)*, pages 1735–1738. IEEE, 2012.
- [64] Henry Crew. *The Wave Theory of Light-Memoirs by Huygens, Young and Fresnel*. Chapman Press, 2009.
- [65] CW McCutchen. Generalized aperture and the three-dimensional diffraction image. *JOSA*, 54(2):240–244, 1964.
- [66] Rainer Heintzmann. Band limit and appropriate sampling in microscopy. In *Cell biology*, pages 29–36. Elsevier, 2006.
- [67] Qing Cao. Generalized jinc functions and their application to focusing and diffraction of circular apertures. *JOSA A*, 20(4):661–667, 2003.
- [68] Mark Richardson. Fundamentals of the discrete fourier transform. *Sound & Vibration Magazine*, 12:40–46, 1978.
- [69] Frédéric Nataf. Absorbing boundary conditions and perfectly matched layers in wave propagation problems. *Direct and inverse problems in wave propagation and applications*, 14:219–231, 2013.
- [70] Dean A Frickey. Using the inverse chirp-z transform for time-domain analysis of simulated radar signals. Technical report, Idaho National Engineering Lab., Idaho Falls, ID (United States), 1995.
- [71] L Rabiner, RW Schafer, and C Rader. The chirp z-transform algorithm. *IEEE transactions on audio and electroacoustics*, 17(2):86–92, 1969.

- [72] Daissy H Garces, William T Rhodes, and Nestor M Peña. Projection-slice theorem: a compact notation. *JOSA A*, 28(5):766–769, 2011.
- [73] Dina Yaqoob Alsaka et al. A comparison of iterative Fourier transform algorithms for image quality estimation. *Optical Review*, 25(5):625–637, 2018.
- [74] RJMM Arimoto and JM Murray. A common aberration with water-immersion objective lenses. *Journal of microscopy*, 216(1):49–51, 2004.
- [75] James Pawley. *Handbook of biological confocal microscopy*, volume 236. Springer Science & Business Media, 2006.
- [76] Mats GL Gustafsson et al. Three-dimensional resolution doubling in wide-field fluorescence microscopy by structured illumination. *Biophysical journal*, 94(12):4957–4970, 2008.
- [77] Claus B Müller and Jörg Enderlein. Image scanning microscopy. *Physical review letters*, 104(19):198101, 2010.
- [78] Roman Schmidt, Johann Engelhardt, and Marion Lang. 4Pi microscopy. In *Nanoimaging*, pages 27–41. Springer, 2013.
- [79] Amicia D Elliott. Confocal microscopy: principles and modern practices. *Current protocols in cytometry*, 92(1):e68, 2020.
- [80] Matthew R Arnison et al. Wavefront coding fluorescence microscopy using high aperture lenses. In *Optical imaging and microscopy*, pages 143–165. Springer, 2003.
- [81] Jan Becker and Rainer Heintzmann. PSF broadening due to fluorescence emission. *bioRxiv*, 2019.
- [82] Min Gu. *Advanced optical imaging theory*, volume 75. Springer Science & Business Media, 2000.
- [83] Ralph W Gerchberg. A practical algorithm for the determination of phase from image and diffraction plane pictures. *Optik*, 35:237–246, 1972.
- [84] Bridget M Hanser et al. Phase-retrieved pupil functions in wide-field fluorescence microscopy. *Journal of microscopy*, 216(1):32–48, 2004.
- [85] Virendra N Mahajan. *Aberration theory made simple*. SPIE Press, 2nd edition, 2011.
- [86] Raimund J Ober, Sripad Ram, and E Sally Ward. Localization accuracy in single-molecule microscopy. *Biophysical journal*, 86(2):1185–1200, 2004.
- [87] Plastic chroma slide. <https://argolight.com/blog/fluorescent-plastic-slides-field-uniformity/>. Accessed: 2022-09-05.
- [88] Virendra N Mahajan. Strehl ratio for primary aberrations: some analytical results for circular and annular pupils. *JOSA*, 72(9):1258–1266, 1982.

- [89] A Griffa, N Garin, and D Sage. Comparison of deconvolution software in 3D microscopy: a user point of view-part 1. *GIT Imaging & Microscopy*, 12(ARTICLE):43–45, 2010.
- [90] Dong C Liu and Jorge Nocedal. On the limited memory BFGS method for large scale optimization. *Mathematical programming*, 45(1):503–528, 1989.
- [91] JP Lewis. Fast normalized cross-correlation int. In *Proceedings of Vision Interface*, pages 120–123, 1995.
- [92] Daniel Eaton. normxcorr3 (Fast 3D NCC). <https://www.mathworks.com/matlabcentral/fileexchange/73946-normxcorr3-fast-3d-ncc>, 2020. Accessed: 2022-02-12.